Converting antimicrobial into targeting peptides reveals key features governing protein import into mitochondria and chloroplasts

Oliver D Caspari, Clotilde Garrido, Yves Choquet, Francis-André Wollman, Ingrid Lafontaine

▶ **To cite this version:**

Oliver D Caspari, Clotilde Garrido, Yves Choquet, Francis-André Wollman, Ingrid Lafontaine. Converting antimicrobial into targeting peptides reveals key features governing protein import into mitochondria and chloroplasts. 2022. hal-03844827

HAL Id: hal-03844827
https://hal.science/hal-03844827

Preprint submitted on 9 Nov 2022

HAL is a multi-disciplinary open access archive for the deposit and dissemination of scientific research documents, whether they are published or not. The documents may come from teaching and research institutions in France or abroad, or from public or private research centers.

L'archive ouverte pluridisciplinaire **HAL**, est destinée au dépôt et à la diffusion de documents scientifiques de niveau recherche, publiés ou non, émanant des établissements d'enseignement et de recherche français ou étrangers, des laboratoires publics ou privés.

bioRxiv preprint doi: https://doi.org/10.1101/2021.12.03.471120; this version posted June 23, 2022. The copyright holder for this preprint (which was not certified by peer review) is the author/funder, who has granted bioRxiv a license to display the preprint in perpetuity. It is made available under aCC-BY-NC-ND 4.0 International license.

Converting antimicrobial into targeting peptides reveals key features governing protein import into mitochondria and chloroplasts

Oliver D Caspari[1¶*†], Clotilde Garrido[1], Yves Choquet[1], Francis-André Wollman[1], Ingrid Lafontaine[1*]

[1]UMR7141 (CNRS/Sorbonne Université), Institut de Biologie Physico-Chimique, 13 Rue Pierre et Marie Curie, 75005 Paris, France

[¶]Lead contact

*corresponding authors:

ODC: **odc20@cantab.net**

IL: **ingrid.lafontaine@ibpc.fr**

current addresses:

[†]Department of Microbiology, Institut Pasteur, 28 Rue Docteur Roux, 75015 Paris, France

bioRxiv preprint doi: https://doi.org/10.1101/2021.12.03.471120; this version posted June 23, 2022. The copyright holder for this preprint (which was not certified by peer review) is the author/funder, who has granted bioRxiv a license to display the preprint in perpetuity. It is made available under aCC-BY-NC-ND 4.0 International license.

Summary

We asked what peptide features govern targeting to the mitochondria versus the chloroplast using antimicrobial peptides as a starting point. This approach was inspired by the endosymbiotic hypothesis that organelle-targeting peptides derive from antimicrobial amphipathic peptides delivered by the host cell, to which organelle progenitors became resistant. To explore the molecular changes required to convert antimicrobial into targeting peptides, we expressed a set of 13 antimicrobial peptides in *Chlamydomonas reinhardtii*. Peptides were systematically modified to test distinctive features of mitochondrial and chloroplast targeting peptides, and we assessed their targeting potential by following the intracellular localization and maturation of a Venus fluorescent reporter used as cargo protein. Mitochondrial targeting can be achieved by unmodified antimicrobial peptide sequences and is improved by replacing Lysines with Arginines and adding a processing site. The presence of unstructured sequence and protein interaction sites enable chloroplast targeting. Chloroplast targeting is subject to more constraints, consistent with chloroplast endosymbiosis having occurred in a cell that already contained mitochondria. If indeed targeting peptides evolved from antimicrobial peptides, required modifications imply a temporal evolutionary scenario with an early exchange of cationic residues, and a late acquisition of chloroplast specific motifs.

Keywords:

1. Antimicrobial peptide
2. *Chlamydomonas reinhardtii*
3. Chloroplast
4. Endosymbiotic organellogenesis
5. Mitochondria
6. Presequence
7. Targeting peptide
8. Transit peptide

bioRxiv preprint doi: https://doi.org/10.1101/2021.12.03.471120; this version posted June 23, 2022. The copyright holder for this preprint (which was not certified by peer review) is the author/funder, who has granted bioRxiv a license to display the preprint in perpetuity. It is made available under aCC-BY-NC-ND 4.0 International license.

Introduction

Mitochondria and Chloroplasts arose through endosymbiosis and retain their own genomes, yet the vast majority of organellar proteins is encoded in the nucleus, translated in the cytoplasm and imported into the organelles[1,2]. N-terminal targeting peptides (TPs) that are cleaved off upon import provide the information on targeting, although their primary structures are very diverse[3]. Yet chloroplast transit peptides (cTP) and mitochondrial presequences (mTP) have very similar physico-chemical properties making reliable differentiation often challenging. A multitude of studies has found sequence elements contributing to specificity determination, and prediction programs have been improving[4,5], yet a mechanistic understanding of how targeting information is encoded has remained elusive.

Here, we use antimicrobial peptides (AMP) as an original chassis, to test the contribution of key TP features towards targeting efficiency and specificity. Part of the innate immune system, AMPs are produced by virtually all types of cells in a bid to kill or control microbial adversaries[6,7]. AMPs have recently been proposed to be at the evolutionary origin of TPs[8,9]. The proposed evolutionary scenario posits that early during endosymbiotic organellogenesis of first the mitochondrion and later the chloroplast, the host cell used AMPs to attack the bacterial proto-endosymbiont. A bacterial resistance mechanism, whereby the AMP is imported into the bacterial cytoplasm, would have generated a pathway for host proteins to reach the bacterial cytosol – a plausible first step in the evolution of a protein import machinery. Cationic, Helical-Amphipathic Ribosomally-produced AMPs (HA-RAMPs) and TPs share key physico-chemical properties and they were shown, in some instances, to retain cross-functionality[10]: several TPs showed antimicrobial activity and selected HA-RAMPs, fused to a cleavage-site containing TP element, were shown to promote the import of a Venus fluorescent protein into either the mitochondria or the chloroplast of the model green alga *Chlamydomonas reinhardtii*.

The main part of mTPs and the central element of cTPs most closely resemble HA-RAMPs on account of a shared cationic, amphipathic helical structure that often encompasses the entire length of the HA-RAMPs[9] and mTPs[11,12]. Although plant cTPs have been described as unstructured[13], algal cTPs more closely resemble mTPs in being helical[14]. Helices were observed by NMR in membrane-mimetic environments in both algal and plant cTPs[3,15–18], and signatures of amphipathic helices can be detected in a majority of cTPs[10].

bioRxiv preprint doi: https://doi.org/10.1101/2021.12.03.471120; this version posted June 23, 2022. The copyright holder for this preprint (which was not certified by peer review) is the author/funder, who has granted bioRxiv a license to display the preprint in perpetuity. It is made available under aCC-BY-NC-ND 4.0 International license.

In addition to the helices, both mTPs and cTPs contain recognition sites at the C-terminus where processing peptidases in the mitochondrial matrix (MPP) and the chloroplast stroma (SPP) cleave off the cargo protein[19]. These recognition sites encompass some 10 residues upstream of the cleavage site and are structurally distinct from the rest of the TPs, even showing a weak sequence conservation[4,12,20]. While targeting information is usually contained within mTP sequences upstream of the cleavage site, targeting by cTPs shorter than ca. 60 amino acids often requires downstream unstructured sequence stretches in the N-terminal domain of the mature protein[21,22]. Besides the amphipathic helical module and the C-terminal cleavage module shared between mTPs and cTPs, it has been argued that distinct features at their N-termini conferred organelle specificity to each set of targeting peptides[2,12,20,23–28].

In this study, we systematically introduced modifications into a diversity of HA-RAMPs in a bid to generate targeting to the mitochondria or chloroplast in Chlamydomonas. This dataset provides new insights into how different TP elements contribute to differential targeting and to the efficiency of protein import. Being similar in physico-chemical properties to TPs[10], HA-RAMPs provide a privileged vantage point from which to study sequence elements that govern targeting. In our choice of HA-RAMPs, we aimed to reflect the diversity of available sequences by choosing representatives of different HA-RAMP families based on similarity with TPs. We show that some of our 13 HA-RAMPs natively contain TP-like sequence elements, with some HA-RAMPs being prone to chloroplast targeting while others show a preference for the mitochondria. Furthermore, we provide evidence for a critical functional difference in cationic residues with Lysine (K) being used in HA-RAMPs and Arginine (R) in TPs.

Results

HA-RAMPs display varying degrees of similarity to TPs

Figure 1 shows the major sequence features of the 13 HA-RAMPs used in the present study (Fig. 1a) together with those of a typical cTP and a typical mTP (Fig. 1b). On the right-hand side, these peptides are represented according to their proportion of a-helical amphipathic structure. The HA-RAMPs Brevinin-2ISb (B2I), Magainin 2 (MII), Ranatuerin-2G (R2G), Dermaseptin S4 (DS4), Dermadistinctin-M (DDM),

bioRxiv preprint doi: https://doi.org/10.1101/2021.12.03.471120; this version posted June 23, 2022. The copyright holder for this preprint (which was not certified by peer review) is the author/funder, who has granted bioRxiv a license to display the preprint in perpetuity. It is made available under aCC-BY-NC-ND 4.0 International license.

Brevinin-1E (B1E), Cecropin-P3 (CP3), Sarcotoxin-1D (S1D), Esculentin-1SEA (E1S), Leucocin A (LCA), SI Moricin (SIM), Bacillocin 1580 (B15), and Enterocin HF (EHF) were chosen such that different AMP families would be represented with varying proximity to TPs (Table S1) and thus a range of physico-chemical properties be explored (Fig. S1). As negative controls, two peptides that lack predicted amphipathic helices were chosen from among randomly generated sequences (Fig. 1c).

To explore targeting, the 13 HA-RAMPs were systematically modified (Fig. 2), notably by adding TP elements from the N- and/or C-terminal domains of Chlamydomonas Rubisco activase (RBCA) cTP, or a C-terminal domain of similar length from mitochondrial γ-carbonic anhydrase 2 (CAG2) mTP (Fig. 1b, Fig. 2). In a bid to keep peptidase recognition sites intact, C-terminal elements were designed to start 10 residues upstream of the cleavage site, even though this slightly truncates TP helices. Peptides carrying the 15 amino-acid long cTP N-terminus (cTP-N) will be denoted ^{c}P. Similarly, peptides with C-terminal elements from RBCA-cTP (cTP-C) or CAG2-mTP (mTP-C) will be denoted P^{c} or P^{m} respectively. Micrographs for three biological replicates per construct are displayed on Fig. S2-S19. The reader will be asked to return to Fig. 2 throughout, with Fig. 3 and Fig. 4 providing selected micrographs as examples highlighting particular points of interest.

Some unmodified HA-RAMPs generate mitochondrial targeting

In the absence of any modifications, B2I and MII were capable of organelle-targeting visible in fluorescence microscopy (Fig. 2 row A, Fig. S2-S14). When equipped with B2I, the fluorescent reporter Venus shows mitochondrial localization (Fig. 3a, Fig. S2): the Venus signal is observed as a characteristic network pattern that co-localizes with MitoTracker fluorescence. By contrast, in the case of MII only a small fraction of fluorescence signal in the Venus channel shows co-localisation with the mitotracker dye, signifying that targeting is only partial (Fig. 3a, Fig. S3). Note that in these epifluorescence images, some autofluorescence emanating from the chloroplast is present in the Venus channel (Fig. 3b). Where possible, the brightness of these images was adjusted to remove this autofluorescence. Chosen brightness settings are indicated next to each image. In cases where low Venus accumulation necessitated brightness values low enough for autofluorescence to be visible in the Venus channel, a black dotted line is visible in the brightness display.

bioRxiv preprint doi: https://doi.org/10.1101/2021.12.03.471120; this version posted June 23, 2022. The copyright holder for this preprint (which was not certified by peer review) is the author/funder, who has granted bioRxiv a license to display the preprint in perpetuity. It is made available under aCC-BY-NC-ND 4.0 International license.

K/R content contributes to functional divergence between HA-RAMP and TP

We looked for differences in primary sequence that might impede the ability of the remaining 11 HA-RAMPs to target. As illustrated on Fig. S20, extant HA-RAMPs and organellar TPs display a few differences in their amino-acid content. HA-RAMPs are richer in helix-breaking Glycines (G) but poorer in Prolines (P), whereas TPs are enriched in Serines (S) compared to HA-RAMPs. Most of the other amino acid frequencies are broadly similar between the two sets of peptides and within range of the average value across all entries in the UNIPROT database (red lines). As expected, both HA-RAMPs and TPs are poor in acidic residues (D, E) but enriched in basic residues (K or R). However, their complement in basic residues is markedly different (Fig. 3c, Fig. S20): HA-RAMPs are rich in Lysines (K) whereas TPs are rich in Arginines (R).

In order to see whether these contrasting differences in K/R ratio contributed to the functional divergence between HA-RAMPs and TPs, we substituted all instances of R by K in TPs and of K by R in HA-RAMPs. In the rest of the text, the basic amino acid mostly present in a given peptide P will be indicated by a subscript as P_R or P_K. HA-RAMPs with K→R transition showed reduced antimicrobial activity, as illustrated on Fig. 3d by the increased minimum inhibitory concentrations for MII, DS4 or B1E.

We used Chlamydomonas Rubisco activase (RBCA) cTP ($^{c}CH_R^{c}$) and mitochondrial γ-carbonic anhydrase 2 (CAG2) mTP (MH_R^{m}) as positive controls for chloroplast and mitochondrial targeting respectively (Fig. 3e, Fig. S17-S18). Note that TP helical fragments, stripped of their N- and C-terminal domains, are denoted as MH for mTP and CH for cTP (Fig. 1b). Chloroplast localization of RBCA-cTP ($^{c}CH_R^{c}$) is evident from a bright Venus signal colocalizing with chlorophyll autofluorecence, Furthermore, Venus accumulates in the pyrenoid, a proteinaceous chloroplast subcompartment that contains a large majority of Rubisco. While small proteins like Venus can enter the pyrenoid, most thylakoid membranes are excluded, allowing the structure to be localized as a dip in chlorophyll autofluorescence. Venus channel signal emanating from the pyrenoid is thus a useful visual guide to true chloroplast localization of the fluorescent reporter[29]. Note that due to cTP-C containing a Rubisco-binding motif[30], Venus accumulation in the Rubisco microcompartment, the pyrenoid, is particularly pronounced in constructs carrying this element. When natively R-rich RBCA-cTP and CAG2-mTP sequences were subjected to systematic R→K substitutions ($^{c}CH_K^{c}$, MH_K^{m}), their ability to target were reduced or abolished

bioRxiv preprint doi: https://doi.org/10.1101/2021.12.03.471120; this version posted June 23, 2022. The copyright holder for this preprint (which was not certified by peer review) is the author/funder, who has granted bioRxiv a license to display the preprint in perpetuity. It is made available under aCC-BY-NC-ND 4.0 International license.

(Fig. 3e, Fig. S17-S18). These experiments demonstrate the respective functional contributions of K and R residues to antimicrobial and organelle targeting activity. We then systematically re-examined the organelle targeting ability of the set of 13 HA-RAMP that had undergone K→R substitutions (Fig. 2 row B, Fig. S2-S14). MII_R now shows full mitochondrial targeting, and $R2G_R$ as well as $CP3_R$ show partial targeting, as evidenced by significant overlap of Venus and mitotracker fluorescence (Fig. 3f, Fig. S3, S4, S8).

TP C-termini matter for targeting

Addition of mTP-C, the cleavage-site containing C-terminal element of CAG2-mTP (Fig. 4a, Fig. 2 rows CD) enabled mitochondrial targeting for $E1S_R$ and $R2G_K$ and improved the targeting already observed for $R2G_R$ and $CP3_R$, in addition to continued targeting by B2I and MII. The impact of adding cTP-C, the C-terminal element derived from RBCA-cTP, is even more important: cTP-C significantly enabled chloroplast targeting, which could be seen in nine HA-RAMP constructs involving $CP3_R$, S1D, LCA, B15 and EHF (Fig. 4b, Fig. 2 rows E,F, Fig. S8, S9, S11, S13, S14). The addition of cTP-C to the helical part of the CAG2-mTP (MH_R^c) even partially retargets the construct to the chloroplast (Fig. 4c, Fig. S18), and deletion of cTP-C abolishes chloroplast targeting by RBCA-cTP (^cCH_R) (Fig. 4c, Fig. S17). By comparison, deletion of mTP-C reduces but does not totally abolish mitochondrial targeting of CAG2-mTP (MH_R) (Fig. 4c, Fig. S18), and addition of mTP-C fails to rescue ^cCH_R ($^cCH_R^m$) (Fig. 4c, Fig. S17). Note that the addition of cTP-C was also compatible with mitochondrial localization by B2I and MII (Fig. 4b, Fig. 2 rows E,F, Fig. S2, S3). The addition of mTP-C also enabled chloroplast localization by EHF_R (Fig. 2 row D), visible despite low Venus channel brightness as Venus signal emanating from within the pyrenoid (Fig. 4a, Fig. S14).

cTP N-termini matter for chloroplast targeting

The sole addition of cTP-N generated at least partial chloroplast targeting in 6 HA-RAMP constructs, notably by SIM, but also $CP3_R$, $E1S_R$, $B15_R$ and EHF_R (Fig. 4d, Fig. 2 rows G,H, Fig. S8, S10, S12, S13, S14). However, cTP-N also enabled mitochondrial targeting in three HA-RAMPs that had not previously shown mitochondrial localization, B1E, DDM_R and S1D (Fig. 4e, Fig. 2 rows G,H, Fig. S5, S7, S9).

bioRxiv preprint doi: https://doi.org/10.1101/2021.12.03.471120; this version posted June 23, 2022. The copyright holder for this preprint (which was not certified by peer review) is the author/funder, who has granted bioRxiv a license to display the preprint in perpetuity. It is made available under aCC-BY-NC-ND 4.0 International license.

The importance of cTP-N as a chloroplast determinant becomes more evident when combined with a C-terminal element: addition of cTP-N to constructs equipped with mTP-C resulted in 10 HA-RAMP constructs targeting the chloroplast ($CP3_K$, E1S, LCA_K, SIM, B15, EHF) as well as 6 constructs showing dual targeting to the chloroplast and the mitochondria ($B2I_R$, MII_R, B1E, S1D) (Fig. 2 rows I,J, Fig. S2-S3, S5, S8-S14). Combining cTP-N with cTP-C (Fig. 2 rows KL, Fig. S2-S5, S7-S14) generates at least partial chloroplast targeting in 22 out of 26 HA-RAMP constructs (including 1 instance of dual targeting by $R2G_R$; Fig. S4); only DS4 fails to show any chloroplast targeting (Fig. S6). Consider ^{c}B2I (Fig. 2 column a rows G-L, Fig. S2) as an example of the effect of combining cTP-N with C-termini, shown in Fig. 4f: Equipped with mTP-C, $^{c}B2I_K^{m}$ targets the mitochondria whereas addition of cTP-C ($^{c}B2I_K^{c}$) generates partial targeting to the chloroplast. Upon K→R, the presence of mTP-C ($^{c}B2I_R^{m}$) now supports dual targeting and full chloroplast targeting is observed in the presence of cTP-C ($^{c}B2I_R^{c}$).

Finally, Fig. 4g shows that while addition of cTP-N to the CAG2-mTP abolished mitochondrial targeting ($^{c}MH_R^{m}$), the cTP-N/cTP-C combination also retargets MH to the chloroplast, and enables partial chloroplast targeting of a control in which the central element is composed of a poly-Alanine tract ($^{c}AA^{c}$) devoid of amphipathic properties and of a no peptide control (^{c}-^{c}) (Fig. 2 columns q-s, rows KL). The two latter experiments demonstrate that there are enough determinants for recognition of the chloroplast translocon dispersed between the Nter and Cter of a cTP, to target Venus to the chloroplast, albeit with a lower efficiency than when an amphipathic helix is present in between.

To further explore the role of the N-terminal cTP domain, we performed some in silico comparisons of the studied peptides. In Principal Component Analyses on ACC Z-scales[10] comparing TP N- and C-termini with our 13 HA-RAMPs (Fig. S21), cTPs and mTPs could be differentiated much better by N- compared to C-termini, supporting N-termini as important specificity determinants. Furthermore, even though algal cTP N-termini are more charged, less hydrophobic and more disordered than higher plant cTPs (Fig. S22) in line with algal cTPs being more mTP-like[14], Chlamydomonas cTP N-termini are recognized as chloroplast-targeting in a model trained on Arabidopsis TP and vice versa (Fig. S22), confirming that essential physico-chemical features of chloroplast determination in cTP N-termini are maintained in both lineages.

bioRxiv preprint doi: https://doi.org/10.1101/2021.12.03.471120; this version posted June 23, 2022. The copyright holder for this preprint (which was not certified by peer review) is the author/funder, who has granted bioRxiv a license to display the preprint in perpetuity. It is made available under aCC-BY-NC-ND 4.0 International license.

HA-RAMPs dominate targeting specificity

Considering Fig. 2 by columns reveals that organelle specificity is, to a large extent, determined by HA-RAMPs. Only 3 HA-RAMPs (B2I, R2G, MII; referred to hereafter as the mt-set) account for >70% of all constructs where mitochondrial targeting is seen. Similarly, 5 HA-RAMPs (E1S, LCA, SIM, B15, EHF; referred to as the cp-set) account for the majority (~57%) of all chloroplast targeting, and for two thirds when excluding the cTP-N/cTP-C combination that generates chloroplast targeting across most HA-RAMPs. In some instances, a set of peptide modifications may switch targeting from the mitochondria to the chloroplast, yet the major effect of modifications, i.e. exchanging K→R (Fig. 3, Fig. S23) or adding TP elements (Fig. 4, 6), is to enhance the targeting ability to an organelle determined by the HA-RAMP primary sequence properties (Fig. 2).

Chloroplast targeting involves longer, less helical peptides

To understand what differentiates mt-set from cp-set HA-RAMPs, we examined the sequence characteristics of our 13 HA-RAMPs with those of well-characterized Chlamydomonas targeting peptides (Fig. 5). In Chlamydomonas, mTPs are ca. 35 residues in length (Fig. 5a). By contrast, most cTPs are significantly longer ($p=0.0017$). The difference is even greater than shown here given that many cTPs require a contribution from post-cleavage site residues for successful targeting[10,21,22]. Consistently, cp-set HA-RAMPs (in green, Fig. 5a) are longer than mt-set HA-RAMPs (in orange; $p=0.0184$) and require further elongation by addition of TP elements before targeting can be observed (Fig. 2).

Most mTPs fold into an amphipathic helix for most of the sequence (~80% on average, Fig. 5b) starting directly from their N-terminus (Fig. 5c). The fraction dedicated to amphipathic helix formation in cTPs is significantly lower (Fig. 5b, $p<0.0001$), with a longer stretch of non-helical sequence at the N-terminus (Fig. 5c, $p<0.0001$). A PCA analysis based on these properties, plus the fraction of R and K, recapitulates the combined properties within each peptide (Fig. S24). The PCA shows that cp-set HA-RAMPs are localized with cTPs in the upper left area of the graph, consistent with a lower helix fraction (Fig. 1, Fig. 5b) due to longer sequence stretches upstream of the main helix than in the mt-set HA-RAMPs (Fig. 1, Fig. 5c, $p=0.0199$). Consistent with the importance of these helical features, LCA, the most helical among cp-set HA-RAMPs also shows the highest fraction of only partial

bioRxiv preprint doi: https://doi.org/10.1101/2021.12.03.471120; this version posted June 23, 2022. The copyright holder for this preprint (which was not certified by peer review) is the author/funder, who has granted bioRxiv a license to display the preprint in perpetuity. It is made available under aCC-BY-NC-ND 4.0 International license.

chloroplast targeting (3 out of 5 targeting constructs, Fig. 2 column j rows E,F,K). Furthermore, SIM and E1S, the two cp-set HA-RAMPs with the shortest pre-helix segments (Fig7 row C), both require addition of cTP-N for chloroplast targeting (Fig. 2 columns i,k).

cTPs are predicted to be more prone to protein interaction than mTPs

cTPs appear more likely to interact with proteins than mTPs (Fig. S25), just like cp-set HA-RAMPs. 'FGLK' motifs that are reportedly TOC interaction sites in plant cTPs[2] appear shortened to 'GLK' motifs in Chlamydomonas but they are associated with an increased protein interaction potential in cTPs compared to mTPs ($p<0.0001$), including within cTP-N and cTP-C elements. However, Hsp70-interaction sites[25], which are commonly found at cTP N-termini[2], also occur at a high frequency in mTP sequences and HA-RAMPs (Fig. S25, S26).

Probing cleavage of HA-RAMP-driven reporter constructs by immunobloting

To characterize the maturation of HA-RAMP–targeted proteins upon organellar import, we performed immunoblotting experiments (Fig. 6). Indicative examples were selected for clarity; a more comprehensive overview is provided in Fig. S27.

In the absence of a dedicated cleavage site (Fig. 6a), we found some cleavage did occur but preproteins are also maintained: two bands are observed in constructs that were localized in an organelle by fluorescence imaging (lanes d,f-j). The upper band corresponds to unprocessed Venus, which is a fusion of the reporter with the HA-RAMP construct and migrates at varying positions depending on the length of the presequence. The lower band corresponds to the processed form migrating closer to the "free" Venus position (lane c) depending on the exact site of cleavage. The cTP and mTP controls (lanes a,b) contain 23 residues between cleavage site and Venus (Venus+23), and maintain very little preprotein migrating above. In HA-RAMP constructs by contrast, the majority of Venus remained in the unprocessed top band for constructs targeting the mitochondria (lanes f-j). Nonetheless, the presence of a faint processed form in the lower band just above free Venus shows that some cleavage occurs. The proportion of processed versus unprocessed Venus preprotein is much higher in partially chloroplast-targeted $^{c}SIM_{K}$ (lane d), hinting at more efficient degradation of the unprocessed form in the chloroplast (see also Fig. S27).

Addition of cleavage sites improves cleavage across organelles: In the presence of either cTP-C (Fig. 6b, Blot 1) or mTP-C (Fig. 6b, Blot 2), which contain the RBCA-

bioRxiv preprint doi: https://doi.org/10.1101/2021.12.03.471120; this version posted June 23, 2022. The copyright holder for this preprint (which was not certified by peer review) is the author/funder, who has granted bioRxiv a license to display the preprint in perpetuity. It is made available under aCC-BY-NC-ND 4.0 International license.

cTP and CAG2-mTP cleavage sites respectively, targeting constructs appear to be cleaved at a site corresponding to TP controls (Venus+23). Constructs equipped with either of the two cleavage sites deliver a processed Venus of similar size, independently of whether the mitochondria or the chloroplast are targeted (Fig. 6b). These results indicate that mTP and cTP cleavage sites are recognized in both organelles. We note that in the case of HA-RAMP constructs equipped with mTP-C, cleavage appears to occur not at the cleavage site previously identified for CAG2 (Fig. 6b Blot 2 lane a, top band, corresponding to Venus+23), but instead at or near a second site closer to "free" Venus (compare Fig. 6b Blot 2 lane a, bottom band to lanes b-g), implying processing within ten residues upstream of Venus. Unlike mTP-C (Fig. 6b Blot 2 lane h), cTP-C appears to be processed in the absence of targeting (Fig. 6b Blot 1 lanes a,b) at a site different to the one used in organelles (Fig. 6b Blot 1 lanes c-h).

A switch from K to R (Fig. 6c), which improved targeting, also increased the amount of processed form relative to that of the unprocessed form in all cases, whether due to a gain of targeting (lanes f-i) or an increase in efficiency (lanes b-e), suggesting that cleavage can serve as a proxy for targeting. Indeed, there is a remarkable correlation between which constructs show cleavage, as observed in immunoblots, and which constructs show targeting, as judged from microscopy (Fig. S27). We note that faint processed bands can be seen for several unmodified HA-RAMPs (Fig. S27), suggesting further peptides in addition to $B2I_K$ and MII_K (Fig. 2) may be able to support some amount of targeting that is, however, too partial to be seen in fluorescence microscopy.

Discussion

How to make TPs from HA-RAMPs

To gain insight into peptide features that govern targeting, we used a related but separate class of peptides, HA-RAMPs, as chassis and stacked modifications to generate targeting into mitochondria or chloroplasts, or in some cases into both (Fig. 7a).

Arginines target better than Lysines

We showed that a K-to-R-switch increases targeting efficacy to both organelles across many constructs. R is more common than K in cTPs across green algae, vascular

bioRxiv preprint doi: https://doi.org/10.1101/2021.12.03.471120; this version posted June 23, 2022. The copyright holder for this preprint (which was not certified by peer review) is the author/funder, who has granted bioRxiv a license to display the preprint in perpetuity. It is made available under aCC-BY-NC-ND 4.0 International license.

plants, red algae, glaucophytes and many secondary plastids[31], but the functional significance for targeting efficacy had not previously been recognized. Our observation is in line with a previous report that a R-to-K switch at the N-ter of an Arabidopsis mTP abolished targeting (Lee at al., 2019). The underlying mechanism warrants further research, since differences in bulkiness and pKa[32,33], or in trans-acting factors that regulate targeting through ubiquination of K[34], may play a role. Indeed a preference for R may help to protect preproteins from degradation while they transit in the cytosol (Fig. 7a). It is of note that arginine features in consensus sequences of the cleavage sites[4,35], which thus may have been generated by K→R modification, potentially accounting for increased chloroplast-localization among cTP-N bearing constructs (Fig. 2 rows GH).

Unstructured sequences contribute to chloroplast determination

TP N-termini contribute to differential targeting[24]. In vascular plants, the presence of a multi-Arginine motif within the N-terminus of the peptide prevents chloroplast import[23]. Our data on a wider series of constructs suggest that chloroplast targeting specificity is provided by an unstructured sequence upstream of the amphipathic helix in cTP N-termini rather than by the mere absence of Arginines[23,36] (Fig. S22) or a difference in Hsp70 binding sites[2,27,28] (Fig. S25). Indeed, several HA-RAMPs that intrinsically contained unstructured N-termini proved able to support chloroplast targeting, even in the absence of a cTP-N addition.

We found chloroplast targeting was further improved by an unstructured C-terminus, in addition to the unstructured N-terminal element. Indeed mTP-C are more structured, containing a long predicted amphipathic helix. The need to contain unstructured sequences[13] as well as the increased length of cTPs, even extending beyond the cleavage site in many cases[10,21,22], appear mechanistically related to the import system (Fig. 7a): whereas mitochondrial import makes use of the proton gradient to power uptake of positively charged presequences[37,38], energized chloroplast import requires the cTP to stretch across both TOC and TIC and contact the translocation motor[2,39,40]. Structured sequence elements can thus impede import, including the helix at the Venus N-terminus[41]. HA-RAMPs with unstructured C-termini, such as SIM, were thus most likely to generate chloroplast targeting in the absence of an added TP-C. Unstructured elements also likely provide protein-protein interaction motifs. For instance, TOC-interaction has been attributed to semi-conserved 'FGLK' motifs[27,42–44], although the requirement for F appears to be relaxed

bioRxiv preprint doi: https://doi.org/10.1101/2021.12.03.471120; this version posted June 23, 2022. The copyright holder for this preprint (which was not certified by peer review) is the author/funder, who has granted bioRxiv a license to display the preprint in perpetuity. It is made available under aCC-BY-NC-ND 4.0 International license.

in Chlamydomonas (Fig. 4g)[45]. The presence of GLK sites with high predicted interactivity in cTP-N and cTP-C should contribute to the high chloroplast targeting potential of constructs equipped with both elements.

Amphipathic helices contribute to differential targeting

While N- and C-terminal elements aid specificity determination, particularly for chloroplast import, their influence fails to explain why some HA-RAMPs target preferentially the mitochondria or exclusively the chloroplast. This observation suggests that targeting specificity also is determined by some sequence properties of the amphipathic helical elements, which in the case of HA-RAMPs serve to mediate insertion into specific target membranes. It is of note that individual mTPs and cTPs also interact with membrane bilayers[12,18]. For instance, the Rubisco small subunit cTP interacts with chloroplast-mimetic membranes only in presence of the chloroplast-specific galactolipids[46]. Taken together these observations suggest that amphipathic helices may interact specifically with the membranes of the targeted organelle[6]. A direct interaction with the membrane bilayer, before that with proteins of the translocons, would provide a basic mechanism for a first step in differential organelle targeting (Fig. 7a). It could explain how TPs can be functionally specific whilst diverse in sequence.

A possible series of events for the evolution of targeting peptides

A small subset of randomly chosen sequences is able to inefficiently deliver proteins into extant mitochondria, relying on amphipathic helices[47,48]. Thus, the existing protein import machinery recognizes amphipathic helical peptides. However, an origin of TPs from random sequences does not explain how protein import into organelles would have spontaneously occurred in absence of the extant translocons.

Here, our use of antimicrobial peptides that harbor an amphipathic helix to further understand organelle targeting specificity, was inspired by the hypothesis that HA-RAMPs may have given rise to TPs during endosymbiotic organellogenesis because of an “import and destroy” mechanism from HA-RAMP-resistant bacteria[8,9]. In this context, combining the organelle-targeting behavior of all those constructs that convert antimicrobial into targeting peptides can be translated into a temporal evolutionary scenario (Fig. 7b) that adds to previously proposed models[37,48,50]. First, we found that several unaltered HA-RAMPs can deliver cargo, suggesting the evolution of mTPs from HA-RAMPs would have been straightforward. However,

bioRxiv preprint doi: https://doi.org/10.1101/2021.12.03.471120; this version posted June 23, 2022. The copyright holder for this preprint (which was not certified by peer review) is the author/funder, who has granted bioRxiv a license to display the preprint in perpetuity. It is made available under aCC-BY-NC-ND 4.0 International license.

K→R was found to reduce toxicity and increase targeting, a dual effect that would have produced a strong selection pressure favoring this exchange as an early step. Since mitochondria appear to tolerate the presence of preproteins containing unaltered HA-RAMPs, the addition of cleavage sites that allow presequences to be degraded separately from the cargo protein[49] would have come as a second step.

That chloroplast targeting requires additional discriminating elements is consistent with cTPs evolving in a cell that already had mTPs. There are two possible scenarios for the origin of cTPs. Firstly, cTPs might have evolved directly from HA-RAMPs that already contained unstructured sequence elements (Fig. 7b), as seen for our cp-set HA-RAMPs. Secondly, as has been suggested earlier[50], cTPs might have co-opted existing mTPs. According to the present scenario, these mTPs already contained R and a cleavage site, yet would still have been recognized by cyanobacterial HA-RAMP importers. In this case, the key innovation that generated cTPs may simply have been the addition of unstructured, possibly TOC-interacting elements to mTPs, which we showed here to be sufficient to retarget the mt-set HA-RAMPs equipped with TP C-termini at least partially to the chloroplast. The cTP N-terminus likely originally started with an F, given that in glaucophytes and rhodophytes (and many derived secondary plastids), a conserved N-terminal F plays a role in chloroplast import[20,31,51]. This observation led to the idea that cTPs may have originated from a re-use of a C-terminal F-based motif involved in secretion via OMP85 beta-barrel proteins[52,53] in (cyano)bacteria, from which TOC75 evolved. To this end, periplasmic POTRA domains responsible for substrate-recognition were proposed to have flipped orientation and now point into the host cytoplasm[54,55]. However, several studies of plant TOC75 have since consistently found POTRA-domains to be in the inter-membrane space, not the cytoplasm[56–58].

Note that the proposed scenario makes no prediction about whether host/proto-organelle interactions were mutualistic or antagonistic. Either way, antimicrobial peptides are likely to have been part of the suite of tools used in these host/proto-symbiont interactions. In particular, the role of antimicrobial peptides in mutualistic symbioses[59] includes one of the best documented cases for defensive antimicrobial peptide import into bacteria[60].

bioRxiv preprint doi: https://doi.org/10.1101/2021.12.03.471120; this version posted June 23, 2022. The copyright holder for this preprint (which was not certified by peer review) is the author/funder, who has granted bioRxiv a license to display the preprint in perpetuity. It is made available under aCC-BY-NC-ND 4.0 International license.

Conclusion

Investigating the steps required to generate TPs from HA-RAMPs has allowed us to uncover a number of novel mechanistic insights. Notably, we discovered a role for Arginines for targeting efficacy, and delineated the contributions of N- and C-terminal elements in targeting specificity. Our work also suggests that whether due to common descent or convergence, the similarities between TPs and HA-RAMPs point to TPs interacting with membrane lipids as an early targeting step. As any evolutionary scenario, including ours describing a plausible pathway from HA-RAMPs to TPs, it must be considered as a working hypothesis that will need to be assessed further by a series of bioinformatics and laboratory-controlled evolutionary experiments. Further understanding of peptide-lipid interactions and the phylogeny of import machinery components should shed new light on the evolution and functioning of organelle TPs.

Materials and Methods

Construct generation

Venus expression constructs were designed in SnapGene (v4.3.11) and generated by integrating PCR-amplified (Q5 hot start high-fidelity, #M0515, New England Biolabs) DNA fragments into plasmid pODC53[61] upstream of Venus using Gibson assembly (NEBuilder HiFi DNA assembly, #E5520S, New England Biolabs). Chlamydomonas TP sequences were amplified from genomic DNA extracted from strain T222+ (CC-5101). Templates for codon optimized HA-RAMP, RP and R→K modified TP sequences were obtained by gene synthesis (Eurofins Genomics). Correct assembly was verified by sequencing (Eurofins Genomics). Linear transformation cassettes were generated through restriction digest with *Eco*RV (New England Biolabs).

Transformation and fluorescence screen conditions

Constructs were transformed into wild-type strain T222+ (CC-5101) using the protocol described previously[62], except using 4µl of DNA at 2µg/µl. Transformants (≥24 per construct) selected for Paromomycin resistance were grown in 200µl TAP in 96-well plates under 50µmol photons m^{-2} s^{-2} for 3-5 days and then screened for Venus

bioRxiv preprint doi: https://doi.org/10.1101/2021.12.03.471120; this version posted June 23, 2022. The copyright holder for this preprint (which was not certified by peer review) is the author/funder, who has granted bioRxiv a license to display the preprint in perpetuity. It is made available under aCC-BY-NC-ND 4.0 International license.

475 expression in a fluorescence plate reader (CLARIOstar, BMG Labtech) as described
476 previously[61].

477 ***Microscopy***

478 Cells were grown in 96-well plates and epifluorescence microscopy was carried out as
479 described before[10]. Strains with suspected mitochondrial targeting were subjected to
480 0.1 µM MitoTracker Red CMXRos (ThermoFisher) in growth medium for 30 min in
481 the dark and washed with TAP prior to taking epifluorescence images with the same
482 settings as before[10], using a white light LED and a beam splitter at 535nm (423052-
483 0104-000, Zeiss) in combination with a custom-made filter set (559/34 BrightLine
484 HC, Beamsplitter T 585 LP, 607/36 BrightLine HC; AHF Analysentechnik AG) for
485 detecting the MitoTracker signal. Images were adjusted in Fiji[63] (ImgageJ version
486 2.0.0) as described before[10], and final figures assembled in PowerPoint (Microsoft
487 PowerPoint for Mac 2011, Version 14.6.3).

488 ***Western Blots***

489 Cells were grown up in liquid culture (10ml TAP, 30µmol photons m^{-2} s^{-1}, 160RPM)
490 until late mid-log phase. 2ml Aliquots were resuspended in 30µl storage buffer (1×
491 Roche cOmplete™ Mini proteinase inhibitor cocktail, 10 mM NaF, 0.2 M DTT, 0.2
492 M $NaCO_3$) and stored at -20°C. 20µl boiling buffer (1× Roche cOmplete™ Mini
493 proteinase inhibitor cocktail, 10mM NaF, 50 g/L SDS, 200 g/L sucrose) was added,
494 then aliquots were boiled (50 seconds). Cell debris was removed (tabletop centrifuge,
495 maximum speed, 15 minutes, 4°C). Chlorophyll content was estimated
496 spectrophotometrically: 1 µg chlorophyll $µl^{-1}$ = 0.11 × (OD_{680} – OD_{770}) for 5 µl
497 diluted in 1 ml water. Samples (10 µg chlorophyll, equal volumes) were run
498 (overnight, room temperature, 18A) on large gels (35×27cm; resolving gel: 12%
499 Acrylamide, 0.32% Bisacrylamide, 0.25 µl/ml Tetramethylethylenediamine, 250
500 mg/L Ammonium Persulfate, 375 mM Tris/HCl pH 8.8; stacking gel: 5%
501 Acrylamide, 0.133% Bisacrylamide, 0.666 µl/ml Tetramethylethylenediamine, 666
502 mg/L Ammonium Persulfate, 125 mM Tris/HCl pH 6.8). Proteins (<25kDa, >75kDa)
503 were transferred (0.1 µm nitrocellulose membranes, 1h, 0.8 A cm^{-2}) as follows:
504 cathode – 5 filter papers (FP, 3 mm, Whatman) soaked in transfer buffer 1 (40 mM
505 Aminocaproic acid, 20% Isopropanol, 25 mM Tris/HCl pH 9.4) – gel – membrane – 2
506 FPs soaked in transfer buffer 2 (20% Isopropanol, 25 mM Tris/HCl pH 10.4) – 3 FPs
507 soaked in transfer buffer 3 (20% Isopropanol, 300 mM Tris/HCl pH 10.4) – anode.

bioRxiv preprint doi: https://doi.org/10.1101/2021.12.03.471120; this version posted June 23, 2022. The copyright holder for this preprint (which was not certified by peer review) is the author/funder, who has granted bioRxiv a license to display the preprint in perpetuity. It is made available under aCC-BY-NC-ND 4.0 International license.

Membranes were fixed (Ponceau Red), incubated (1h, room temperature) in block (30 g/L skimmed milk powder, 0.1% tween-20, 1x PBS: 140 mM NaCl, 30 mM KCl, 100 mM Na_2HPO_4, 15 mM KH_2PO_4), immunolabelled (overnight, 4°C) using α-FLAG 1° (Sigma Aldrich F1804, diluted 1:10 000 in block), washed (0.1% tween-20, 1x PBS), treated (1h, room temperature) with horseradish peroxidase-conjugated α-mouse 2° (diluted 1:10 000 in block), washed, revealed (ECL; ChemiDoc, Biorad). Blots were processed using ImageLab (Version 6.0.0 build 26, BioRad), final figures were assembled in PowerPoint (Microsoft).

Antimicrobial activity assay

Minimum inhibitory concentration assays were performed as described before[10].

Sequence Data Set

TPs with experimentally-confirmed cleavage sites were recovered from proteomic studies: *Chlamydomonas reinhardtii* cTP (Terashima 2011), mTP (Tardif 2012); *Arabidopsis thaliana* cTP (Ge 2008, Rowland 2015), mTP (Huang 2009). For each peptide, we recovered the full-length protein sequence from NCBI and UNIPROT. Cytoplasmic control sequences were generated by taking N-terminal sequence stretches of random length, matching the distribution of peptide lengths observed in our Chlamydomonas TP dataset, from a random subset of Chlamydomonas proteins with a validated cytoplasmic location in UNIPROT. For PCAs and calculating amino acid frequencies, the same HA-RAMP, signal peptide and non-Chlamydomonas TP sequences were used as before[10].

Amphipathic helix prediction

Amphipatic α-helices are predicted as described previously[10], following the principle of the Heliquest algorithm[64]. Briefly, the approach aims to establish the longest sequence stretch that contains identifiable hydrophilic and hydrophobic faces. The algorithm is iterated such that multiple non-overlapping helices can be found within a given peptide (Fig. 1). Consequently, helix fractions are calculated as number of residues within all predicted helices divided by the total number of residues in the peptide; for evaluating the number of upstream residues, only the longest helix was considered (Fig. 6, Fig. S24).

bioRxiv preprint doi: https://doi.org/10.1101/2021.12.03.471120; this version posted June 23, 2022. The copyright holder for this preprint (which was not certified by peer review) is the author/funder, who has granted bioRxiv a license to display the preprint in perpetuity. It is made available under aCC-BY-NC-ND 4.0 International license.

ACC terms

In order to evaluate the physicochemical properties of our peptides we used the approach we previously described[10]. Briefly, each amino acid is described in terms of 3 'Z-scale' values[65] that can be interpreted as representing a residue's hydrophobic, steric and electronic properties. Auto-cross-covariances (ACC) between nearby residues are calculated up to a distance of four amino acids, generating a quantitative representation of a given peptide in terms of 36 ACC terms. Euclidian distances between HA-RAMP ACC term vectors and the barycenter of Chlamydomonas TPs were used as a measure of similarity (Table S1).

Visualization

We performed principal component analysis (PCA) to visualize the relationships between peptides as described by their 36 ACC terms (Fig. S1, S21) or by their 5 salient TP properties (Fig. S24) using python package sklearn v0.22.1[66].

Analysis of TP N-termini

TP N-termini, defined as the N-terminal 15 amino acids, were analysed (Fig. S22) as follows: Charge profiles were generated as described in the literature[27]. Hydrophobicity of TP N-termini was estimated using the Heliquest standalone application[64]. To evaluate disorder, we used IUpred2A, a software that calculates the probability for each residue of being in a disordered region[67]. We used the default 'Long' setting, which has been reported to be more accurate than the alternative 'Short' setting[68]. The disorder of a given sequence was taken as the mean of the probability values for each residue (average residue disorder probability).

Statistical prediction

To evaluate the predictive power of ACC terms[10] obtained for 15 residue-long TP N-termini with regards to localization (Fig. S22) we used a binomial logistic regression classifier. We performed one hundred 5-fold cross validation runs. In each set of one hundred runs, we randomly selected sequences such that the same number of mTPs and cTPs were used. For *C. reinhardtii* we used 33 mTP and 33 cTP and for *A. thaliana* we use 29 mTP and 29 cTP sequences. We used an elastic net penalty in a saga solver with an l1-ratio (a-parameter) of 0, which is equivalent to using only ridge penalty, where all features take part in the model, and a C parameter ($1/\lambda$) of 0.1. The a and $1/\lambda$ parameters were optimised with 10-fold cross validation. Firstly, when $1/\lambda =$

bioRxiv preprint doi: https://doi.org/10.1101/2021.12.03.471120; this version posted June 23, 2022. The copyright holder for this preprint (which was not certified by peer review) is the author/funder, who has granted bioRxiv a license to display the preprint in perpetuity. It is made available under aCC-BY-NC-ND 4.0 International license.

1, the best accuracy (0.82) was obtained with a between 0 and 0.09. Secondly, with a = 0, the best accuracy (0.82) was obtained with $1/\lambda = 0.1$. A Logistic Regression model with elastic net penalty ratio of 0.15 (scikit-learn Python package v0.22.1) trained on class I HA-RAMPs[10] and Chlamydomonas TPs was used to evaluate how similar potential HA-RAMP candidates are to TPs (Table S1). Custom scripts were written in python (v3.7.6).

Interaction site prediction

Values for the Boman index, a quantitative proxy for whether a peptide is more likely to interact with proteins (high values) or lipids (low values), were calculated as described in the literature[69]. Anchor2 interactivity values, a second proxy for protein interaction potential developed for disordered sequences[70], were calculated using the IUPred2A standalone application and webserver[67,71]. Interaction sites for Hsp70 were predicted as described by Ivey and coworkers[25] based on experimental affinity values for individual amino acids. Putatively TOC-interacting 'FGLK' sites were established by searching for presence of F and [P or G] and [K or R] and [A or L or V], and absence of [D and E], within each 8-residue window of a sequence, corresponding to rule 22 by Chotewutmontri and co-workers[27] that was recommended by the authors in personal communication. 'FGLK-1' sites were established the same way, but requiring the presence of only three of the four positive determinants. Custom scripts were implemented in R[72] (v3.6.1) using RStudio[73] (v1.2.1335).

Statistical analysis

Chlamydomonas TP distributions (Fig. 5, Fig. S25) were compared using two-sided t-tests (n=34 for mTPs and n=85 for cTPs), and associated mt-set and cp-set HA-RAMPs were compared using one-sided t-tests based on the trends set by TPs (n=3 for mt-set and n=5 for cp-set HA-RAMPs) in R[72] using RStudio[73]. Multiple Kruskal statistical tests are performed (same Chlamydomonas mTPs and cTPs as above, plus n=382 HA-RAMPs) to evaluate the distribution of amino acids (Fig. 3c, Fig. S20) in the different groups, followed by Dunn post-hoc tests (scipy v1.4.1).

Acknowledgements

Thank you to Tiffina Benhamou and Gabriel Chemin, who worked on aspects of this study with ODC during their summer internships. We also thank Prakitchai

bioRxiv preprint doi: https://doi.org/10.1101/2021.12.03.471120; this version posted June 23, 2022. The copyright holder for this preprint (which was not certified by peer review) is the author/funder, who has granted bioRxiv a license to display the preprint in perpetuity. It is made available under aCC-BY-NC-ND 4.0 International license.

Chotwutmontri and Barry Bruce for their help in correctly replicating their Hsp70-binding and FGLK-motif finding algorithms.

The following financial support is gratefully acknowledged: the Centre National de la Recherche Scientifique and Sorbonne University for annual funding to UMR7141; the Agence National de la Recherche for (a) "ChloroMitoRAMP" ANR grant (ANR-19-CE13-0009) and (b) "LabEx Dynamo" (ANR-LABX-011), both of which provided postdoctoral support to ODC, and (c) "MATHTEST" grant (ANR-18-CE13-0027) which provided doctoral support to CG; finally, the Fondation Edmond Rothschild which provided complementary financial support to ODC and CG. The funders had no role in the design of the study; in the collection, analyses, or interpretation of data; in the writing of the manuscript, or in the decision to publish the results.

Author contributions

FAW, IL and YC conceptualized the project and acquired funds. ODC devised, conducted and visualized the wet-lab experimental part of the investigation, and was chiefly responsible for assigning subcellular localization interpretations based on microscopic evidence. CG carried out the dry-lab/bioinformatic part of the investigation and associated visualization under the supervision of IL, writing custom software to do so (ODC contributed to the analysis of FGLK and Hsp70-binding sites). ODC wrote the original draft of the manuscript. FAW, IL, ODC and YC reviewed and edited the manuscript. All authors approved the final manuscript. The authors declare no competing interests.

Data availability

All data are available in the main text or the supplementary materials. Custom code generated in the course of this project will be made available without restrictions upon request to the authors. All constructs will be made available through the Chlamydomonas resource centre.

References

1. Wiedemann, N., and Pfanner, N. (2017). Mitochondrial Machineries for Protein Import and Assembly. Annu. Rev. Biochem. *86*, 685–714.

bioRxiv preprint doi: https://doi.org/10.1101/2021.12.03.471120; this version posted June 23, 2022. The copyright holder for this preprint (which was not certified by peer review) is the author/funder, who has granted bioRxiv a license to display the preprint in perpetuity. It is made available under aCC-BY-NC-ND 4.0 International license.

2. Chotewutmontri, P., Holbrook, K., and Bruce, B.D. (2017). Plastid Protein Targeting: Preprotein Recognition and Translocation. Int. Rev. Cell Mol. Biol. *330*, 227–294.

3. Bruce, B.D. (2001). The paradox of plastid transit peptides: Conservation of function despite divergence in primary structure. Biochim. Biophys. Acta - Mol. Cell Res. *1541*, 2–21.

4. Tardif, M., Atteia, A., Specht, M., Cogne, G., Rolland, N., Brugière, S., Hippler, M., Ferro, M., Bruley, C., Peltier, G., et al. (2012). Predalgo: A new subcellular localization prediction tool dedicated to green algae. Mol. Biol. Evol. *29*, 3625–3639.

5. Armenteros, J.J.A., Salvatore, M., Emanuelsson, O., Winther, O., Von Heijne, G., Elofsson, A., and Nielsen, H. (2019). Detecting sequence signals in targeting peptides using deep learning. Life Sci. Alliance *2*, 1–14.

6. Lazzaro, B.P., Zasloff, M., and Rolff, J. (2020). Antimicrobial peptides: Application informed by evolution. Science *368*.

7. Joo, H.S., Fu, C.I., and Otto, M. (2016). Bacterial strategies of resistance to antimicrobial peptides. Philos. Trans. R. Soc. B Biol. Sci. *371*.

8. Wollman, F.-A. (2016). An antimicrobial origin of transit peptides accounts for early endosymbiotic events. Traffic *17*, 1322–1328.

9. Caspari, O.D., and Lafontaine, I. (2021). The role of antimicrobial peptides in the evolution of endosymbiotic protein import. PLoS Pathog. *17*, e1009466.

10. Garrido, C., Caspari, O.D., Choquet, Y., Wollman, F.A., and Lafontaine, I. (2020). Evidence Supporting an Antimicrobial Origin of Targeting Peptides to Endosymbiotic Organelles. Cells *9*, 1795.

11. von Heijne, G. (1986). Mitochondrial targeting sequences may form amphiphilic helices. EMBO J. *5*, 1335–1342.

12. von Heijne, G., Steppuhn, J., and Herrmann, R.G. (1989). Domain structure of mitochondrial and chloroplastic targeting peptides. Eur. J. Biochem. *180*, 535–545.

13. von Heijne, G., and Nishikawa, K. (1991). Chloroplast transit peptides. The perfect random coil? FEBS Lett. *278*, 1–3.

14. Franzén, L.-G.G., Rochaix, J.-D.D., and von Heijne, G. (1990). Chloroplast transit peptides from the green alga Chlamydomonas reinhardtii share features with both mitochondrial and higher plant chloroplast presequences. FEBS Lett.

bioRxiv preprint doi: https://doi.org/10.1101/2021.12.03.471120; this version posted June 23, 2022. The copyright holder for this preprint (which was not certified by peer review) is the author/funder, who has granted bioRxiv a license to display the preprint in perpetuity. It is made available under aCC-BY-NC-ND 4.0 International license.

260, 169–172.

15. Lancelin, J.M., Gans, P., Bouchayer, E., Bally, I., Arlaud, G.J., and Jacquot, J.P. (1996). NMR structures of a mitochondrial transit peptide from the green alga Chlamydomonas reinhardtii. FEBS Lett. *391*, 203–208.
16. Krimm, I., Gans, P., Hernandez, J.F., Arlaud, G.J., and Lancelin, J.M. (1999). A coil-helix instead of a helix-coil motif can be induced in a chloroplast transit peptide from Chlamydomonas reinhardtii. Eur. J. Biochem. *265*, 171–180.
17. Wienk, H.L.J., Wechselberger, R.W., Czisch, M., and De Kruijff, B. (2000). Structure, Dynamics, and Insertion of a Chloroplast Targeting Peptide in Mixed Micelles. Biochemistry *39*, 8219–8227.
18. Bruce, B.D. (1998). The role of lipids in plastid protein transport. Plant Mol. Biol. *38*, 223–46.
19. Teixeira, P.F., and Glaser, E. (2013). Processing peptidases in mitochondria and chloroplasts. Biochim. Biophys. Acta - Mol. Cell Res. *1833*, 360–370.
20. Köhler, D., Dobritzsch, D., Hoehenwarter, W., Helm, S., Steiner, J.M., and Baginsky, S. (2015). Identification of protein N-termini in Cyanophora paradoxa cyanelles: transit peptide composition and sequence determinants for precursor maturation. Front. Plant Sci. *6*, 1–11.
21. Bionda, T., Tillmann, B., Simm, S., Beilstein, K., Ruprecht, M., and Schleiff, E. (2010). Chloroplast import signals: The length requirement for translocation in vitro and in vivo. J. Mol. Biol. *402*, 510–523.
22. Caspari, O.D. (2021). Chloroplast transit peptides often require downstream unstructured sequence in Chlamydomonas reinhardtii. bioRxiv, doi:10.1101/2021.11.26.470094.
23. Lee, D.W., Lee, S., Lee, J., Woo, S., Razzak, M.A., Vitale, A., and Hwang, I. (2019). Molecular Mechanism of the Specificity of Protein Import into Chloroplasts and Mitochondria in Plant Cells. Mol. Plant.
24. Bhushan, S., Kuhn, C., Berglund, A., Roth, C., and Glaser, E. (2006). The role of the N-terminal domain of chloroplast targeting peptides in organellar protein import and miss-sorting. FEBS *580*, 3966–3972.
25. Ivey, R. a, Subramanian, C., and Bruce, B.D. (2000). Identification of a Hsp70 recognition domain within the rubisco small subunit transit peptide. Plant Physiol. *122*, 1289–1299.
26. Ivey, R. a, and Bruce, B.D. (2000). In vivo and in vitro interaction of DnaK

bioRxiv preprint doi: https://doi.org/10.1101/2021.12.03.471120; this version posted June 23, 2022. The copyright holder for this preprint (which was not certified by peer review) is the author/funder, who has granted bioRxiv a license to display the preprint in perpetuity. It is made available under aCC-BY-NC-ND 4.0 International license.

and a chloroplast transit peptide. Cell Stress Chaperones *5*, 62–71.

27. Chotewutmontri, P., Reddick, L.E., McWilliams, D.R., Campbell, I.M., and Bruce, B.D. (2012). Differential Transit Peptide Recognition during Preprotein Binding and Translocation into Flowering Plant Plastids. Plant Cell *24*, 3040–3059.

28. Chotewutmontri, P., and Bruce, B.D. (2015). Non-native, N-terminal Hsp70 molecular motor recognition elements in transit peptides support plastid protein translocation. J. Biol. Chem. *290*, 7602–7621.

29. Caspari, O.D. (2022). Chloroplast transit peptides often require downstream unstructured sequence in Chlamydomonas reinhardtii. Front. Plant Sci. *13*, 825797.

30. Meyer, M., Itakura, A., Patena, W., Wang, L., He, S., Emrich-Mills, T., Lau, C.S., Yates, G., Mackinder, L.C.M., and Jonikas, M.C. (2020). Assembly of the algal CO2-fixing organelle, the pyrenoid, is guided by a Rubisco-binding motif. Sci. Adv. *6*, eabd2408.

31. Patron, N.J., and Waller, R.F. (2007). Transit peptide diversity and divergence : a global analysis of plastid targeting signals. BioEssays *29*, 1048–1058.

32. Li, L., Vorobyov, I., and Allen, T.W. (2013). The different interactions of lysine and arginine side chains with lipid membranes. J. Phys. Chem. B *117*, 11906–11920.

33. Li, J., Koh, J.-J., Liu, S., Lakshminarayanan, R., Verma, C.S., and Beuerman, R.W. (2017). Membrane Active Antimicrobial Peptides: Translating Mechanistic Insights to Design. Front. Neurosci. *11*, 1–18.

34. Mattiroli, F., and Sixma, T.K. (2014). Lysine-targeting specificity in ubiquitin and ubiquitin-like modification pathways. Nat. Struct. Mol. Biol. *21*, 308–316.

35. Calvo, S.E., Julien, O., Clauser, K.R., Shen, H., Kamer, K.J., Wells, J.A., and Mootha, V.K. (2017). Comparative analysis of mitochondrial N-termini from mouse, human, and yeast. Mol. Cell. Proteomics *16*, 512–523.

36. Lee, D.W., Lee, S., Min, C.-K., Park, C., Kim, J.-M., Hwang, C.-S., Park, S.K., Cho, N.-H., and Hwang, I. (2020). Cross-Species Functional Conservation and Possible Origin of the N-Terminal Specificity Domain of Mitochondrial Presequences. Front. Plant Sci. *11*, 1–7.

37. Garg, S.G., and Gould, S.B. (2016). The Role of Charge in Protein Targeting Evolution. Trends Cell Biol. *26*, 894–905.

bioRxiv preprint doi: https://doi.org/10.1101/2021.12.03.471120; this version posted June 23, 2022. The copyright holder for this preprint (which was not certified by peer review) is the author/funder, who has granted bioRxiv a license to display the preprint in perpetuity. It is made available under aCC-BY-NC-ND 4.0 International license.

733 38. Martin, J., Mahlke, K., and Pfanner, N. (1991). Role of an energized inner
734 membrane in mitochondrial protein import: ΔΨ drives the movement of
735 presequences. J. Biol. Chem. *266*, 18051–18057.
736 39. Nakai, M. (2018). New Perspectives on Chloroplast Protein Import. Plant Cell
737 Physiol. *59*, 1111–1119.
738 40. Richardson, L.G.L., Small, E.L., Inoue, H., and Schnell, D.J. (2018). Molecular
739 topology of the transit peptide during chloroplast protein import. Plant Cell *30*,
740 1789–1806.
741 41. Rekas, A., Alattia, J.R., Nagai, T., Miyawaki, A., and Ikura, M. (2002). Crystal
742 structure of venus, a yellow fluorescent protein with improved maturation and
743 reduced environmental sensitivity. J. Biol. Chem. *277*, 50573–50578.
744 42. Holbrook, K., Subramanian, C., Chotewutmontri, P., Reddick, L.E., Wright, S.,
745 Zhang, H., Moncrief, L., and Bruce, B.D. (2016). Functional Analysis of Semi-
746 conserved Transit Peptide Motifs and Mechanistic Implications in Precursor
747 Targeting and Recognition. Mol. Plant *9*, 1286–1301.
748 43. Pilon, M., Wienk, H., Sips, W., De Swaaf, M., Talboom, I., Van't Hof, R., De
749 Korte- Kool, G., Demel, R., Weisbeek, P., and De Kruijff, B. (1995).
750 Functional domains of the ferredoxin transit sequence involved in chloroplast
751 import. J. Biol. Chem. *270*, 3882–3893.
752 44. Lee, D.W., Lee, S., Oh, Y.J., and Hwang, I. (2009). Multiple sequence motifs
753 in the rubisco small subunit transit peptide independently contribute to Toc159-
754 dependent import of proteins into chloroplasts. Plant Physiol. *151*, 129–141.
755 45. Razzak, A., Lee, D.W., Yoo, Y., and Hwang, I. (2017). Evolution of rubisco
756 complex small subunit transit peptides from algae to plants. Sci. Rep. *7*, 9279.
757 46. Pinnaduwage, P., and Bruce, B.D. (1996). In vitro interaction between a
758 chloroplast transit peptide and chloroplast outer envelope lipids is sequence-
759 specific and lipid class-dependent. J. Biol. Chem. *271*, 32907–32915.
760 47. Baker, A., and Schatz, G. (1987). Sequences from a prokaryotic genome or the
761 mouse dihydrofolate reductase gene can restore the import of a truncated
762 precursor protein into yeast mitochondria. Proc. Natl. Acad. Sci. *84*, 3117–
763 3121.
764 48. Lemire, B.D., Fankhauser, C., Baker, A., and Schatz, G. (1989). The
765 mitochondrial targeting function of randomly generated peptide sequences
766 correlates with predicted helical amphiphilicity. J. Biol. Chem. *264*, 20206–

bioRxiv preprint doi: https://doi.org/10.1101/2021.12.03.471120; this version posted June 23, 2022. The copyright holder for this preprint (which was not certified by peer review) is the author/funder, who has granted bioRxiv a license to display the preprint in perpetuity. It is made available under aCC-BY-NC-ND 4.0 International license.

20215.

49. Kmiec, B., Teixeira, P.F., and Glaser, E. (2014). Shredding the signal: targeting peptide degradation in mitochondria and chloroplasts. Trends Plant Sci. *19*, 771–8.

50. Lee, D.W., and Hwang, I. (2021). Understanding the evolution of endosymbiotic organelles based on the targeting sequences of organellar proteins. New Phytol. *230*, 924–930.

51. Wunder, T., Martin, R., Löffelhardt, W., Schleiff, E., and Steiner, J.M. (2007). The invariant phenylalanine of precursor proteins discloses the importance of Omp85 for protein translocation into cyanelles. BMC Evol. Biol. *7*, 236.

52. Robert, V., Volokhina, E.B., Senf, F., Bos, M.P., Van Gelder, P., and Tommassen, J. (2006). Assembly factor Omp85 recognizes its outer membrane protein substrates by a species-specific C-terminal motif. PLoS Biol. *4*, 1984–1995.

53. Knopp, M., Garg, S.G., Handrich, M., and Gould, S.B. (2020). Major Changes in Plastid Protein Import and the Origin of the Chloroplastida. iScience *23*, 100896.

54. Sommer, M.S., Daum, B., Gross, L.E., Weis, B.L.M., Mirus, O., Abram, L., Maier, U.G., Kühlbrandt, W., and Schleiff, E. (2011). Chloroplast Omp85 proteins change orientation during evolution. Proc. Natl. Acad. Sci. U. S. A. *108*, 13841–13846.

55. Bullmann, L., Haarmann, R., Mirus, O., Bredemeier, R., Hempel, F., Maier, U.G., and Schleiff, E. (2010). Filling the gap, evolutionarily conserved Omp85 in plastids of chromalveolates. J. Biol. Chem. *285*, 6848–6856.

56. Paila, Y.D., Richardson, L.G.L., Inoue, H., Parks, E.S., McMahon, J., Inoue, K., and Schnell, D.J. (2016). Multi-functional roles for the polypeptide transport associated domains of Toc75 in chloroplast protein import. Elife *5*, 1–29.

57. Chen, Y.L., Chen, L.J., and Li, H.M. (2016). Polypeptide transport-associated domains of the Toc75 channel protein are located in the intermembrane space of chloroplasts. Plant Physiol. *172*, 235–243.

58. Gross, L.E., Spies, N., Simm, S., and Schleiff, E. (2020). Toc75-V/OEP80 is processed during translocation into chloroplasts, and the membrane-embedded form exposes its POTRA domain to the intermembrane space. FEBS Open Bio

bioRxiv preprint doi: https://doi.org/10.1101/2021.12.03.471120; this version posted June 23, 2022. The copyright holder for this preprint (which was not certified by peer review) is the author/funder, who has granted bioRxiv a license to display the preprint in perpetuity. It is made available under aCC-BY-NC-ND 4.0 International license.

10, 444–454.

59. Mergaert, P. (2018). Role of antimicrobial peptides in controlling symbiotic bacterial populations. Nat. Prod. Rep. *35*, 336–356.

60. Guefrachi, I., Pierre, O., Timchenko, T., Alunni, B., Barrière, Q., Czernic, P., Villaécija-Aguilar, J.-A., Verly, C., Bourge, M., Fardoux, J., et al. (2015). Bradyrhizobium BclA Is a Peptide Transporter Required for Bacterial Differentiation in Symbiosis with Aeschynomene Legumes. Mol. Plant-Microbe Interact. *28*, 1155–1166.

61. Caspari, O.D. (2020). Introduction of a leaky stop codon as molecular tool in Chlamydomonas reinhardtii. PLoS One *15*, e0237405.

62. Onishi, M., and Pringle, J.R. (2016). Robust Transgene Expression from Bicistronic mRNA in the Green Alga *Chlamydomonas reinhardtii*. G3 (Bethesda). *6*, 4115–4125.

63. Schindelin, J., Arganda-Carreras, I., Frise, E., Kaynig, V., Longair, M., Pietzsch, T., Preibisch, S., Rueden, C., Saalfeld, S., Schmid, B., et al. (2012). Fiji: an open-source platform for biological-image analysis. Nat. Methods *9*, 676–682.

64. Gautier, R., Douguet, D., Antonny, B., and Drin, G. (2008). HELIQUEST: a web server to screen sequences with specific alpha-helical properties. Bioinformatics *24*, 2101–2102.

65. Hellberg, S., Sjostrom, M., Skagerberg, B., and Wold, S. (1987). Peptide Quantitative Structure-Activity Relationships, a Multivariate Approach. J. Med. Chem. *30*, 1126–1135.

66. Pedregosa, F., Varoquaux, G., Gramfort, A., Michel, V., Thirion, B., Grisel, O., Blondel, M., Prettenhofer, P., Weiss, R., Dubourg, V., et al. (2011). Scikit-learn: Machine Learning in Python. J. Mach. Learn. Res. *12*, 2825–2830.

67. Erdős, G., and Dosztányi, Z. (2020). Analyzing Protein Disorder with IUPred2A. Curr. Protoc. Bioinforma. *70*, 1–15.

68. Nielsen, J.T., and Mulder, F.A.A. (2019). Quality and bias of protein disorder predictors. Sci. Rep. *9*, 1–11.

69. Boman, H.G. (2003). Antibacterial peptides: basic facts and emerging concepts. J. Intern. Med. *254*, 197–215.

70. Mészáros, B., Simon, I., and Dosztányi, Z. (2009). Prediction of Protein Binding Regions in Disordered Proteins. PLoS One *5*, e1000376.

bioRxiv preprint doi: https://doi.org/10.1101/2021.12.03.471120; this version posted June 23, 2022. The copyright holder for this preprint (which was not certified by peer review) is the author/funder, who has granted bioRxiv a license to display the preprint in perpetuity. It is made available under aCC-BY-NC-ND 4.0 International license.

71. Mészáros, B., Erdös, G., and Dosztányi, Z. (2018). IUPred2A: Context-dependent prediction of protein disorder as a function of redox state and protein binding. Nucleic Acids Res. *46*, W329–W337.

72. R Core Team (2019). R: A Language and Environment for Statistical Computing.

73. RStudio Team (2020). RStudio: Integrated Development for R.

bioRxiv preprint doi: https://doi.org/10.1101/2021.12.03.471120; this version posted June 23, 2022. The copyright holder for this preprint (which was not certified by peer review) is the author/funder, who has granted bioRxiv a license to display the preprint in perpetuity. It is made available under aCC-BY-NC-ND 4.0 International license.

Figures and legends

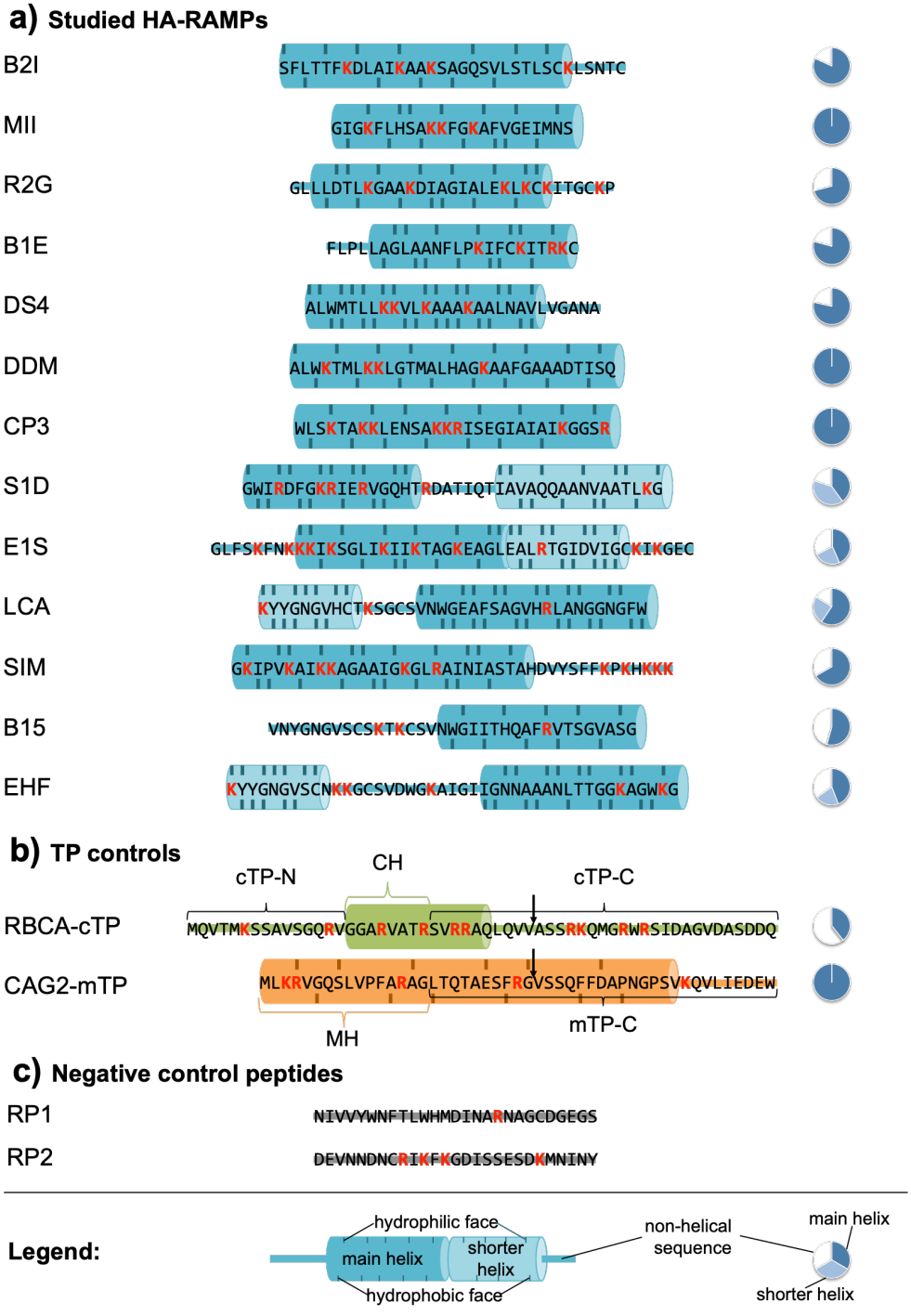

Fig. 1. Peptide sequences under study. Amino acid sequences are shown using the one-letter code. Positively charged residues are highlighted in red. The fraction of the sequence predicted to fold into amphipathic helices (see Methods) is provided by a pie-chart to the right of the sequence; for TPs in (**b**) this was calculated up to the cleavage site indicated by a downward arrow. Predicted amphipathic helices are highlighted using a cylinder cartoon, with residues contributing to the hydrophilic/hydrophobic face indicated on the top/bottom. No helix could be

bioRxiv preprint doi: https://doi.org/10.1101/2021.12.03.471120; this version posted June 23, 2022. The copyright holder for this preprint (which was not certified by peer review) is the author/funder, who has granted bioRxiv a license to display the preprint in perpetuity. It is made available under aCC-BY-NC-ND 4.0 International license.

predicted within RBCA-cTP, and thus the indicated helix is taken from a published NMR-structure obtained in membrane-mimetic conditions[16]. Note that the two helices of E1S are at an angle to each other and therefore cannot form a single continuous amphipathic helix. Abbreviations: (**a**) B2I: Brevinin-2ISb, R2G: Ranatuerin-2G, MII: Magainin 2, B1E: Brevinin-1E, DS4: Dermaseptin S4, DDM: Dermadistinctin-M, CP3: Cecropin-P3, S1D: Sarcotoxin-1D, E1S: Esculentin-1SEA, LCA: Leucocin-A, SIM: SI Moricin, B15: Bacillocin 1580, EHF: Enterocin HF; (**b**) TP – targeting peptide, cTP: chloroplast TP, mTP: mitochondrial TP, RBCA: Rubisco activase, CAG2: γ-carbonic anhydrase, cTP-N: cTP N-terminal element, CH: cTP helix, MH: mTP helix, cTP-C: cTP C-terminal element, mTP-C: mTP C-terminal element; (**C**) RP: random peptide.

bioRxiv preprint doi: https://doi.org/10.1101/2021.12.03.471120; this version posted June 23, 2022. The copyright holder for this preprint (which was not certified by peer review) is the author/funder, who has granted bioRxiv a license to display the preprint in perpetuity. It is made available under aCC-BY-NC-ND 4.0 International license.

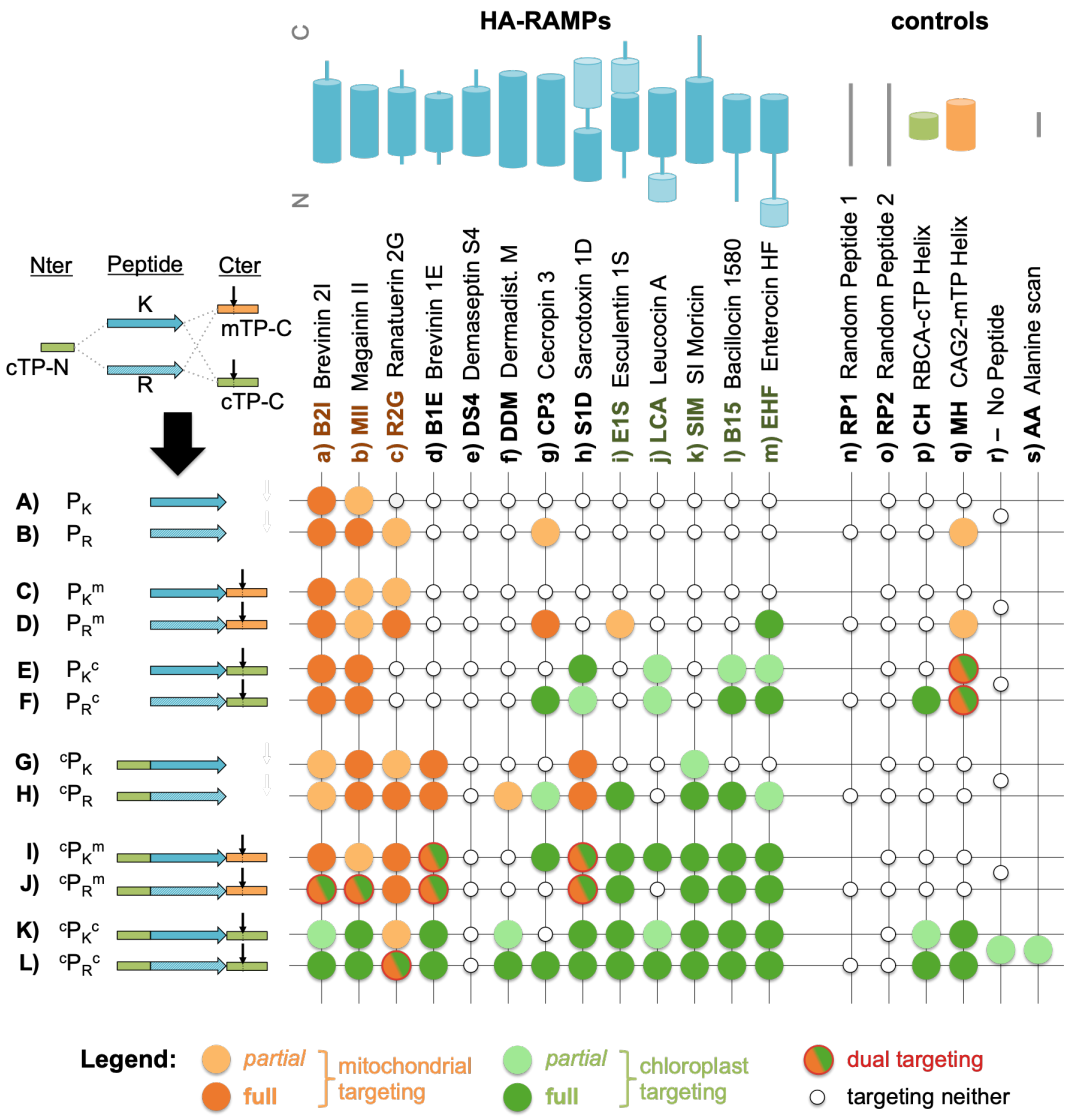

Fig. 2. TP modifications enable HA-RAMP targeting. Chimeric constructs were generated by combining TP elements with HA-RAMPs (see Fig. 1 for sequences; in the ^{c}AA^{c} construct in column s, all residues of the helical element "CH" within RBCA-cTP are replaced by Alanines). The overview graph shows in each column (**a-s**) one of the peptides with a cartoon indicating the position of the predicted amphipathic helices within the sequence; and in each row (**A-L**) a combination of peptide, K/R modification, addition of cTP-N (the 15 N-terminal residues upstream of the helix in RBCA-cTP) and/or a C-terminal TP element (cTP-C or mTP-C, which include -10 residues upstream and +23 residues downstream of the cleavage site for RBCA-cTP and CAG2-mTP respectively) indicated by a cartoon and the following shorthand: P = peptide, $_{K}$ = contains mostly Lysines, $_{R}$ = contains mostly Arginines, ^{m} = mTP element, ^{c} = cTP element (^{c}P = cTP-N, P^{c} = cTP-C). In each case, an overview of observed targeting is provided by a colour code (see figure legend). Images for all

bioRxiv preprint doi: https://doi.org/10.1101/2021.12.03.471120; this version posted June 23, 2022. The copyright holder for this preprint (which was not certified by peer review) is the author/funder, who has granted bioRxiv a license to display the preprint in perpetuity. It is made available under aCC-BY-NC-ND 4.0 International license.

878 constructs are shown in Fig. S2-S19. Note that the present results for $B2I_K^c$, MII_K^c,
879 $S1D_K^c$, $B15_K^c$ and EHF_K^c (row E, columns a,b,h,l,m) confirmed our previous report
880 on these strains[10].
881

bioRxiv preprint doi: https://doi.org/10.1101/2021.12.03.471120; this version posted June 23, 2022. The copyright holder for this preprint (which was not certified by peer review) is the author/funder, who has granted bioRxiv a license to display the preprint in perpetuity. It is made available under aCC-BY-NC-ND 4.0 International license.

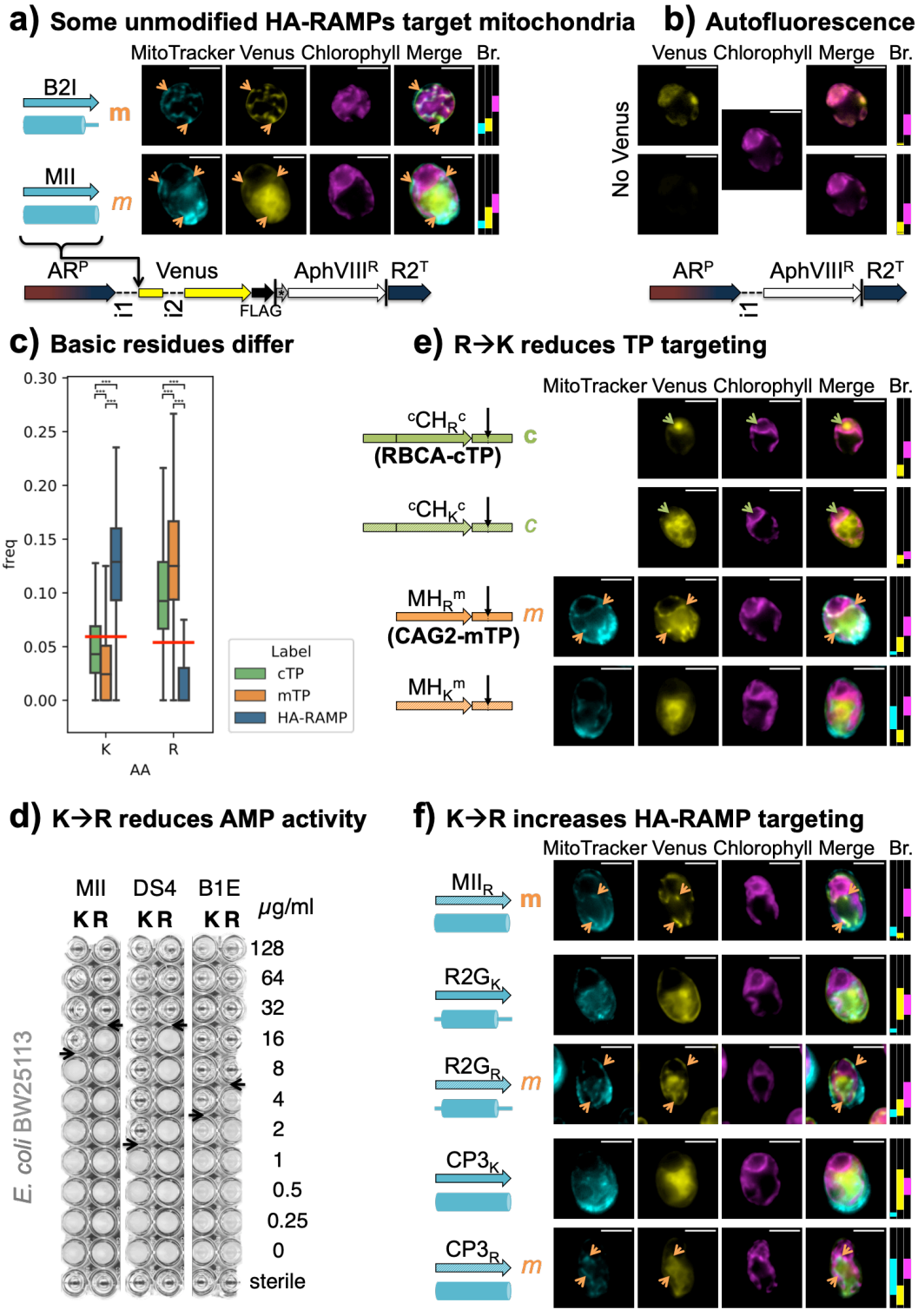

Fig. 3. K is for killing, R is for targeting. (**a**) Indicated peptides were inserted upstream of a Venus fluorescent protein reporter in a bicistronic expression system for Chlamydomonas[61]. AR^{P}: hybrid *HSP70a-RBCS2* promoter, i1: *RBCS2* intron 1, i2: *RBCS2* intron 2, FLAG: FLAG-tag, |: stop codon, *: bicistronic bridge sequence tagcat, AphVIII^{R}: Paromomycin resistance gene, R2^{T}: *RBCS2* terminator. Epifluorescence microscopy images of selected examples are shown. False-coloured

bioRxiv preprint doi: https://doi.org/10.1101/2021.12.03.471120; this version posted June 23, 2022. The copyright holder for this preprint (which was not certified by peer review) is the author/funder, who has granted bioRxiv a license to display the preprint in perpetuity. It is made available under aCC-BY-NC-ND 4.0 International license.

889 yellow fluorescence from the Venus channel reports on the subcellular localization of
890 the fluorescent reporter. MitoTracker fluorescence, false-coloured in cyan, indicates
891 the position of mitochondria (although parts of the cell exterior are sometimes also
892 stained), with salient features highlighted with orange arrows to indicate co-
893 localisation with the Venus channel. Chlorophyll autofluorescence, shown in
894 magenta, indicates the location of the chloroplast. Scale bars are 5µm. Refer to Fig. 1
895 for sequences and Fig. S2 and S3 for biological replicates. Where a construct was
896 interpreted as generating reporter localization in mitochondria or chloroplast, this is
897 indicated by an orange 'm' or a green 'c' respectively, in bold for full targeting or in
898 italics for partial targeting. Brightness (Br.) was adjusted for clarity: fluorescence
899 intensity values were restricted to the range shown for each channel by matching
900 coloured rectangles. Intensity scales to 0 at the bottom of the panel, and to 65535 at
901 the top. (**b**) A 'no Venus' control strain, expressing an empty vector, is shown with
902 two different Venus channel brightness settings to visualize chloroplast
903 autofluorescence in the Venus channel. Autofluorescence intensity is typically below
904 2000, indicated by a black dotted line in Brightness rectangles. Therefore, if Venus
905 channel brightness is adjusted below 2000, autofluorescence originating from the
906 chloroplast may be misinterpreted as Venus located in the chloroplast. **(c)** Lysine (K)
907 and Arginine (R) frequencies for Chlamydomonas TPs and HA-RAMPs are shown as
908 boxplots (center line: median; box limits: upper and lower quartiles; whiskers:
909 min/max values within 1.5x interquartile range). To give a baseline for comparison,
910 their average across the UNIPROT database is given as red horizontal line.
911 Statistically significant differences are indicated with stars: (Multiple Kruskal-Wallis
912 tests followed by Dunn post-hoc tests, ***$p<0.0001$). See Fig. S20 for all amino
913 acids. (**d**) Grayscale photos of antimicrobial activity growth assays in the presence of
914 dilutions of three selected antimicrobial peptides against *E. coli* strain BW25113
915 show reduced activity when natively K-rich sequences (K, left hand columns) are
916 altered by replacing all Ks by Rs (R, right hand columns). (**e,f**) Epifluorescence
917 images of selected chimeric (**e**) TP control or (**f**) HA-RAMP constructs are shown as
918 in (a). MH: mTP helical fragment, CH: cTP helical fragment.
919

bioRxiv preprint doi: https://doi.org/10.1101/2021.12.03.471120; this version posted June 23, 2022. The copyright holder for this preprint (which was not certified by peer review) is the author/funder, who has granted bioRxiv a license to display the preprint in perpetuity. It is made available under aCC-BY-NC-ND 4.0 International license.

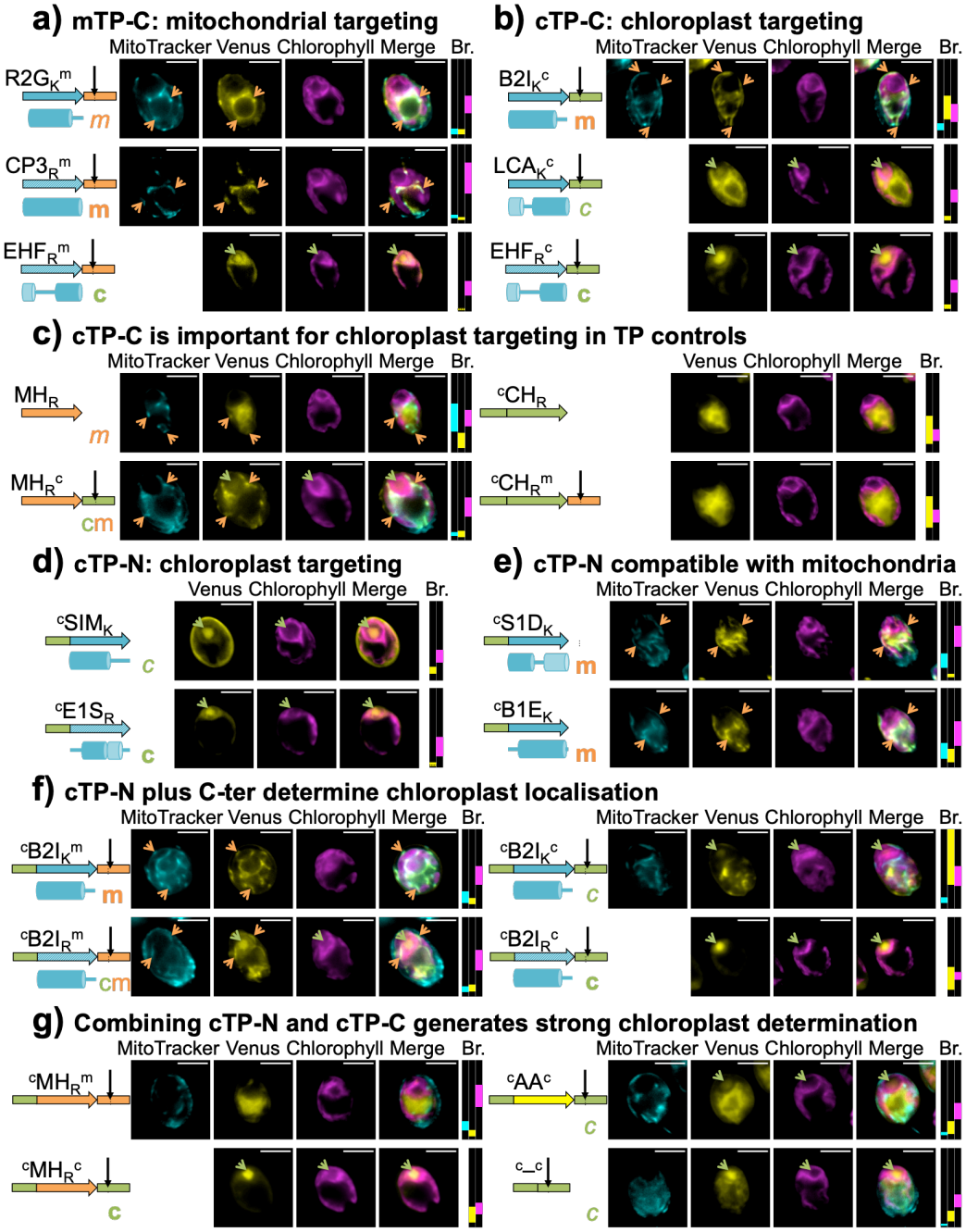

Fig. 4. TP N- and C-termini enable chloroplast targeting by HA-RAMPs. Exemplary epifluorescence images are shown as in Fig. 3; same convention as in Fig. 3 for Venus localisation. The result for B2I$_K^c$ in (**b**) confirms our previous report on this construct[10].

bioRxiv preprint doi: https://doi.org/10.1101/2021.12.03.471120; this version posted June 23, 2022. The copyright holder for this preprint (which was not certified by peer review) is the author/funder, who has granted bioRxiv a license to display the preprint in perpetuity. It is made available under aCC-BY-NC-ND 4.0 International license.

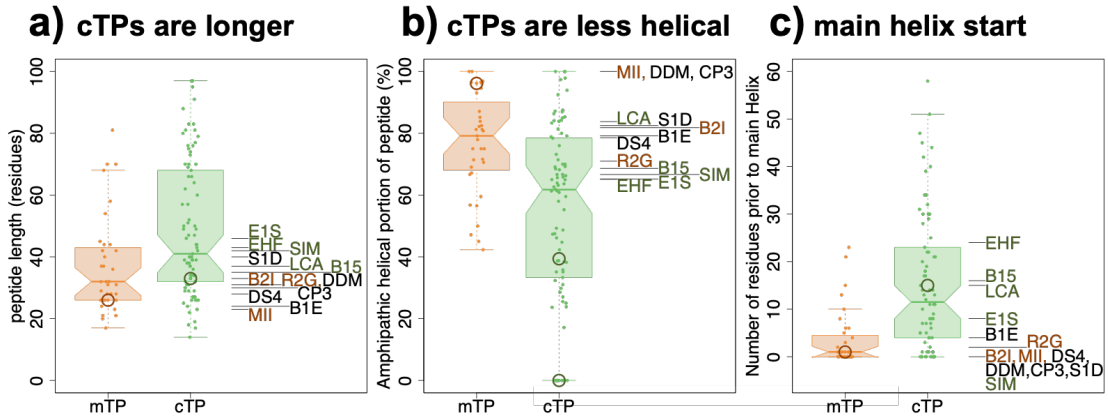

Fig. 5. Chloroplast and mitochondrial targeting HA-RAMPs match cTPs and mTPs respectively. For salient properties, Chlamydomonas mTPs and cTPs are compared to our 13 HA-RAMPs. TP distributions are shown as boxplots (center line: median; box limits: upper and lower quartiles; whiskers: min/max values within 1.5x interquartile range), coloured points represent individual peptides. The position of the CAG2-mTP and RBCA-cTP is circled in each graph. The non-zero value for RBCA-cTP in (B) and the single circle in (C) report on the amphipathic helix established by an NMR-study[16], since no helix could be predicted by our approach. HA-RAMPs are colour-coded by preferred targeting: orange = mt-set; green = cp-set (cf. Fig. 2). (**a**) cTPs are significantly longer than mTPs (p=0.0017), and cp-set are longer than mt-set HA-RAMPs (p=0.0184). (**b**) Helices make up a significantly smaller fraction of cTPs than mTPs (p<0.0001), and HA-RAMPs show a similar trend (0.1122). (**c**) cTPs contain significantly longer sequence stretches upstream of the longest predicted helix than mTPs (p<0.0001), as do cp-set compared to mt-set HA-RAMPs (p=0.0205). Reported p-values were obtained through two-way t-tests for TPs and one-way t-tests for HA-RAMPs.

bioRxiv preprint doi: https://doi.org/10.1101/2021.12.03.471120; this version posted June 23, 2022. The copyright holder for this preprint (which was not certified by peer review) is the author/funder, who has granted bioRxiv a license to display the preprint in perpetuity. It is made available under aCC-BY-NC-ND 4.0 International license.

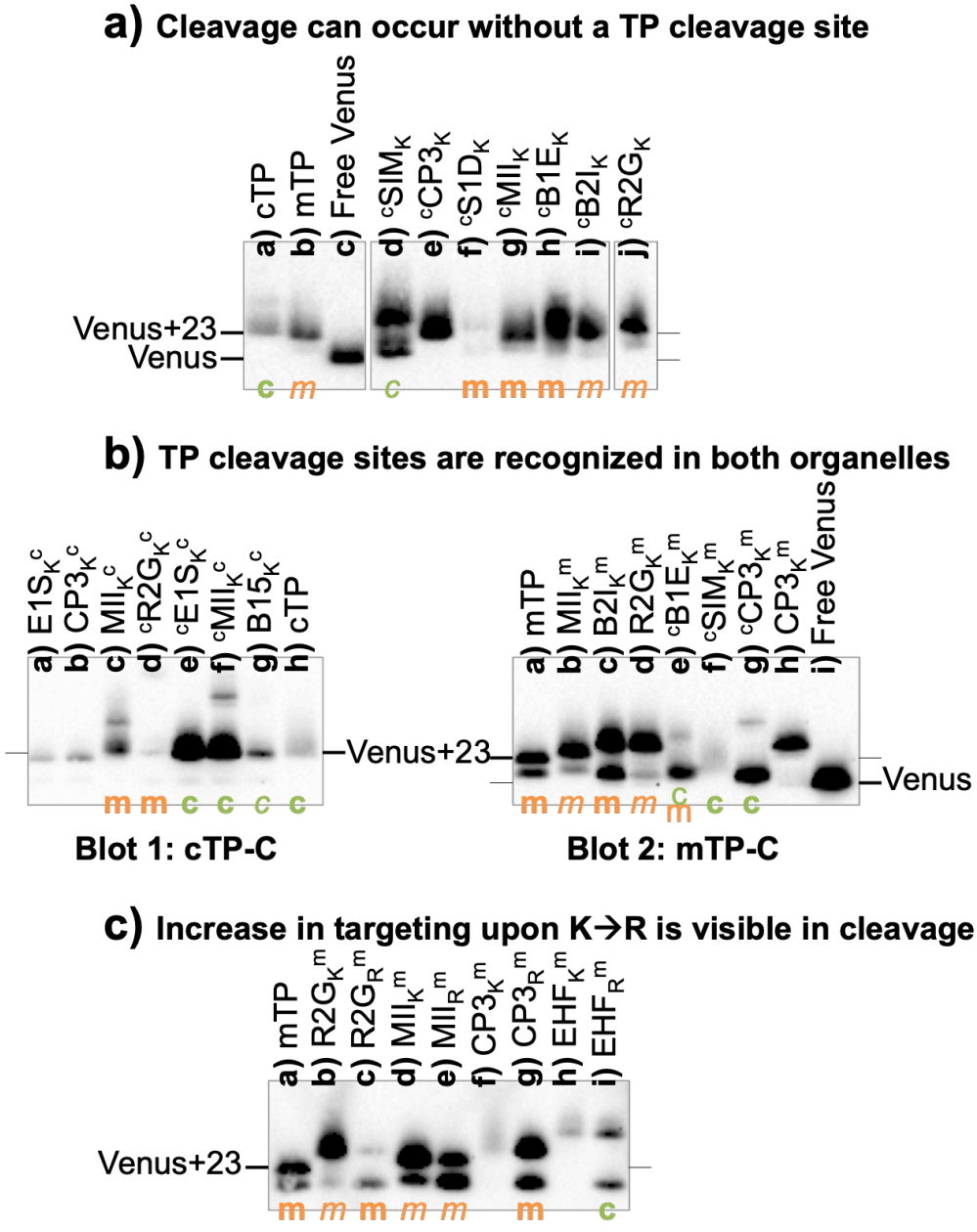

Fig. 6. Import is associated with maturation of the preprotein. Western Blots used an α-FLAG antibody on selected constructs as indicated above blots. Where a construct was interpreted as generating reporter localization by fluorescence microscopy (cf. Fig. 2, Fig. S2-S19) in mitochondria or chloroplast, this is indicated by an orange 'm' or a green 'c' respectively, in bold for full targeting or in italics for partial targeting. In (**a**) some lanes were spliced for clarity; the uncropped blot is provided in Fig. S27.

bioRxiv preprint doi: https://doi.org/10.1101/2021.12.03.471120; this version posted June 23, 2022. The copyright holder for this preprint (which was not certified by peer review) is the author/funder, who has granted bioRxiv a license to display the preprint in perpetuity. It is made available under aCC-BY-NC-ND 4.0 International license.

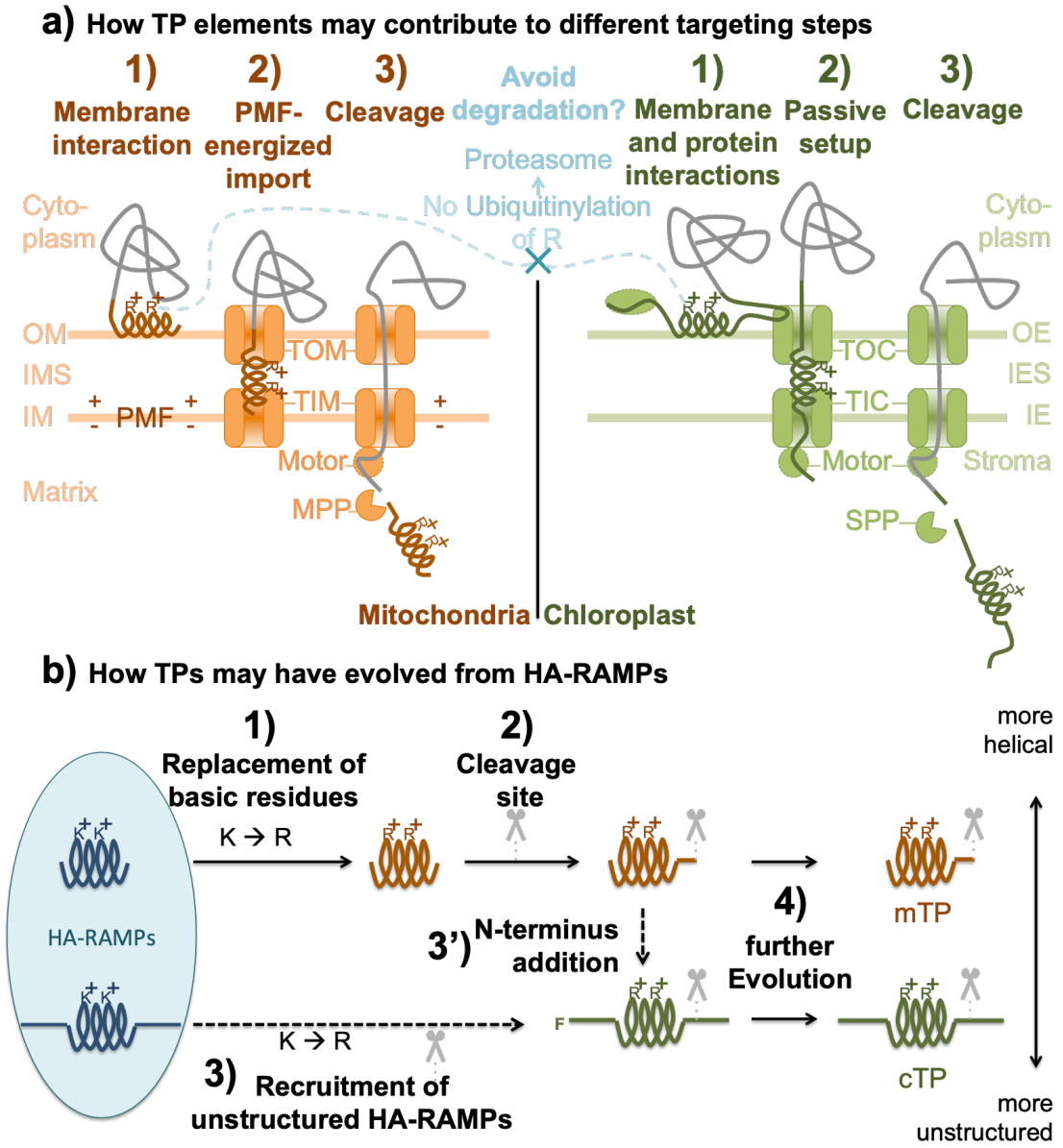

Fig. 7. Proposed functioning and evolution of TPs. Abbreviations: OM – outer membrane, IMS – inter-membrane space, IM – inner membrane, OE – outer envelope, IES – inter-envelope space, IE – inner envelope, PMF – proton motive force, TOM – translocon of the outer mitochondrial membrane, TIM – translocon of the inner mitochondrial membrane, TOC – translocon of the outer chloroplast envelope, TIC – translocon of the inner chloroplast envelope, MPP – matrix processing peptidase, SPP – stromal processing peptidase, R – Arginine, K – Lysine, F – Phenylalanine, mTP – mitochondrial targeting peptide, cTP – chloroplast transit peptide. (**a**) A number of roles for TP elements during protein import are suggested. Since ubiquitinilation targets K residues, a preference for R in TPs may increase preprotein stability. R may also play a role in lipid interactions. (1) membrane

bioRxiv preprint doi: https://doi.org/10.1101/2021.12.03.471120; this version posted June 23, 2022. The copyright holder for this preprint (which was not certified by peer review) is the author/funder, who has granted bioRxiv a license to display the preprint in perpetuity. It is made available under aCC-BY-NC-ND 4.0 International license.

interactions may play a role in enabling differential targeting due to organelle-specific lipid preferences of TP helices. Protein interactions by cTP N- and C-terminal elements, e.g. with cytosolic factors or TOC-components (subunits are not shown for simplicity), may also play a role in specific targeting. (2) Import of positively-charged mTPs across IM is energized by the PMF. By contrast, a passive setup is required for cTPs to allow N-termini to reach into the stroma and contact the motor complex, likely contributing to increased length and relatively unstructured N- and C-termini of cTPs. (3) Sequence elements contributing to targeting may be present downstream of cleavage sites in cTPs. (**b**) If TPs evolved from AMPs, 1) HA-RAMPs would have first changed K to R and 2) acquired a cleavage site to become mTPs. To generate cTPs, either 3) more unstructured HA-RAMPs were recruited directly to become cTPs by undergoing a K to R shift and acquiring a cleavage site separately, or 3') mTPs acquired an N-terminal non-helical domain. Early cTP N-termini likely contained a starting F[51]. 4) Further evolution would have reinforced the differences between cTPs and mTPs to limit mis-targeting.

bioRxiv preprint doi: https://doi.org/10.1101/2021.12.03.471120; this version posted June 23, 2022. The copyright holder for this preprint (which was not certified by peer review) is the author/funder, who has granted bioRxiv a license to display the preprint in perpetuity. It is made available under aCC-BY-NC-ND 4.0 International license.

981 **Supporting Information**

982 **Table S1** Similarity of HA-RAMPs to TPs quantified (in Excel file)

983 **Table S2** Numeric values derived of bioinformatic analyses (in Excel file)

984

985

bioRxiv preprint doi: https://doi.org/10.1101/2021.12.03.471120; this version posted June 23, 2022. The copyright holder for this preprint (which was not certified by peer review) is the author/funder, who has granted bioRxiv a license to display the preprint in perpetuity. It is made available under aCC-BY-NC-ND 4.0 International license.

Fig. S1. HA-RAMP candidates cover a diversity of physico-chemical properties. A Principal component analysis (PCA) based on auto-cross-correllated (ACC) Z-scale values reflects divergent physico-chemical properties of Signal Peptides (SP: bacterial secretory peptides – bSP, thylakoid signal peptides – tSP, eukaryotic signal peptides – eSP) relative to Targeting Peptides (TP: chloroplast transit peptides – cTP, mitochondrial targeting peptides – mTP) and helical-amphipathic ribosomally-produced antimicrobial peptides (HA-RAMP, shown here are class I HA-RAMPs *sensu* Garrido *et al.*[10]). Axes are principal components (PC) 1 and 2. Each dot represents one peptide; the 13 HA-RAMP candidates studied in this article are highlighted in red. Convex areas include the 50% of peptides at the centre of each distribution.

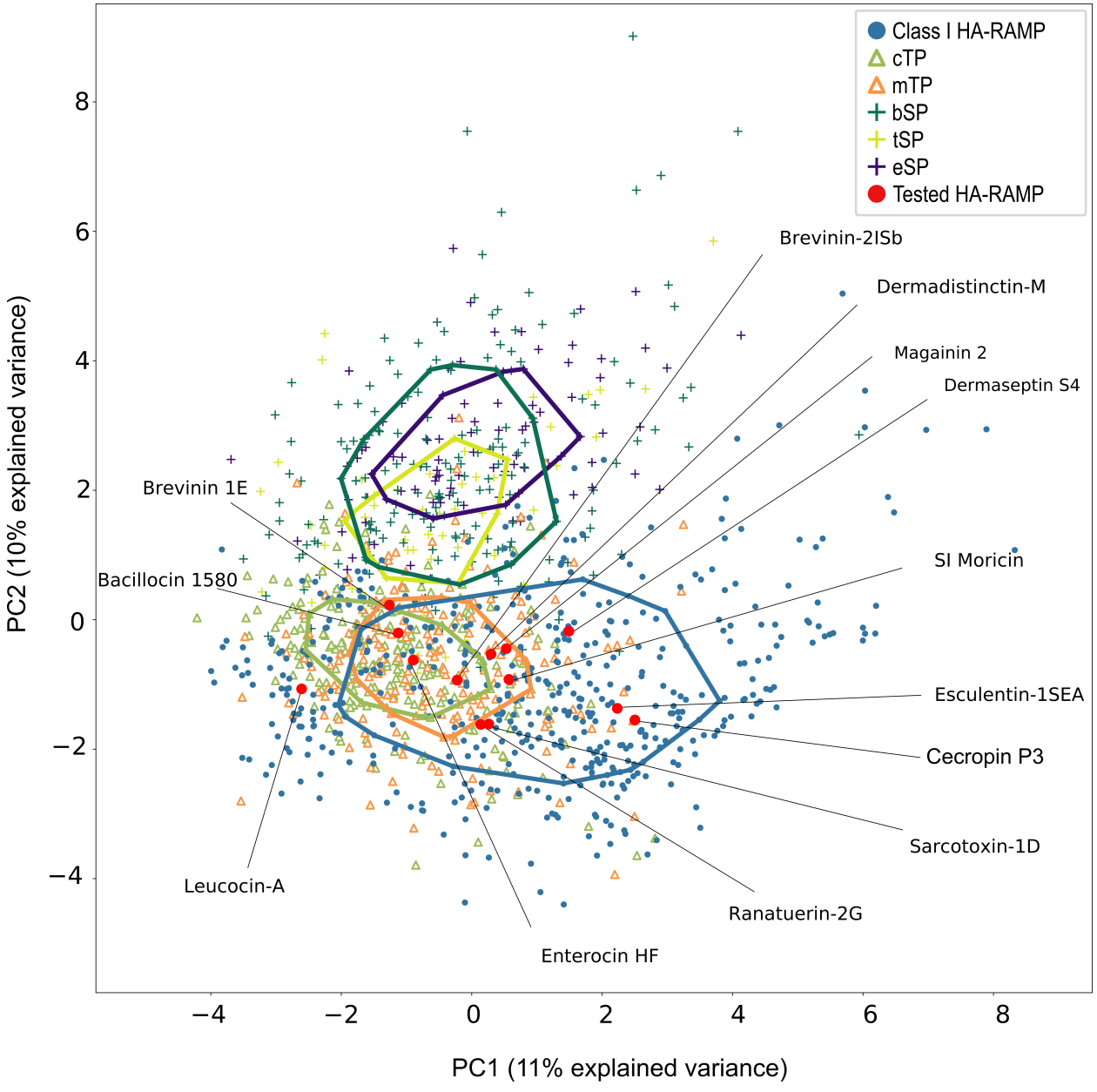

bioRxiv preprint doi: https://doi.org/10.1101/2021.12.03.471120; this version posted June 23, 2022. The copyright holder for this preprint (which was not certified by peer review) is the author/funder, who has granted bioRxiv a license to display the preprint in perpetuity. It is made available under aCC-BY-NC-ND 4.0 International license.

Fig. S2. Microscopy for biological replicates of Brevinin 2ISb. Three independent transformant lines (Strains 1-3) are shown for each combination of modifications (A-L), represented by a cartoon and a shorthand description (cf. Fig. 2). Where a construct was interpreted as generating reporter localization in mitochondria or chloroplast, this is indicated by an orange 'm' or a green 'c' respectively, in bold for full targeting or in italics for partial targeting. Scale bars are 5µm.

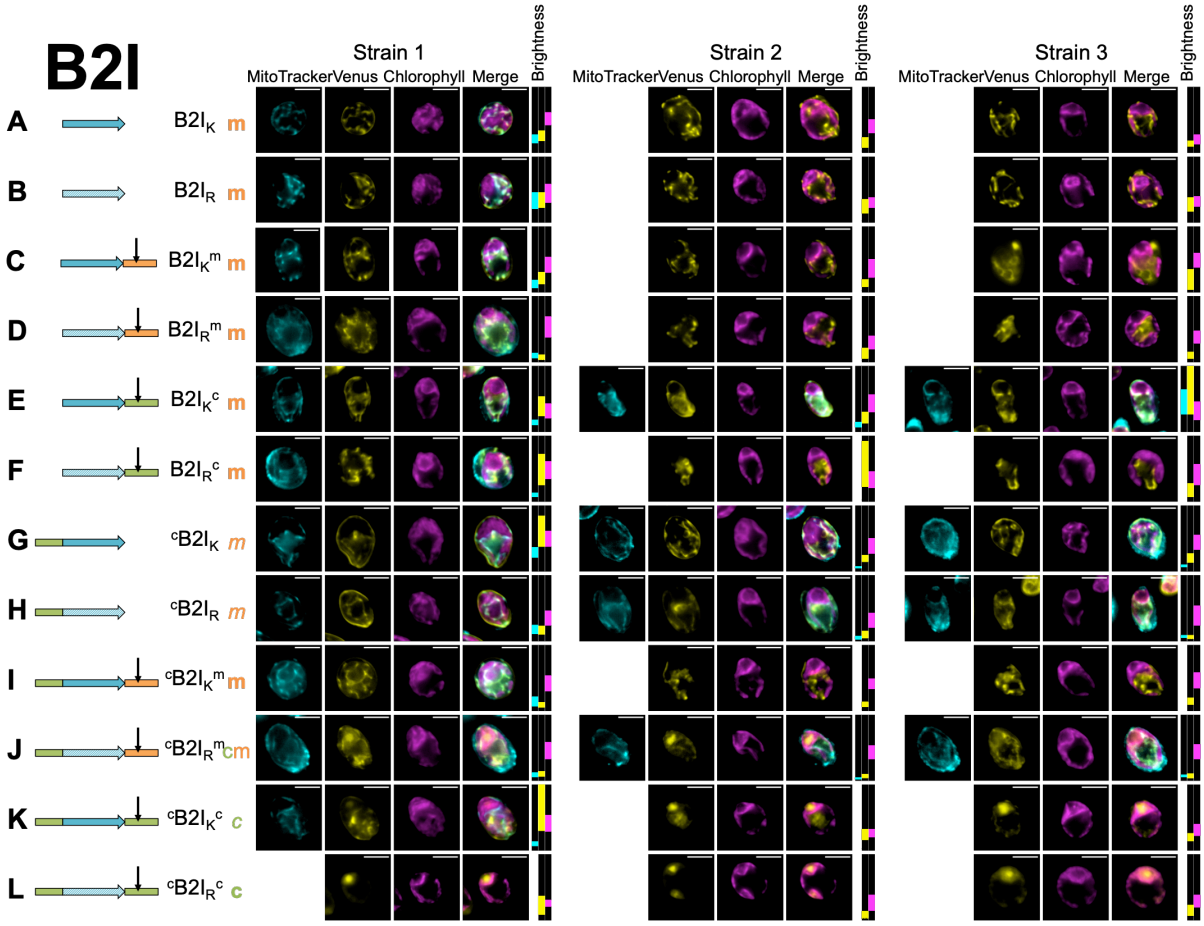

bioRxiv preprint doi: https://doi.org/10.1101/2021.12.03.471120; this version posted June 23, 2022. The copyright holder for this preprint (which was not certified by peer review) is the author/funder, who has granted bioRxiv a license to display the preprint in perpetuity. It is made available under aCC-BY-NC-ND 4.0 International license.

Fig. S3. Microscopy for biological replicates of Magainin 2. Three independent transformant lines (Strains 1-3) are shown for each combination of modifications (A-L), represented by a cartoon and a shorthand description (cf. Fig. 2). Where a construct was interpreted as generating reporter localization in mitochondria or chloroplast, this is indicated by an orange 'm' or a green 'c' respectively, in bold for full targeting or in italics for partial targeting. Scale bars are 5µm.

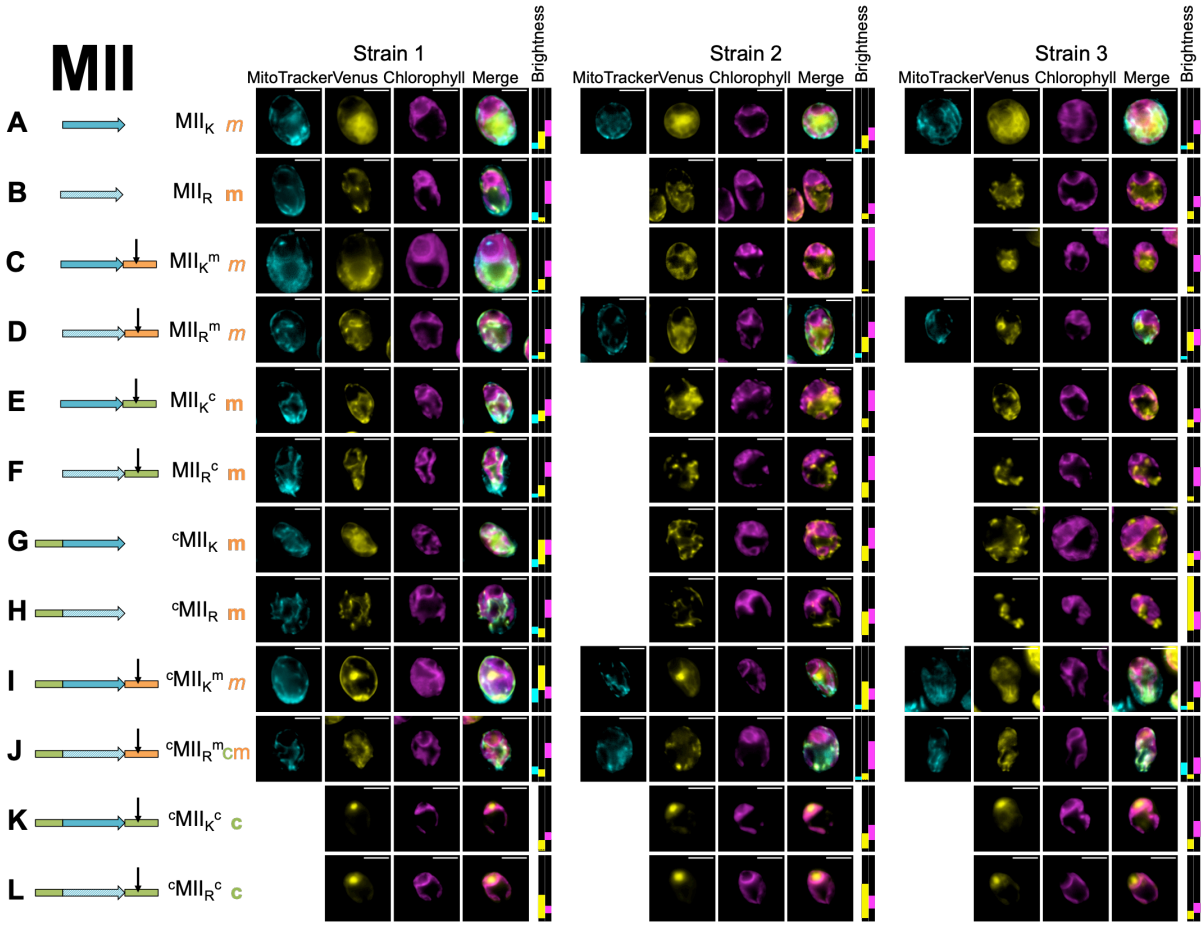

bioRxiv preprint doi: https://doi.org/10.1101/2021.12.03.471120; this version posted June 23, 2022. The copyright holder for this preprint (which was not certified by peer review) is the author/funder, who has granted bioRxiv a license to display the preprint in perpetuity. It is made available under aCC-BY-NC-ND 4.0 International license.

Fig. S4. Microscopy for biological replicates of Ranatuerin 2G. Three independent transformant lines (Strains 1-3) are shown for each combination of modifications (A-L), represented by a cartoon and a shorthand description (cf. Fig. 2). Where a construct was interpreted as generating reporter localization in mitochondria or chloroplast, this is indicated by an orange 'm' or a green 'c' respectively, in bold for full targeting or in italics for partial targeting. Scale bars are 5µm.

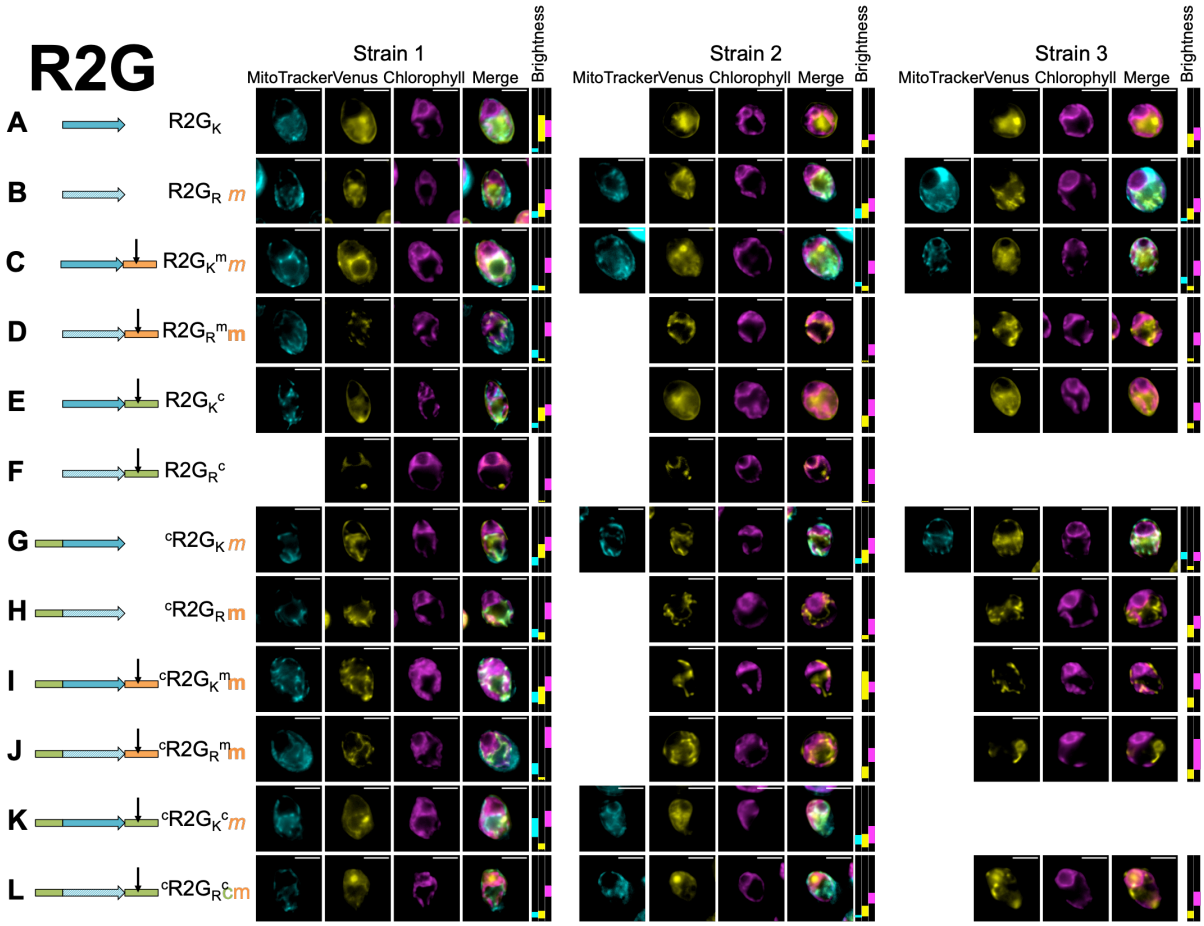

bioRxiv preprint doi: https://doi.org/10.1101/2021.12.03.471120; this version posted June 23, 2022. The copyright holder for this preprint (which was not certified by peer review) is the author/funder, who has granted bioRxiv a license to display the preprint in perpetuity. It is made available under aCC-BY-NC-ND 4.0 International license.

Fig. S5. Microscopy for biological replicates of Brevinin 1E. Three independent transformant lines (Strains 1-3) are shown for each combination of modifications (A-L), represented by a cartoon and a shorthand description (cf. Fig. 2). Where a construct was interpreted as generating reporter localization in mitochondria or chloroplast, this is indicated by an orange 'm' or a green 'c' respectively, in bold for full targeting or in italics for partial targeting. Scale bars are 5µm.

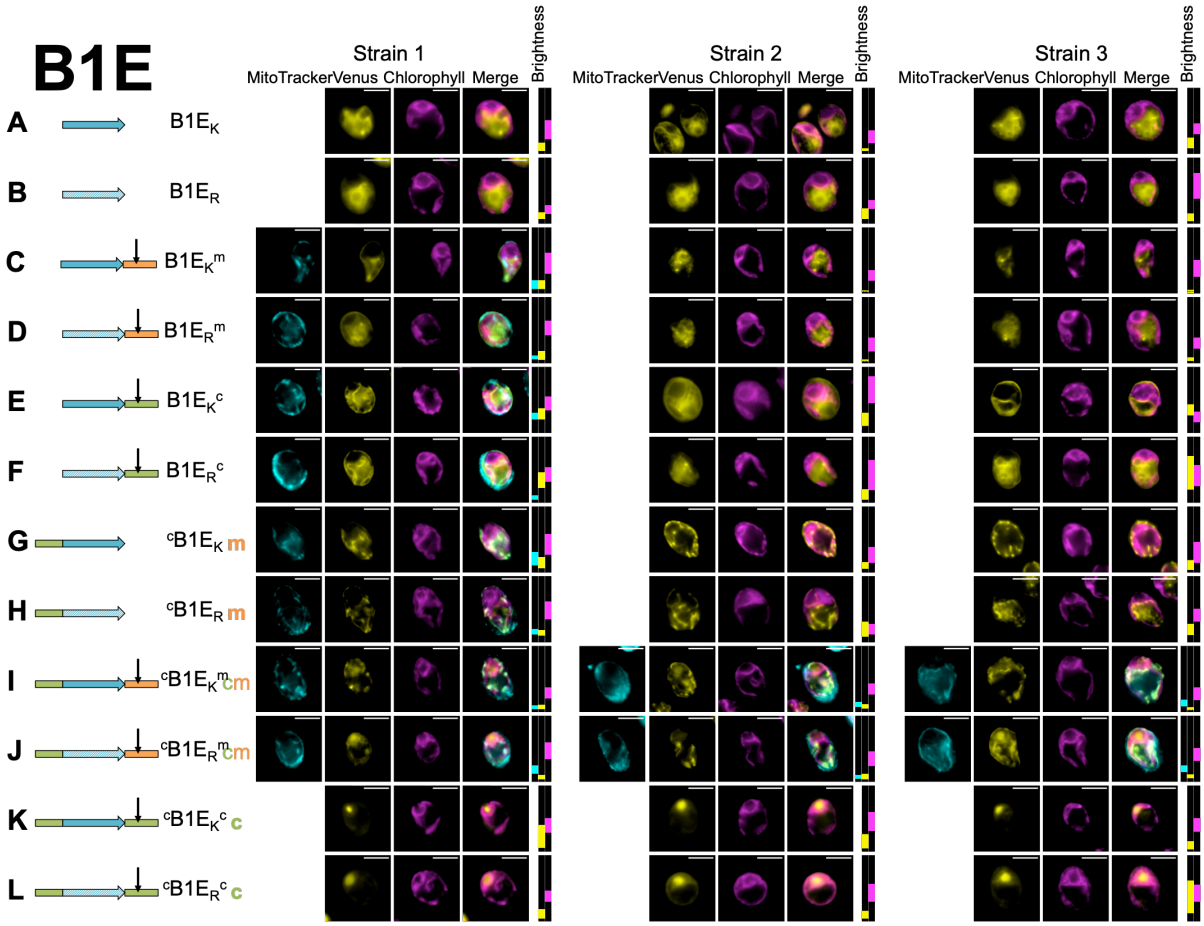

bioRxiv preprint doi: https://doi.org/10.1101/2021.12.03.471120; this version posted June 23, 2022. The copyright holder for this preprint (which was not certified by peer review) is the author/funder, who has granted bioRxiv a license to display the preprint in perpetuity. It is made available under aCC-BY-NC-ND 4.0 International license.

Fig. S6. Microscopy for biological replicates of Dermaseptin S4. Three independent transformant lines (Strains 1-3) are shown for each combination of modifications (A-L), represented by a cartoon and a shorthand description (cf. Fig. 2). Where a construct was interpreted as generating reporter localization in mitochondria or chloroplast, this is indicated by an orange 'm' or a green 'c' respectively, in bold for full targeting or in italics for partial targeting. Scale bars are 5µm.

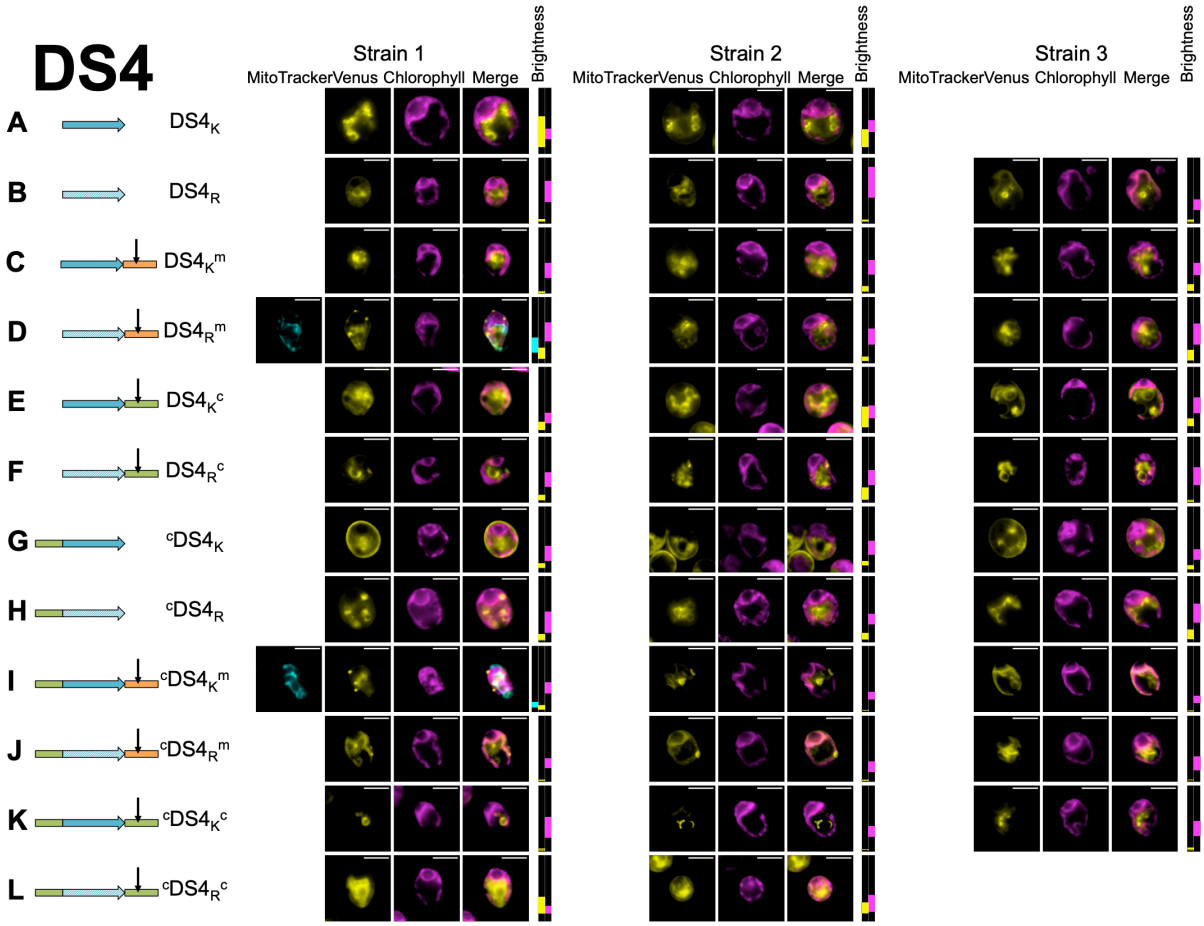

bioRxiv preprint doi: https://doi.org/10.1101/2021.12.03.471120; this version posted June 23, 2022. The copyright holder for this preprint (which was not certified by peer review) is the author/funder, who has granted bioRxiv a license to display the preprint in perpetuity. It is made available under aCC-BY-NC-ND 4.0 International license.

Fig. S7. Microscopy for biological replicates of Dermadistinctin M. Three independent transformant lines (Strains 1-3) are shown for each combination of modifications (A-L), represented by a cartoon and a shorthand description (cf. Fig. 2). Where a construct was interpreted as generating reporter localization in mitochondria or chloroplast, this is indicated by an orange 'm' or a green 'c' respectively, in bold for full targeting or in italics for partial targeting. Scale bars are 5µm.

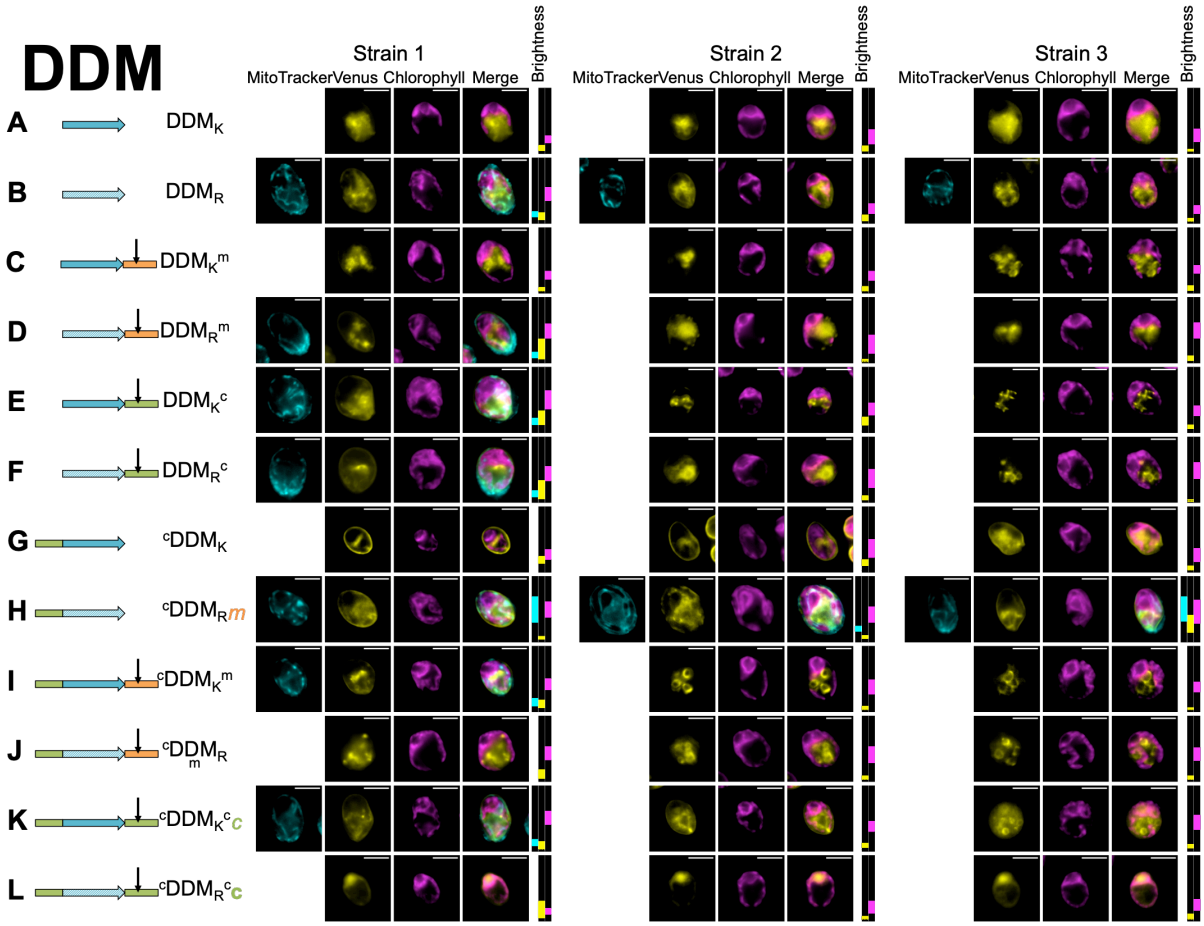

bioRxiv preprint doi: https://doi.org/10.1101/2021.12.03.471120; this version posted June 23, 2022. The copyright holder for this preprint (which was not certified by peer review) is the author/funder, who has granted bioRxiv a license to display the preprint in perpetuity. It is made available under aCC-BY-NC-ND 4.0 International license.

Fig. S8. Microscopy for biological replicates of Cecropin P3. Three independent transformant lines (Strains 1-3) are shown for each combination of modifications (A-L), represented by a cartoon and a shorthand description (cf. Fig. 2). Where a construct was interpreted as generating reporter localization in mitochondria or chloroplast, this is indicated by an orange 'm' or a green 'c' respectively, in bold for full targeting or in italics for partial targeting. Scale bars are 5µm.

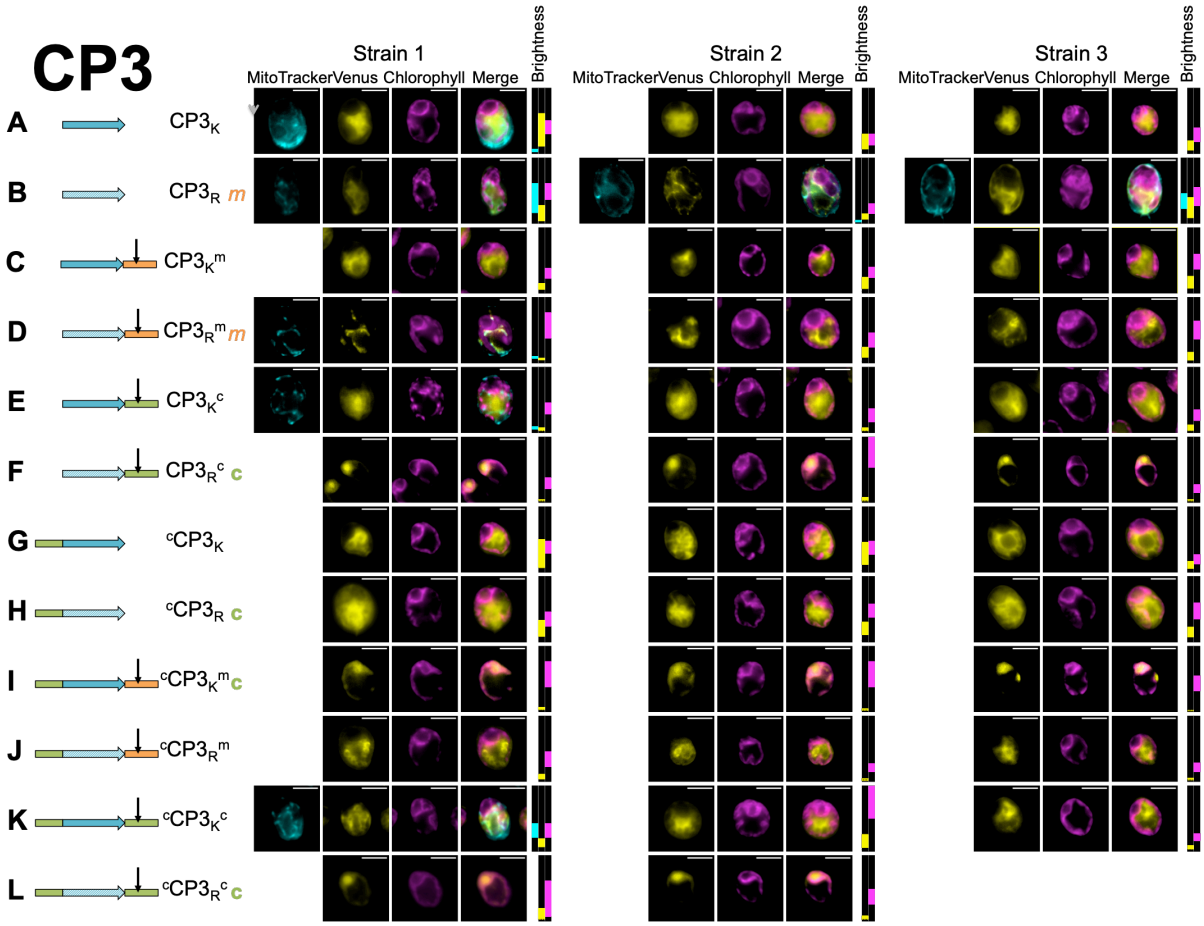

bioRxiv preprint doi: https://doi.org/10.1101/2021.12.03.471120; this version posted June 23, 2022. The copyright holder for this preprint (which was not certified by peer review) is the author/funder, who has granted bioRxiv a license to display the preprint in perpetuity. It is made available under aCC-BY-NC-ND 4.0 International license.

Fig. S9. Microscopy for biological replicates of Sarcotoxin 1D. Three independent transformant lines (Strains 1-3) are shown for each combination of modifications (A-L), represented by a cartoon and a shorthand description (cf. Fig. 2). Where a construct was interpreted as generating reporter localization in mitochondria or chloroplast, this is indicated by an orange 'm' or a green 'c' respectively, in bold for full targeting or in italics for partial targeting. Scale bars are 5µm.

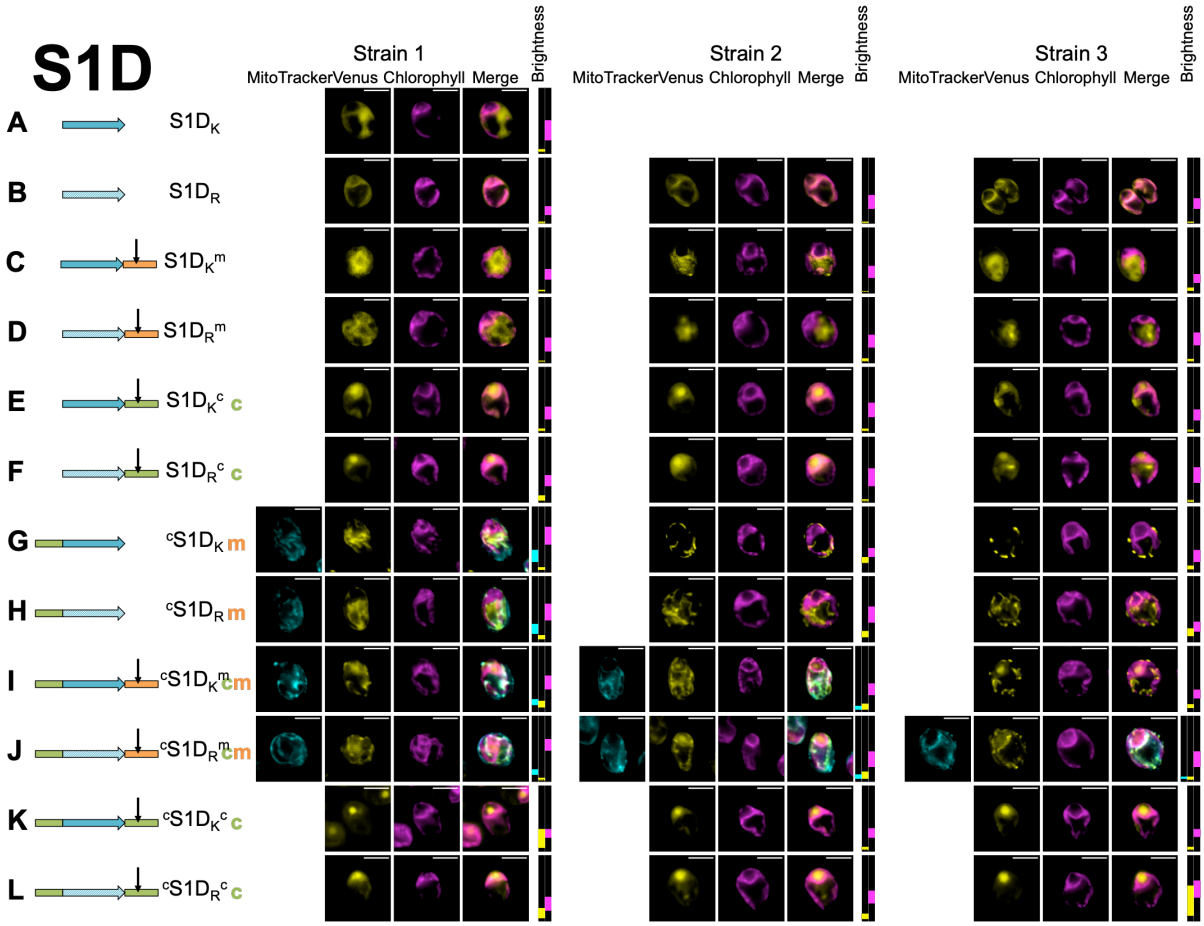

bioRxiv preprint doi: https://doi.org/10.1101/2021.12.03.471120; this version posted June 23, 2022. The copyright holder for this preprint (which was not certified by peer review) is the author/funder, who has granted bioRxiv a license to display the preprint in perpetuity. It is made available under aCC-BY-NC-ND 4.0 International license.

Fig. S10. Microscopy for biological replicates of Esculentin 1S. Three independent transformant lines (Strains 1-3) are shown for each combination of modifications (A-L), represented by a cartoon and a shorthand description (cf. Fig. 2). Where a construct was interpreted as generating reporter localization in mitochondria or chloroplast, this is indicated by an orange 'm' or a green 'c' respectively, in bold for full targeting or in italics for partial targeting. Scale bars are 5µm.

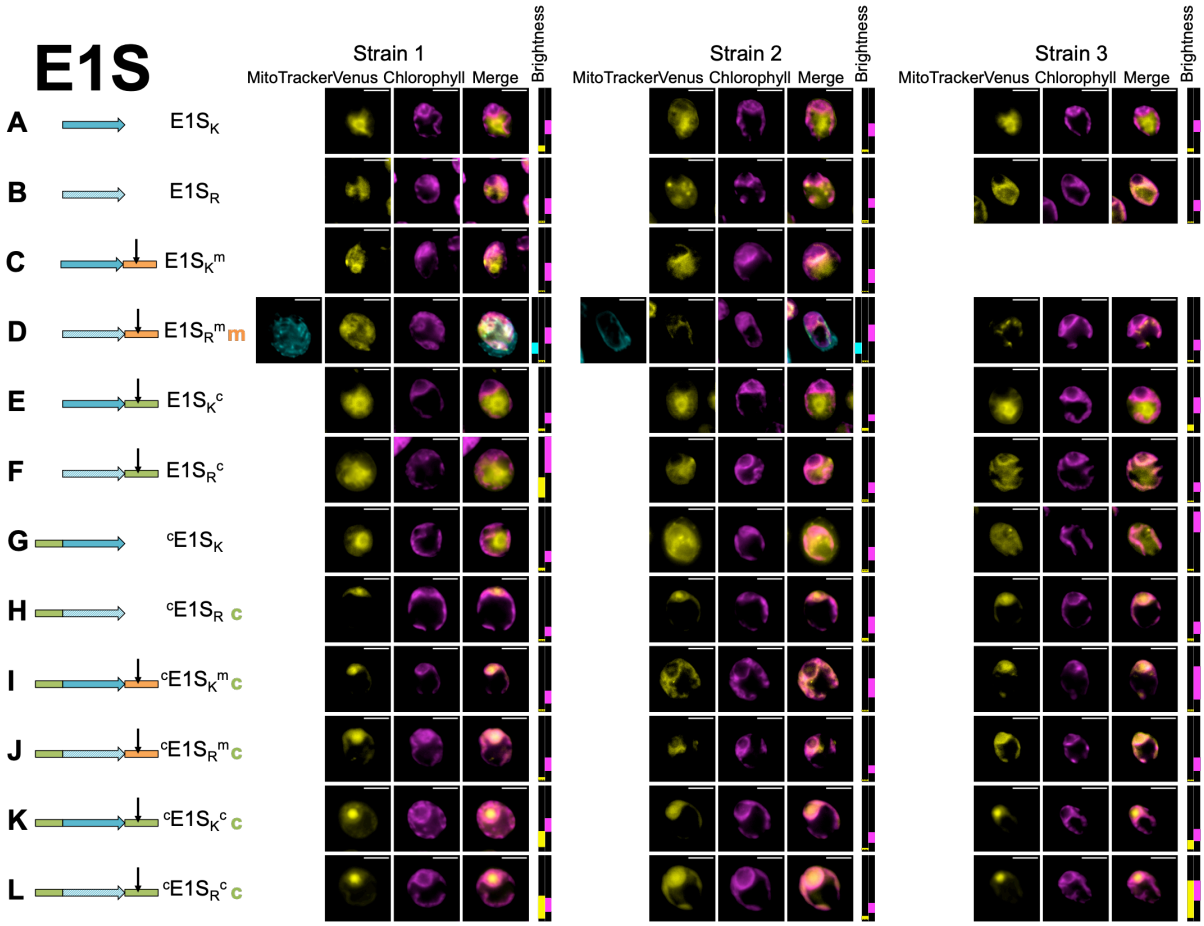

bioRxiv preprint doi: https://doi.org/10.1101/2021.12.03.471120; this version posted June 23, 2022. The copyright holder for this preprint (which was not certified by peer review) is the author/funder, who has granted bioRxiv a license to display the preprint in perpetuity. It is made available under aCC-BY-NC-ND 4.0 International license.

Fig. S11. Microscopy for biological replicates of Leucocin A. Three independent transformant lines (Strains 1-3) are shown for each combination of modifications (A-L), represented by a cartoon and a shorthand description (cf. Fig. 2). Where a construct was interpreted as generating reporter localization in mitochondria or chloroplast, this is indicated by an orange 'm' or a green 'c' respectively, in bold for full targeting or in italics for partial targeting. Scale bars are 5µm.

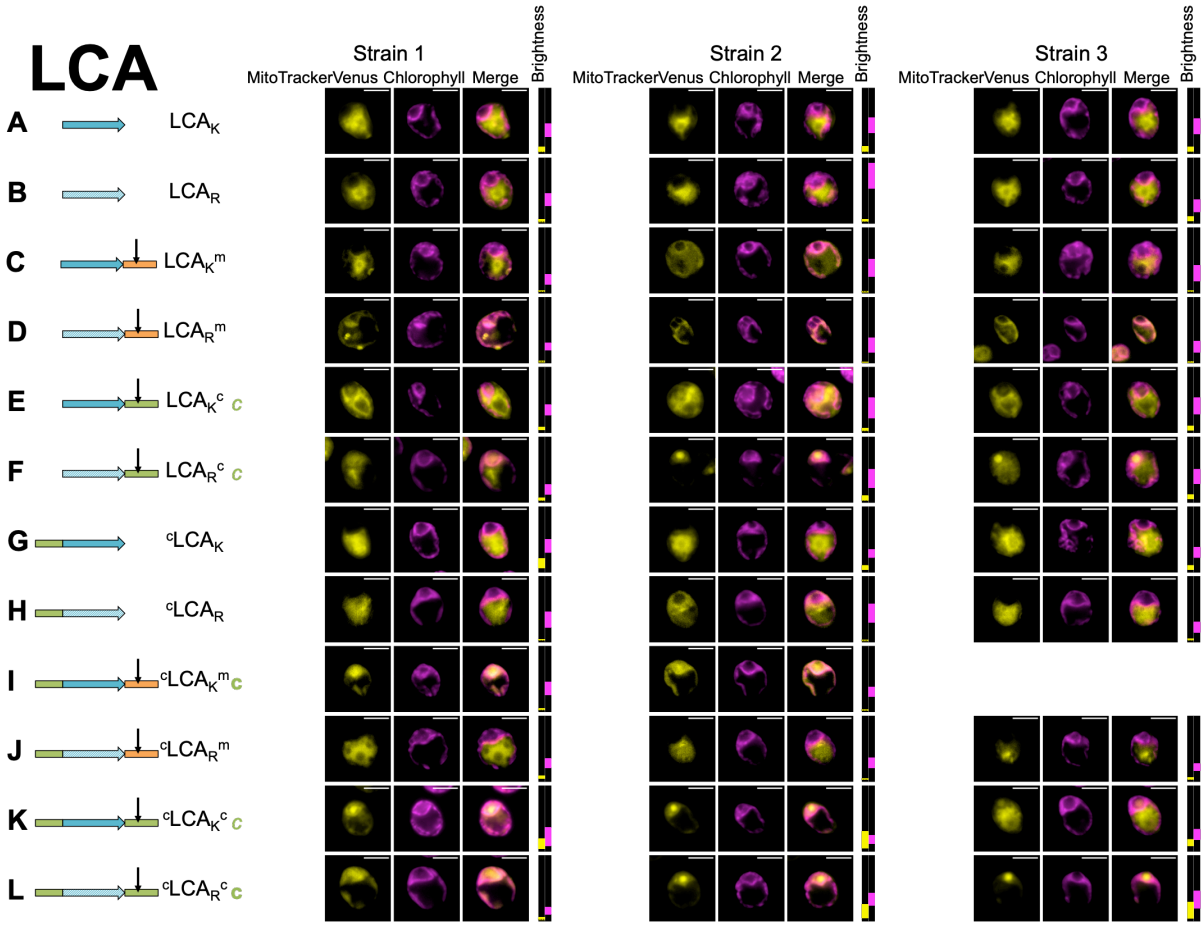

bioRxiv preprint doi: https://doi.org/10.1101/2021.12.03.471120; this version posted June 23, 2022. The copyright holder for this preprint (which was not certified by peer review) is the author/funder, who has granted bioRxiv a license to display the preprint in perpetuity. It is made available under aCC-BY-NC-ND 4.0 International license.

Fig. S12. Microscopy for biological replicates of SI Moricin. Three independent transformant lines (Strains 1-3) are shown for each combination of modifications (A-L), represented by a cartoon and a shorthand description (cf. Fig. 2). Where a construct was interpreted as generating reporter localization in mitochondria or chloroplast, this is indicated by an orange 'm' or a green 'c' respectively, in bold for full targeting or in italics for partial targeting. Scale bars are 5µm.

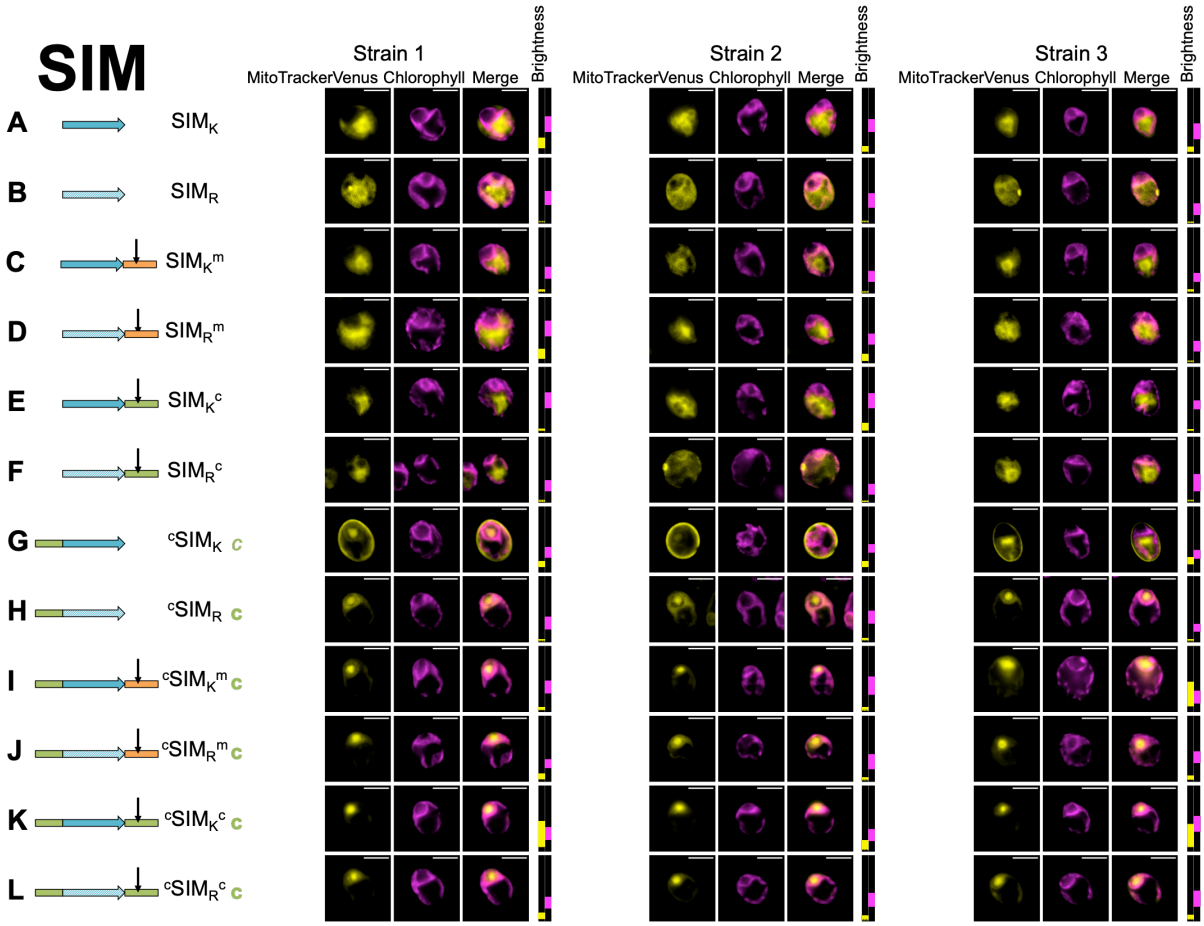

bioRxiv preprint doi: https://doi.org/10.1101/2021.12.03.471120; this version posted June 23, 2022. The copyright holder for this preprint (which was not certified by peer review) is the author/funder, who has granted bioRxiv a license to display the preprint in perpetuity. It is made available under aCC-BY-NC-ND 4.0 International license.

Fig. S13. Microscopy for biological replicates of Bacillocin 1580. Three independent transformant lines (Strains 1-3) are shown for each combination of modifications (A-L), represented by a cartoon and a shorthand description (cf. Fig. 2). Where a construct was interpreted as generating reporter localization in mitochondria or chloroplast, this is indicated by an orange 'm' or a green 'c' respectively, in bold for full targeting or in italics for partial targeting. Scale bars are 5µm.

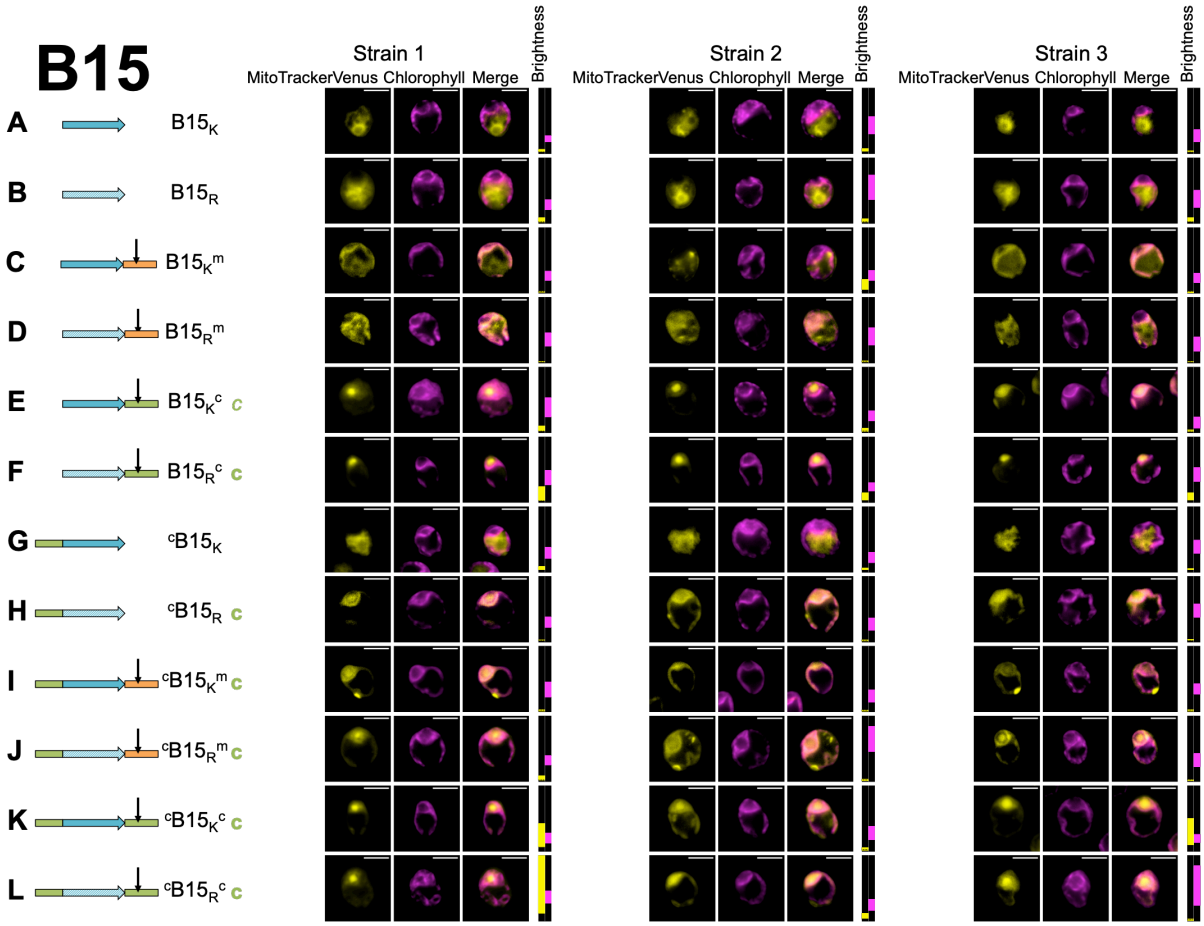

bioRxiv preprint doi: https://doi.org/10.1101/2021.12.03.471120; this version posted June 23, 2022. The copyright holder for this preprint (which was not certified by peer review) is the author/funder, who has granted bioRxiv a license to display the preprint in perpetuity. It is made available under aCC-BY-NC-ND 4.0 International license.

Fig. S14. Microscopy for biological replicates of Enterocin HF. Three independent transformant lines (Strains 1-3) are shown for each combination of modifications (A-L), represented by a cartoon and a shorthand description (cf. Fig. 2). Where a construct was interpreted as generating reporter localization in mitochondria or chloroplast, this is indicated by an orange 'm' or a green 'c' respectively, in bold for full targeting or in italics for partial targeting. Scale bars are 5µm.

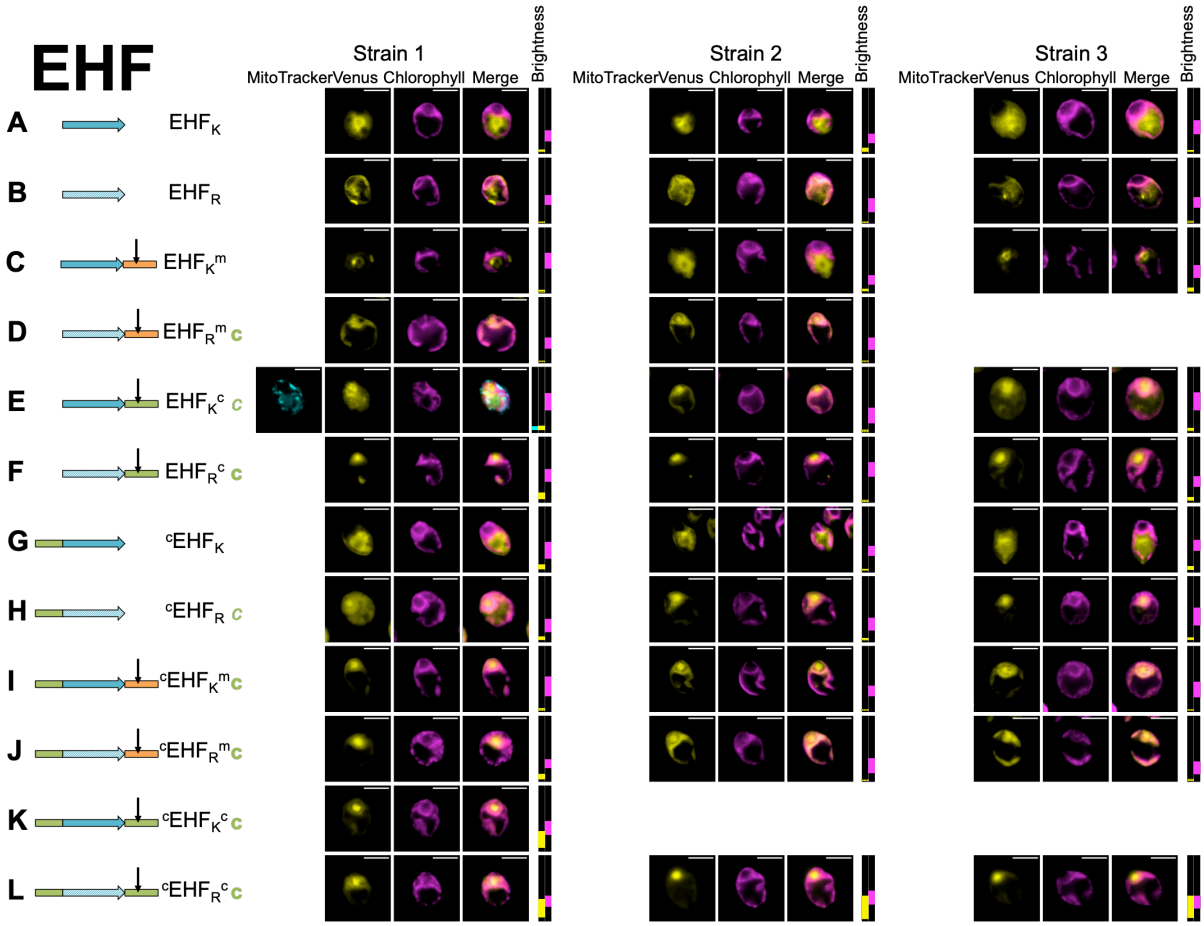

bioRxiv preprint doi: https://doi.org/10.1101/2021.12.03.471120; this version posted June 23, 2022. The copyright holder for this preprint (which was not certified by peer review) is the author/funder, who has granted bioRxiv a license to display the preprint in perpetuity. It is made available under aCC-BY-NC-ND 4.0 International license.

Fig. S15. Microscopy for biological replicates of negative control Random Peptide 1. Three independent transformant lines (Strains 1-3) are shown for each combination of modifications (A-F), represented by a cartoon and a shorthand description (cf. Fig. 2). Where a construct was interpreted as generating reporter localization in mitochondria or chloroplast, this is indicated by an orange 'm' or a green 'c' respectively, in bold for full targeting or in italics for partial targeting. Scale bars are 5µm.

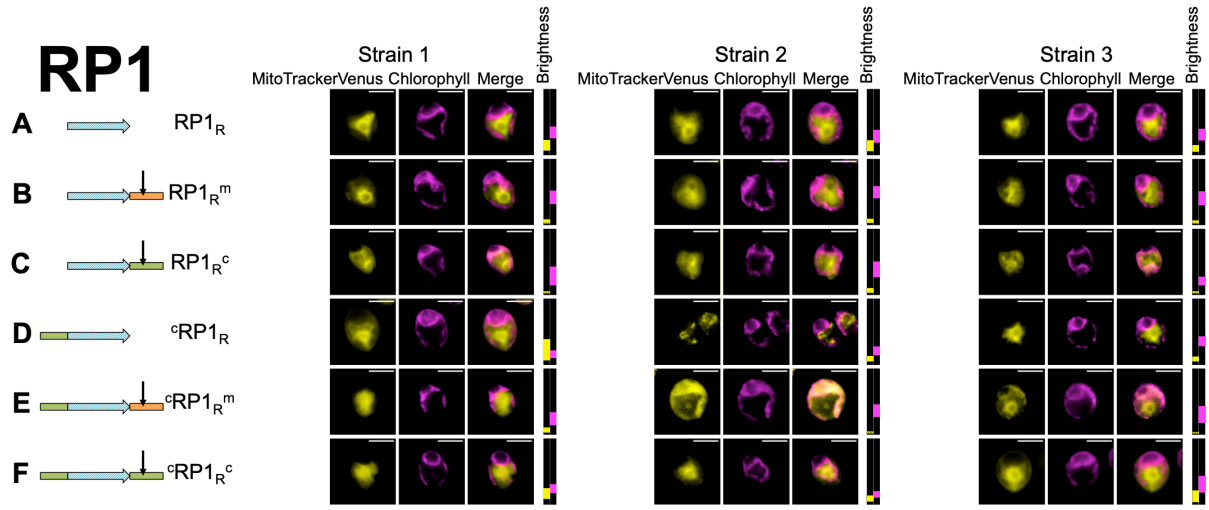

bioRxiv preprint doi: https://doi.org/10.1101/2021.12.03.471120; this version posted June 23, 2022. The copyright holder for this preprint (which was not certified by peer review) is the author/funder, who has granted bioRxiv a license to display the preprint in perpetuity. It is made available under aCC-BY-NC-ND 4.0 International license.

Fig. S16. Microscopy for biological replicates of negative control Random Peptide 2. Three independent transformant lines (Strains 1-3) are shown for each combination of modifications (A-L), represented by a cartoon and a shorthand description (cf. Fig. 2). Where a construct was interpreted as generating reporter localization in mitochondria or chloroplast, this is indicated by an orange 'm' or a green 'c' respectively, in bold for full targeting or in italics for partial targeting. Scale bars are 5µm.

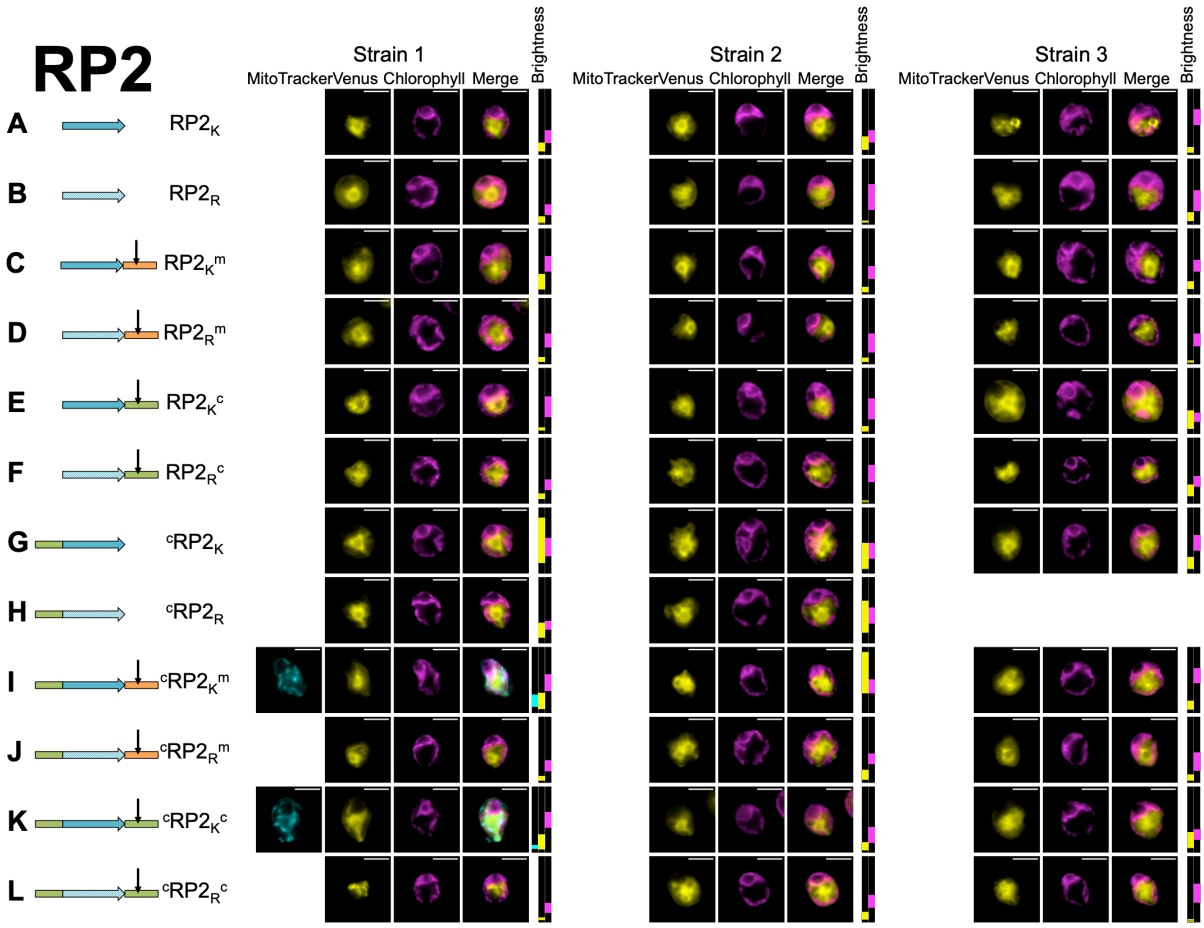

bioRxiv preprint doi: https://doi.org/10.1101/2021.12.03.471120; this version posted June 23, 2022. The copyright holder for this preprint (which was not certified by peer review) is the author/funder, who has granted bioRxiv a license to display the preprint in perpetuity. It is made available under aCC-BY-NC-ND 4.0 International license.

Fig. S17. Microscopy for biological replicates of TP control Rubisco activase cTP helical element (CH). Three independent transformant lines (Strains 1-3) are shown for each combination of modifications (A-L), represented by a cartoon and a shorthand description (cf. Fig. 2). Where a construct was interpreted as generating reporter localization in mitochondria or chloroplast, this is indicated by an orange 'm' or a green 'c' respectively, in bold for full targeting or in italics for partial targeting. Scale bars are 5µm.

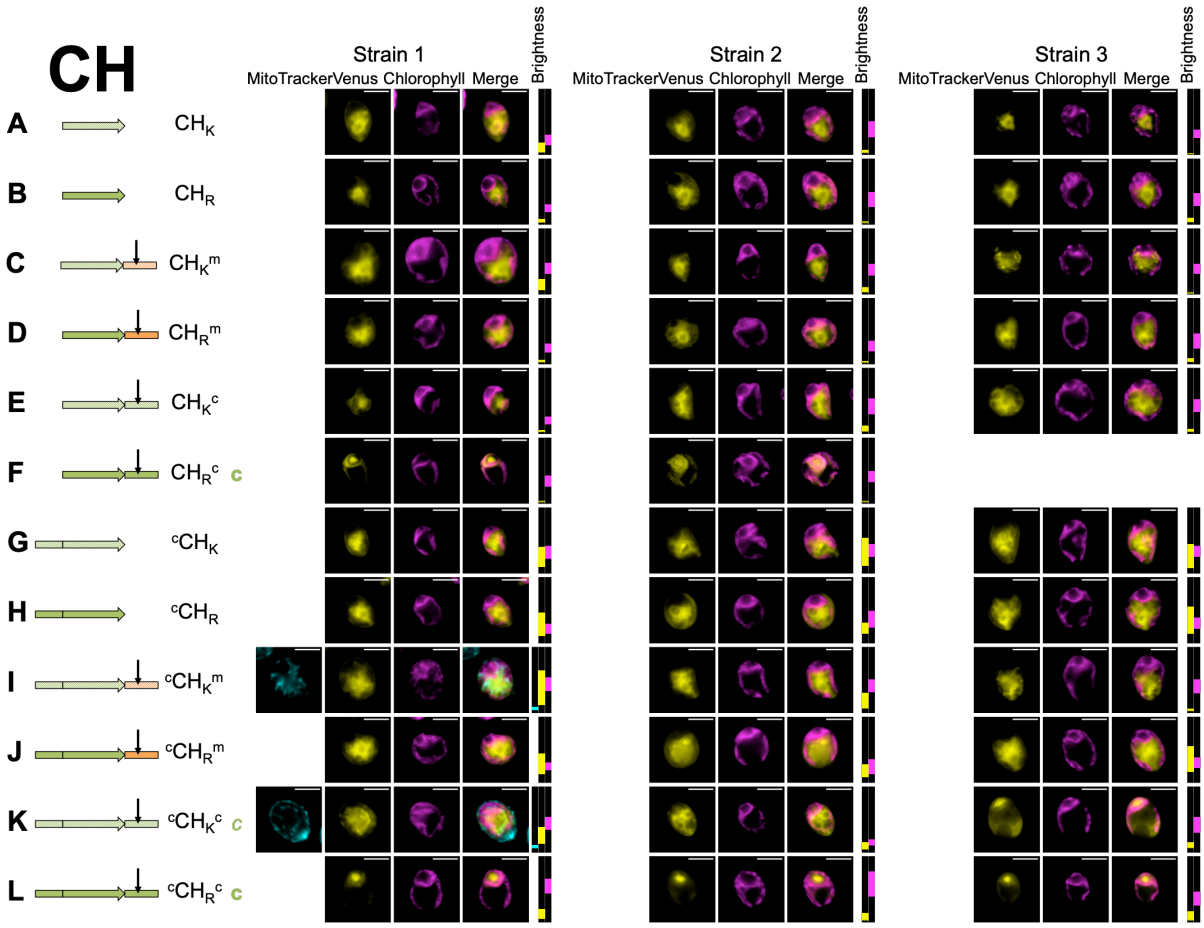

bioRxiv preprint doi: https://doi.org/10.1101/2021.12.03.471120; this version posted June 23, 2022. The copyright holder for this preprint (which was not certified by peer review) is the author/funder, who has granted bioRxiv a license to display the preprint in perpetuity. It is made available under aCC-BY-NC-ND 4.0 International license.

Fig. S18. Microscopy for biological replicates of TP control mitochondrial γ-carbonic anhydrase 2 mTP helical element (MH). Three independent transformant lines (Strains 1-3) are shown for each combination of modifications (A-L), represented by a cartoon and a shorthand description (cf. Fig. 2). Where a construct was interpreted as generating reporter localization in mitochondria or chloroplast, this is indicated by an orange 'm' or a green 'c' respectively in bold for full targeting or in italics for partial targeting. Scale bars are 5µm.

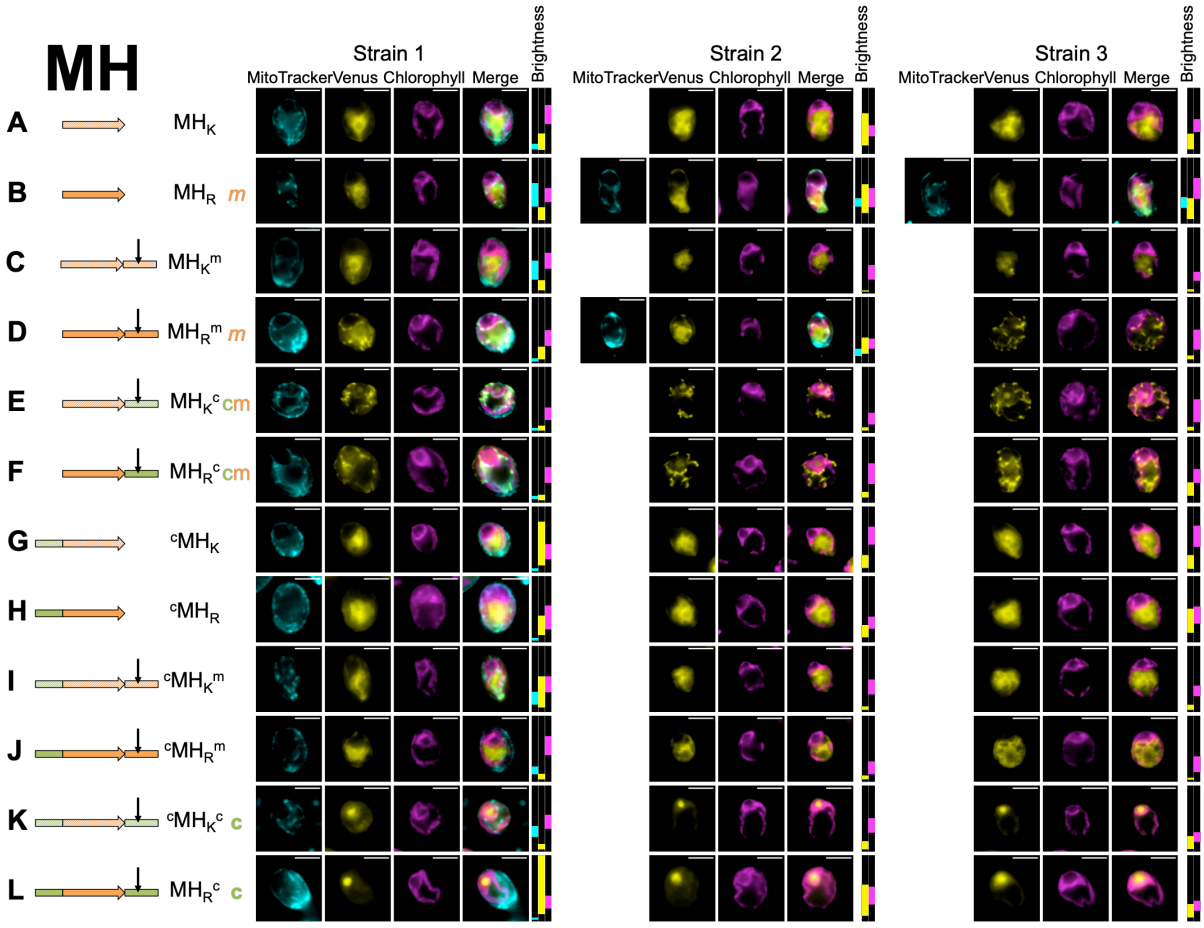

bioRxiv preprint doi: https://doi.org/10.1101/2021.12.03.471120; this version posted June 23, 2022. The copyright holder for this preprint (which was not certified by peer review) is the author/funder, who has granted bioRxiv a license to display the preprint in perpetuity. It is made available under aCC-BY-NC-ND 4.0 International license.

Fig. S19. Microscopy for biological replicates of no-peptide and Alanine-screen controls. Three independent transformant lines (Strains 1-3) are shown for each combination of elements (A-G), represented by a cartoon and a shorthand description (cf. Fig. 2). Where a construct was interpreted as generating reporter localization in mitochondria or chloroplast, this is indicated by an orange 'm' or a green 'c' respectively, in bold for full targeting or in italics for partial targeting. Scale bars are 5µm.

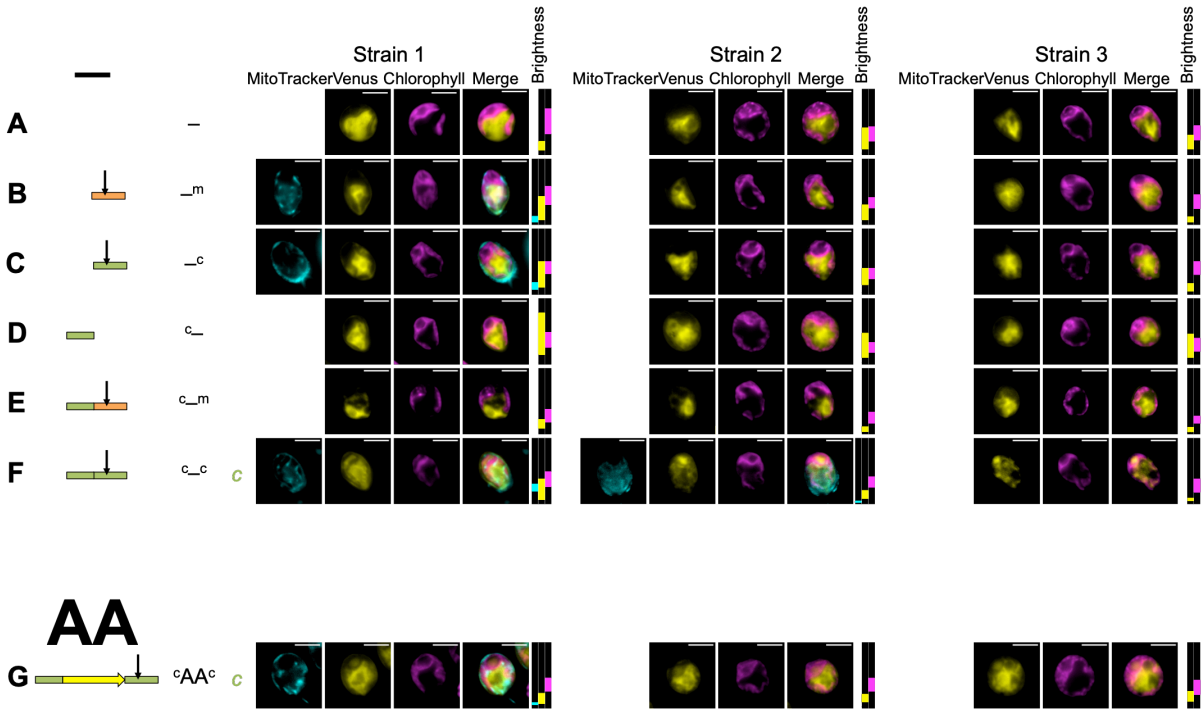

bioRxiv preprint doi: https://doi.org/10.1101/2021.12.03.471120; this version posted June 23, 2022. The copyright holder for this preprint (which was not certified by peer review) is the author/funder, who has granted bioRxiv a license to display the preprint in perpetuity. It is made available under aCC-BY-NC-ND 4.0 International license.

Fig. S20. Comparison of amino acid frequencies reveals K/R shift. (**a**) Amino acid frequencies are shown as boxplots (center line: median; box limits: upper and lower quartiles; whiskers: min/max values within 1.5x interquartile range) for Chlamydomonas cTPs in green, Chlamydomonas mTPs in orange and HA-RAMPs in blue. To give a baseline for comparison, the average across UNIPROT is given for each amino acid as red horizontal line. For each residue, different letters underneath distributions indicate a significant difference: groups that share the same letter are significantly different at $p<0.05$ (Multiple Kruskal Wallis tests followed by Dunn post-hoc tests) from groups attributed a different letter. (**b**) Amino acid frequencies are shown as heatmap for human, plant, algal and yeast TPs.

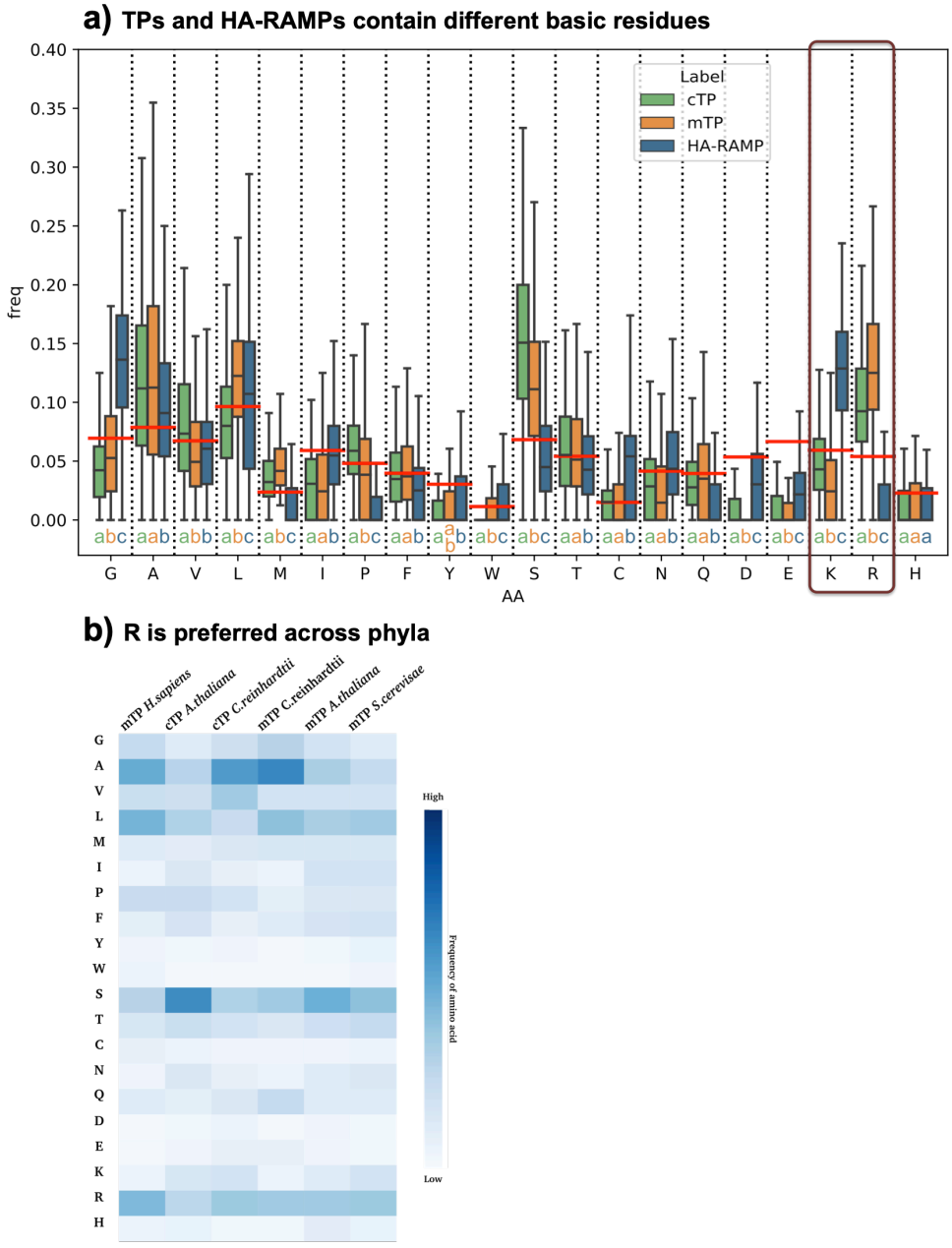

bioRxiv preprint doi: https://doi.org/10.1101/2021.12.03.471120; this version posted June 23, 2022. The copyright holder for this preprint (which was not certified by peer review) is the author/funder, who has granted bioRxiv a license to display the preprint in perpetuity. It is made available under aCC-BY-NC-ND 4.0 International license.

Fig. S21. Principal component analyses reveal that N- but not C-termini differ between cTPs and mTPs. Principal component (PC) analyses of auto-cross-correlated Z-scale values[10] for (**a**) N-termini (15 residues) and (**b**) C-termini (33 residues, encompassing -10 to +23 relative to the cleavage site for TPs) respectively of Chlamydomonas cTPs (in green) and mTPs (in orange) as well as the 13 HA-RAMPs under study (in blue; crosses denote HA-RAMPs after K→R).

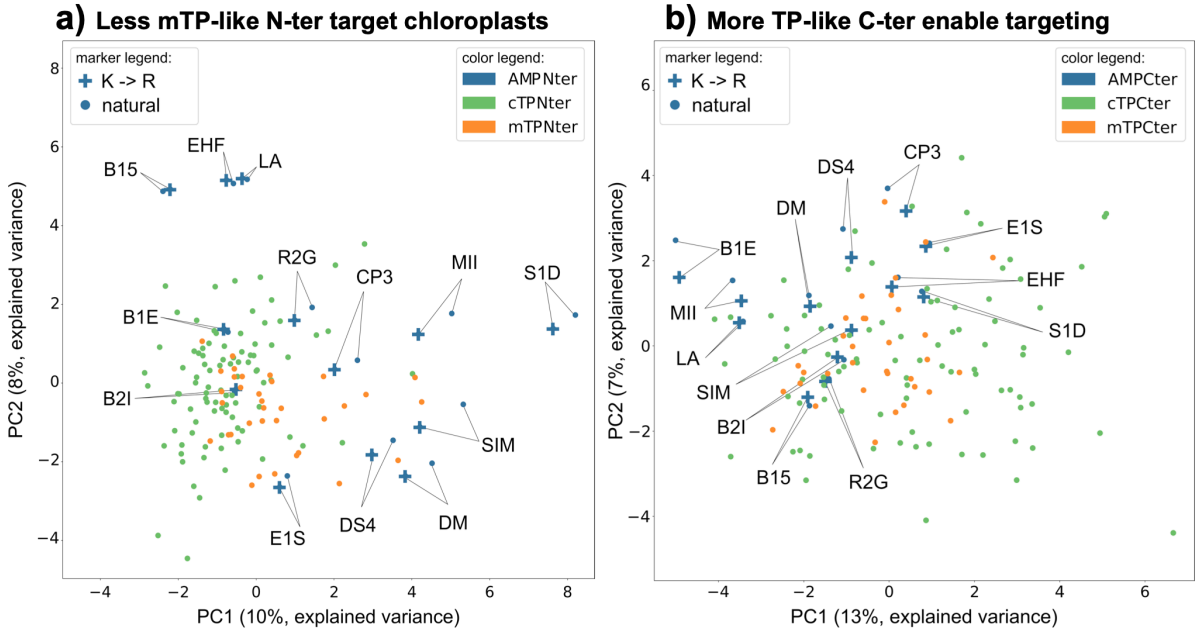

bioRxiv preprint doi: https://doi.org/10.1101/2021.12.03.471120; this version posted June 23, 2022. The copyright holder for this preprint (which was not certified by peer review) is the author/funder, who has granted bioRxiv a license to display the preprint in perpetuity. It is made available under aCC-BY-NC-ND 4.0 International license.

Fig. S22. Unusual algal cTP N-termini share physicochemical differences against mTP N-termini with plant counterparts. (**a**) Plots detailing the percentage of uncharged residues (i.e. excluding K/R and D/E, as in[27]) for window sizes ranging from 5 to 17 residues (refer to legend for colour code) show that Chlamydomonas cTPs (on the left) are less uncharged at the N-terminus than Arabidopsis cTPs (on the right)**.** Dashed grey lines indicate the average value for randomized sequences (including mature proteins), to provide an estimate of what would be expected by chance. (**b**) Equivalent graphs (as in A) for mTPs show a similar charge profile across Chlamydomonas and Arabidopsis. (**c-e**) Distributions of salient values as boxplots (center line: median; box limits: upper and lower quartiles; whiskers: min/max values within 1.5x interquartile range) for mTPs in orange and cTPs in green with *Chlamydomonas reinhardtii* (Cr) on the left and *Arabidopsis thaliana* (At) on the right show that: (**c**) Chlamydomonas cTP N-termini contain R at almost the same frequency as mTP N-termini, whereas Arabidopsis cTP N-termini contain fewer R; (**d**) Chlamydomonas TP N-termini are less hydrophobic than Arabidopsis TP N-termini, with plant cTP N-termini showing the highest hydrophobicity; (**e**) Chlamydomonas cTP N-termini are more disordered than mTP or Arabidopsis cTP N-termini. Points represent individual peptides (note that for integer values, point positions are randomized within ±0.5 in y as well as in x to increase point separation), population means are shown as black diamonds. (**f**) Binomial logistic regression classifier separating TPs using auto-cross-covariance of Z-scales[10] of the N-terminal 15 residues for *C. reinhardtii*. The left-hand graph shows the distribution of cTPs in green and mTPs in orange over the model output 'mTP score'. Black bars at the bottom of the graph represent scores for cTPs of Arabidopsis, showing that plant cTPs are recognized as cTPs by the model trained on algal cTP N-termini (89% recognized as cTPs, with an mTP score <0.5). Values for our 13 HA-RAMPs are given below the graph. The right-hand graph shows receiver operating characteristic (ROC) curves, plotting the true positive rate (TPR) against the false positive rate (FPR), where the area under the curve (AUC) serves as estimate of the model quality with values above 0.5 indicating that the model is better than random. (**g**) Equivalent model (as in F) trained on *A. thaliana* TPs, with black bars now representing Chlamydomonas cTPs showing that the majority of algal cTPs are recognized as cTPs by the plant model (75% recognized as cTPs, with an mTP score <0.5).

bioRxiv preprint doi: https://doi.org/10.1101/2021.12.03.471120; this version posted June 23, 2022. The copyright holder for this preprint (which was not certified by peer review) is the author/funder, who has granted bioRxiv a license to display the preprint in perpetuity. It is made available under aCC-BY-NC-ND 4.0 International license.

1218

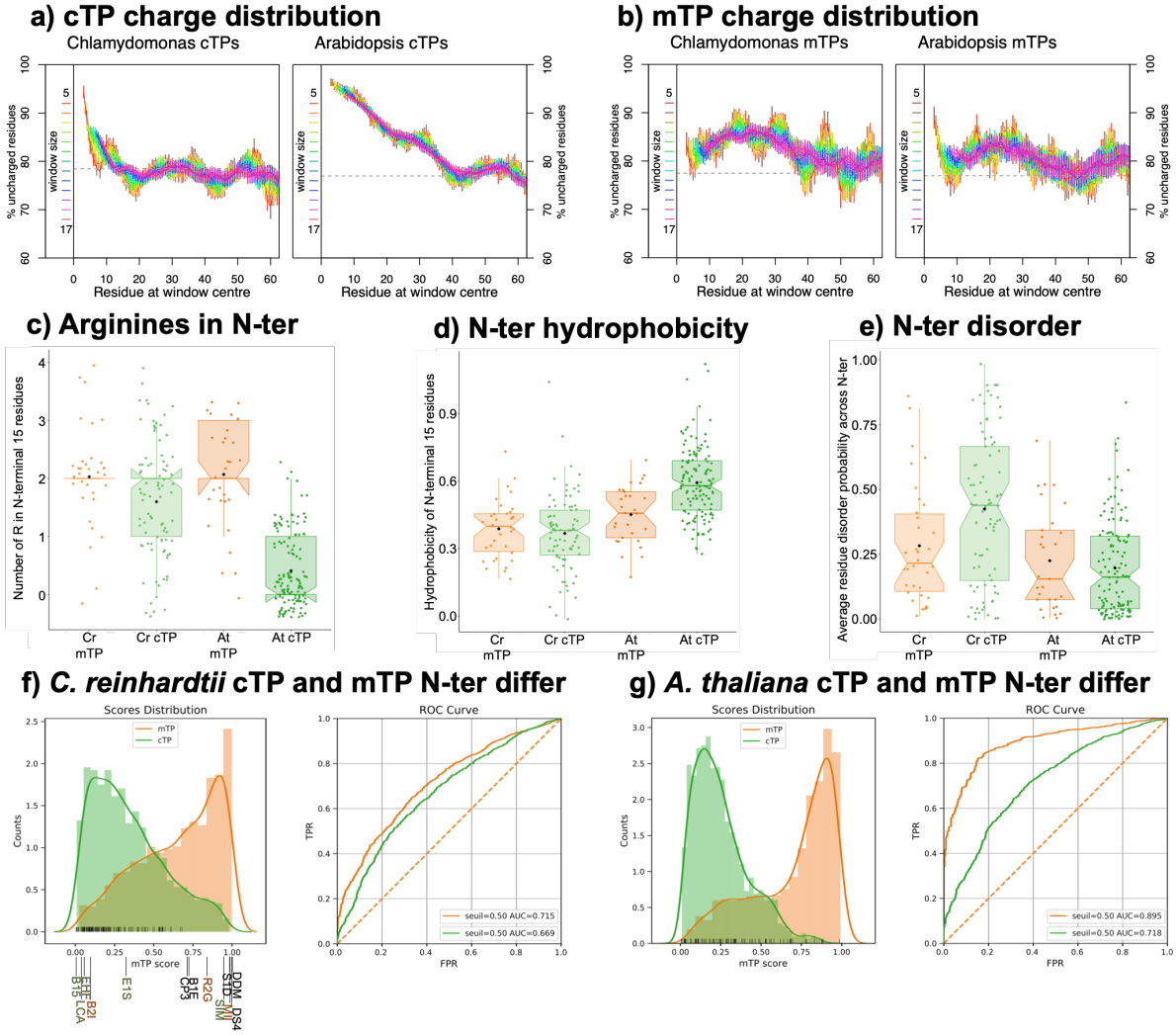

1219

1220

bioRxiv preprint doi: https://doi.org/10.1101/2021.12.03.471120; this version posted June 23, 2022. The copyright holder for this preprint (which was not certified by peer review) is the author/funder, who has granted bioRxiv a license to display the preprint in perpetuity. It is made available under aCC-BY-NC-ND 4.0 International license.

Fig. S23. K→R generally improves HA-RAMP targeting. (**a**) An overview graph showing how many, out of 13 HA-RAMPs studied, show targeting to either mitochondria (mt) or chloroplast (cp), or both (dual) before and after K→R represented. (**b-e**) Epifluorescence microscopy images of selected examples are shown as in Fig. 3.

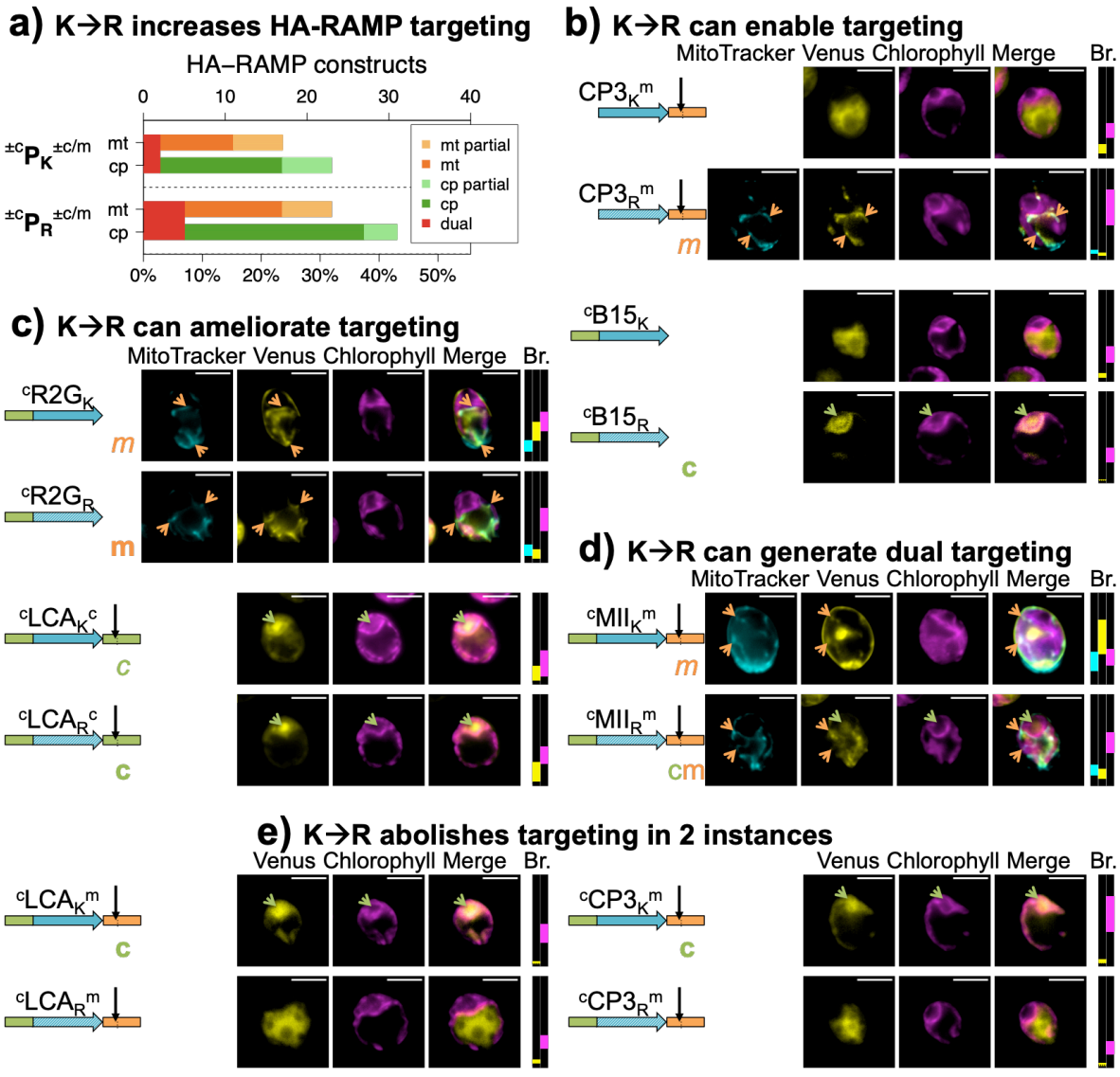

bioRxiv preprint doi: https://doi.org/10.1101/2021.12.03.471120; this version posted June 23, 2022. The copyright holder for this preprint (which was not certified by peer review) is the author/funder, who has granted bioRxiv a license to display the preprint in perpetuity. It is made available under aCC-BY-NC-ND 4.0 International license.

Fig. S24. HA-RAMP properties determine their targeting propensities. PCA analysis of cTPs (green dots), mTPs (orange dots), cp-set HA-RAMPs (green crosses), mt-set HA-RAMPs (orange crosses) and other HA-RAMPs (dark crosses) based on their length (Peptide Length: PL), number of residues before the longest predicted amphipathic helix (Long Helix Start: LHS), fraction of residues forming the predicted amphipathic helix (Helix Fraction: HF) and fraction of K (Fraction of Lysines: FK) and R residues (Fraction of Arginine: FR). Arrows on the graph represent the eigenvalues of the individual variables. The first principal component explains 43% of the variance and distinguishes peptides principally according to FK, PL, LHS (pointing left) and FR residues (pointing right). The second principal component explains 24% of the variance and distinguishes peptides principally according to HF. The cp-set HA-RAMPs group with the most distinguishable cTPs, being longer, with a higher LHS and a lower HF compared to mt-set HA-RAMPs and mTPs.

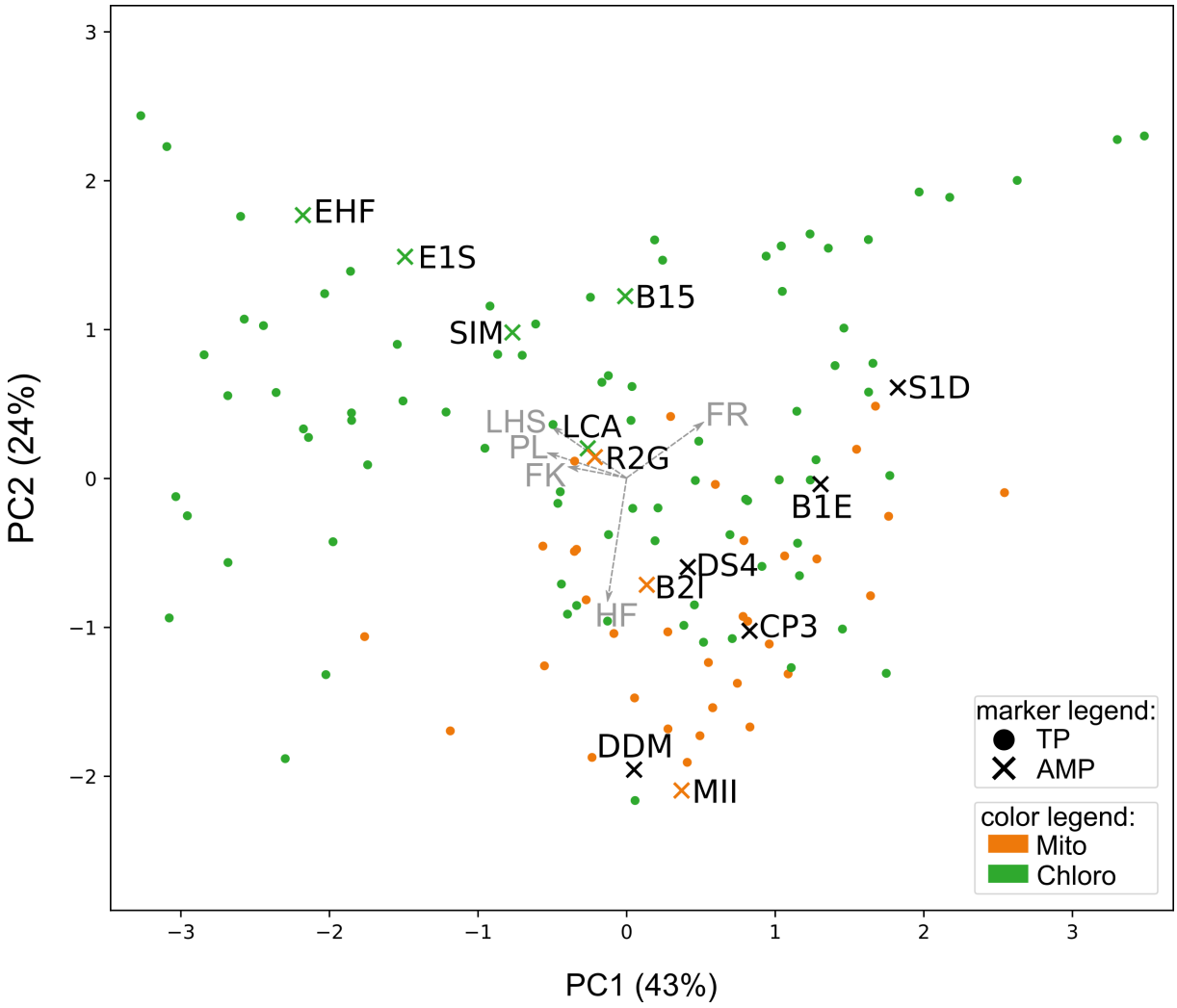

bioRxiv preprint doi: https://doi.org/10.1101/2021.12.03.471120; this version posted June 23, 2022. The copyright holder for this preprint (which was not certified by peer review) is the author/funder, who has granted bioRxiv a license to display the preprint in perpetuity. It is made available under aCC-BY-NC-ND 4.0 International license.

Fig. S25. Higher protein interactivity predicted for cTPs than mTPs. (**a,b,f**) For salient properties, Chlamydomonas mTPs and cTPs are compared to HA-RAMPs (cp-set in green, mt-set in orange). Distributions are shown as boxplots (center line: median; box limits: upper and lower quartiles; whiskers: min/max values within 1.5x interquartile range), coloured points represent individual peptides (**a**) cTPs show increased protein interactivity (p=0.0003), as do cp-set HA-RAMPs (p= 0.0355), as estimated through Boman values[69], a proxy developed for AMPs where a value of ca. >2 indicates increased protein interaction potential, and <2 points to membrane interaction. (**b**) cTPs show increased protein interactivity (p<0.0001), and cp-set HA-RAMPs show a similar tendency (p=0.0638), as estimated with Anchor2[70], developed to predict the protein interaction potential of disordered sequences. (**c**) Both cTPs and mTPs show a high fraction of peptides (~50%) that have an Hsp70 interaction site over a 6-residue window at any given position along the sequence in the top graph, with a peak towards the N-terminus. HA-RAMP constructs shown in the bottom graph also display a peak in predicted Hsp70-binding sites at the N-terminus, independently of construct localisation. The value obtained after randomizing the position of residues is given as dashed grey line to provide an estimate of how often sites would be expected to occur given amino acid frequencies (~50%). Randomization was done over the entire sequence including the cargo protein. (**d**) For Arabidopsis cTPs in the top graph, the percentage of peptides that have a full 'FGLK' site[27] (black curve; presence of F and G/P and L/V/A and K/R and absence of D/E within an 8-residue window) far exceeds the value obtained after randomizing the position of residues (dashed black line for full 'FGLK' sites), a proxy for the frequency of the motif expected at random, for most positions along the sequence up to ~60 residues. Randomization was done over the entire sequence including the cargo protein. Reduced 'FGLK'-1 sites containing three out of four elements appear to occur mostly in the context of full FGLK sites, except for 'GLK' sites for which randomization is also shown (dashed red line). Arabidopsis mTPs (bottom graph) also contain 'FLGK' sites at a frequency higher than expected at random between residues 20-40, and 'GLK' sites upstream of residue 40, but motifs are less prevalent than in cTPs. (**e**) Equivalent graphs (as D) for Chlamydomonas show that full 'FGLK' sites (black lines) are rare in cTPs (top graph) and actually more common in mTPs (bottom graph) upstream of residue 40. Reduced 'GLK' sites (red lines) by contrast far exceed

bioRxiv preprint doi: https://doi.org/10.1101/2021.12.03.471120; this version posted June 23, 2022. The copyright holder for this preprint (which was not certified by peer review) is the author/funder, who has granted bioRxiv a license to display the preprint in perpetuity. It is made available under aCC-BY-NC-ND 4.0 International license.

the prevalence expected at random (dashed red line) ca. up to residue 40. (**f**) Protein interactivity, estimated through Boman values, for only those parts of peptides that correspond to FGLK-1 sites is increased for cTPs ($p<0.0001$), and cp-set HA-RAMPs show a similar tendency ($p= 0.0627$). Note that cTP-C and cTP-N, but not mTP-C, contain 'FGLK-1' sites with predicted protein interactivity. *DS4 contains no 'FGLK-1' sites. Reported p-values were obtained through two-way t-tests for TPs and one-way t-tests for HA-RAMPs.

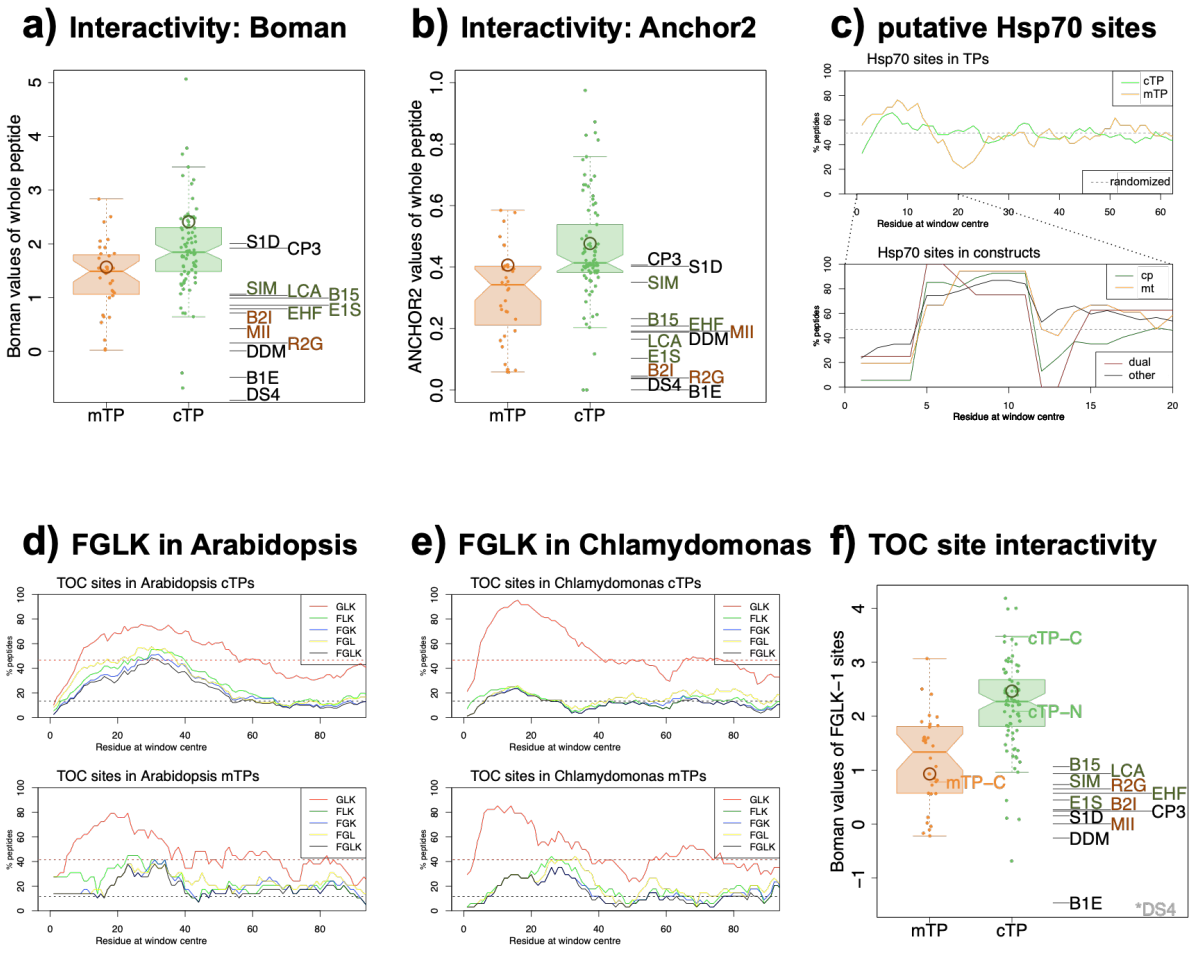

bioRxiv preprint doi: https://doi.org/10.1101/2021.12.03.471120; this version posted June 23, 2022. The copyright holder for this preprint (which was not certified by peer review) is the author/funder, who has granted bioRxiv a license to display the preprint in perpetuity. It is made available under aCC-BY-NC-ND 4.0 International license.

Fig. S26. Hsp70 and (F)GLK sites are present in HA-RAMPs. Predicted Hsp70 binding sites are underlined in blue. Putative TOC interaction sites are overlined in green: 'FGLK' sites in dark green and 'GLK' sites in light green. See Fig. 1 for detailed annotations. Notably, both TOC and Hsp70-interaction sites are contained within native HA-RAMPs (**a**) and within our TP controls (**b**).

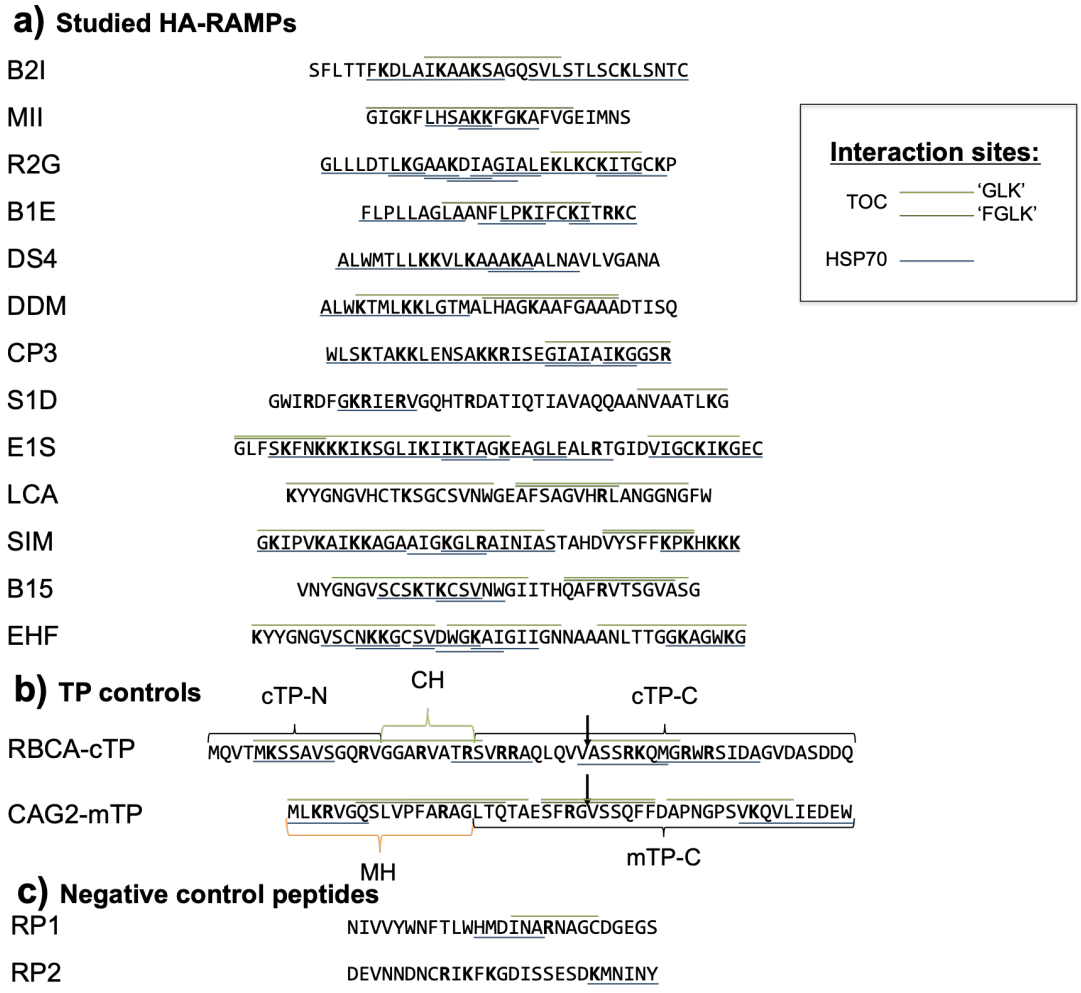

bioRxiv preprint doi: https://doi.org/10.1101/2021.12.03.471120; this version posted June 23, 2022. The copyright holder for this preprint (which was not certified by peer review) is the author/funder, who has granted bioRxiv a license to display the preprint in perpetuity. It is made available under aCC-BY-NC-ND 4.0 International license.

Fig. S27. Western Blots for K-bearing constructs. Samples were immunolabelled using an α-FLAG primary antibody. Constructs representing different combinations of TP-element additions are shown in rows A-F, as indicated by a shorthand description and a cartoon (cf. Fig. 2). HA-RAMPs are consistently arranged in lanes a-m. Note that the order of HA-RAMPs differs from the one in Fig. 2. Control constructs in lanes o-r carry the R→K modification. Additional technical controls are present in lanes labeled with greek letters. Sections containing HA-RAMPs, control constructs and technical controls are separated by dotted black lines. Technical controls (cf. Fig. 1): – is no peptide, $^{c}CH_R{}^{c}$ is Rubisco activase cTP, $MH_R{}^{m}$ is mitochondrial γ-carbonic anhydrase 2 mTP, ^{c}– is Rubisco activase cTP N-terminal element (15 residues), –^{c} is Rubisco activase cTP C-terminal element (33 residues, -10 to +23 relative to cleavage site), e.v. is empty vector (no Venus expression). Constructs that generated chloroplast and/or mitochondrial localization are marked with a green 'c' and/or an orange 'm' respectively, in bold for full or in italics for partial targeting. Note that row E contains two separate blots for the left-hand section up to lane i and the right-hand section following lane j.